ANALYTICAL AND EXPERIMENTAL STUDY OF

RADIATION-RECRYSTALLIZED NEAR-SURFACE FACETS IN SNOW

by

Blake Walden Morstad

A thesis submitted in partial fulfillment
of the requirements for the degree

of

Master of Science

in

Mechanical Engineering

MONTANA STATE UNIVERSITY
Bozeman, Montana

August 2004

©COPYRIGHT

by

Blake Walden Morstad

2004

All Rights Reserved

APPROVAL

of a thesis submitted by

Blake Walden Morstad

This thesis has been read by each member of the thesis committee and has been found to be satisfactory regarding content, English usage, format, citations, bibliographic style, and consistency, and is ready for submission to the College of Graduate Studies.

Dr. Edward E. Adams

Approved for the Department of Mechanical Engineering

Dr. Vic Cundy

Approved for the College of Graduate Studies

Dr. Bruce R. McLeod

STATEMENT OF PERMISSION TO USE

In presenting this thesis in partial fulfillment of the requirements for a master's degree at Montana State University, I agree that the Library shall make it available to borrowers under rules of the Library.

If I have indicated my intention to copyright this thesis by including a copyright notice page, copying is allowable only for scholarly purposes, consistent with "fair use" as prescribed in the U. S. Copyright Law. Requests for permission for extended quotation from or reproduction of this thesis in whole or in parts may be granted only by the copyright holder.

Blake Walden Morstad

ACKNOWLEDGEMENTS

I would like to thank the Western Transportation Institute, the College of Engineering at Montana State University, and the Federal Highway Administration for providing research assistantship enabling this research. Thanks to Dr. Edward Adams for his advising and guidance and Dr. Ladean McKittrick for his help with numerical and LaTeX related questions. A special thanks to my lovely wife, Adele Morstad, for her support in the last two years of graduate school.

TABLE OF CONTENTS

LIST OF TABLES

LIST OF FIGURES

ABSTRACT

A study on the formation of radiation recrystallized near-surface facets in snow was performed experimentally in an environmental chamber. This recrystallization occurs when surface snow metamorphoses into faceted crystals that result from absorbed solar radiation coupled with cooling effects from longwave and turbulent fluxes. The environmental chamber utilized a metal-halide lamp to mimic solar radiation, which penetrates the snow adding thermal energy at depth. In addition, the ceiling was cooled to simulate a cold sky, thus inducing a net longwave radiation loss at the snow surface. Turbulent flux parameters, including relative humidity and wind velocity were measured. Forty-centimeter thick snow samples with insulated sides were placed in the $-10\,^{\circ}\mathrm{C}$ chamber on a constant temperature plate also at $-10\,^{\circ}\mathrm{C}$. The study focused on the significance of radiation balance and snow density on the recrystallization of snow near the surface. Imposed constant boundary conditions led to formation of facets of varying size at and near the snow surface. Faceting was observed when applied solar flux between $350 - 1100\,W/m^2$ was combined with longwave and turbulent exchange for snow with densities below $300\,kg/m^3$. To better understand the governing processes and to extend the number of scenarios a thermodynamic model was used to extrapolate upon the experimental results. The model incorporated meteorological inputs and calculated a snowpack temperature profile based on relevant snow parameters. Conclusions from both experimental and model analysis show radiation and snow density to be significant factors in radiation recrystallized near-surface facets.

CHAPTER 1

INTRODUCTION

Snow avalanches are natural hazards consisting of snow masses cascading down relatively steep slopes. They are capable of inflicting great loss both in economic terms and fatalities. The human toll from avalanches is evident from an average of 41 fatalities per year from 1995-2000 in North America [Tremper, 2001]. As the number of people recreating and building in the mountain environment increases, the chance for increasing fatalities is likely. Financial costs due to property damage, hazard mitigation, and loss of productivity are large. Total direct economic financial loss was estimated at C$40 million per year in Canada [Jamieson, 2000]. These losses provide the motivation to gain an intimate understanding of avalanches.

There are two general types of snow avalanches: *loose snow* and *slab* [McClung and Schaerer, 1993]. Both of these may occur in wet (melting snowpack) or dry snow. A slope angle large enough to allow for snow to overcome sliding friction is required for both types. Loose snow avalanches start at or near the snow surface within a cohesionless layer and spread into a triangular pattern as snow below becomes involved.

This thesis deals with the slab avalanche phenomenon, which are usually more dangerous than the loose type because they are often larger and more difficult to predict. They start with an initial failure at depth within the snowpack at an interface

between a cohesive layer overlying a less cohesive layer termed the *weak* layer. Failure is thought to occur when the shear stress imposed on the weak layer is greater than its shear strength or resistance to shear [McClung and Schaerer, 1993]. Once failure occurs at this weak layer, rapid fracture propagation[1] in the cohesive slab[2] ensues creating separated blocks of snow essentially cut out of the surrounding snowpack. The fracturing can affect a relatively large area depending on the terrain and within seconds whole slopes can avalanche. To emphasize, the slab layer *is* the avalanche, while the weak layer is the *cause* of the avalanche. Figure 1 shows an example of a slab avalanche shown after failure. Triggering mechanisms, describing what causes the weak layer to fail, can be natural or human related. Some natural triggers include precipitation events (snow and rain), rapid temperature changes, and falling debris (snow cornice fall and icefall). Human triggers include skiers or snowboarders, snowmobiles, and explosives [Tremper, 2001]. These triggers provide additional stress to the snow and if their influence is sufficient, they can start an avalanche by causing failure at the weak layer. Since failure occurs at these weak layers a comprehensive understanding of the processes that form weak layers is necessary to slab avalanche prediction.

Several types of weak layers comprised of faceted crystals exist, including surface hoar, depth hoar, and faceted layers [McClung and Schaerer, 1993; Tremper, 2001]. This thesis concentrates on a type of facet layer formed close to the snow surface

[1] According to Kirchner et al. [2002], snow is one of the most brittle materials in existence.
[2] Nominally perpendicular to the basal fracture.

Figure 1. *An example of a slab avalanche that occurred in Glacier National Park, Montana. Notice that the slab layer (shown above the skier) emanates into the background of the picture. The weak layer is the surface where the skier is standing (Courtesy of Chris Lundy and Karl Birkeland).*

termed *near-surface facets* by Birkeland [1998b]. When buried by snow the near-surface facet weak layer poses an avalanche danger. Birkeland et al. [1998] investigated 30 backcountry avalanches in southwest Montana from 1990-1996 and found that 59% were caused by near-surface facets compared to 31% for surface hoar and 6% for depth hoar. Jamieson and Johnston [1992] found that 29% of the fatal avalanche accidents in Canada from 1972 to 1992 were caused by failures of faceted layers.

Near-surface facets may be formed as a result of three processes, including radiation-recrystallization, melt-layer recrystallization, and diurnal recrystallization. This thesis focuses on the first process, radiation-recrystallization, which takes place when energy balances at the snow surface promote strong temperature gradients within the near-surface layer. This energy balance includes absorption of solar radiation within the snowpack, longwave radiation energy exchange with the atmosphere (sky), and turbulent energy exchange due to convection and sensible heat exchange with air overlying the snowpack. Solar radiation can heat the snowpack at depth while the longwave and turbulent energies cool only the snow surface. The presence of a relatively warm sub-surface and cool surface sets up a temperature gradient, which in turn creates a vapor pressure gradient that causes the snow to metamorphose into angular, faceted crystals. These snow crystals exhibit little cohesion between grains, have a low shear strength, and often persist in the snowpack for long periods of time making these faceted crystals a significant weak layer.

An attempt was made to simulate natural conditions existing within a snowpack in the laboratory setting by using an environmental chamber. The chamber was configured with a solar lamp and a cooled ceiling simulating solar and longwave radiation exchanges, respectively. Snow samples were placed in the chamber, which was set at a given temperature. Two air circulating fans provided air movement over the snow sample to simulate turbulent energy exchange. A series of thirteen experiments, each

performed for different combinations of chamber settings and snow properties, provided discrete data points to validate an energy balance based thermal model. This model was used to predict temperature profiles within the snowpack based on the energy exchanges discussed. These computed profiles were then compared with actual experimental temperature profiles. The thermal model showed good agreement to experimental values and was then further used to run "hypothetical" experiment calculations, allowing each variable in the problem to be singled out in order to determine its influence on facet formation. In the future, the model's ultimate utility may be to aid avalanche forecasting by showing if and where near-surface facets may be expected to form on a snow slope.

CHAPTER 2

BACKGROUND

This section contains an overview of snow metamorphism, energy exchange at the snow surface, snow albedo, and discussion of processes creating near-surface facets.

Snowpack

Metamorphism

Snow crystals form in atmospheric clouds where ice crystals grow due to interactions with water droplets. The resulting forms are generally faceted and are thermodynamically unstable once they become a part of the snowpack. Snow on the ground is a granular material composed of ice grains and interstitial pore spaces. When added to the snowpack, snow crystals lose some of their faceted features and become rounder in shape. Then depending on the thermal environment the snow crystals change size and shape, influenced by three metamorphic processes/regimes: equilibrium (round forming), kinetic (facet forming), and melt-freeze. The transition between the equilibrium and kinetic processes is established at values of vapor pressure gradients within the snowpack, which are a function of temperature gradients. Since vapor pressure is difficult to measure within a snowpack, the temperature gradient, which is easier to measure, is used as an indicator of vapor pressure. The nominal magnitude considered to be the kinetic/equilibrium threshold is $10\,^{\circ}\mathrm{C}/m$ [Akitaya, 1974; Armstrong, 1985;

Colbeck, 1982; Marbouty, 1980]. For temperature gradients above this threshold the kinetic metamorphism process prevails, while below, equilibrium processes are found in a general sense. The melt-freeze process deals with snow melt and formation of grains forming into clusters and poly-crystals that sometimes form ice crusts upon refreezing. The remaining two processes, dealing with dry snow, can be distinguished by the shapes of the metamorphosed grains. This thesis is focused on near-surface facets created by the kinetic metamorphic process in dry snow.

Equilibrium. In this process snow grains are attaining a thermodynamically stable shape, which is a rounded grain. Dendrites and other features with a high positive radius of curvature (convex) have a relatively large vapor pressure over the feature compared to features with negative (concave) or smaller radius of curvature. This vapor pressure differential causes mass loss from angular features and mass gain at rounded or concave features. Snow grains grow increasingly round features with the most stable feature being a sphere. Atmospheric snow, once in the snowpack, can change into a rounded crystal within a matter of days [Colbeck, 1980]. Figure 2 shows an initial snow crystal and subsequent shapes after undergoing equilibrium metamorphism. As the mean snowpack temperature increases so does the rate of rounding. Another important characteristic of this process is that snow inter-granular bonding is increased, which creates cohesive layers. Bond growth is promoted by the vapor transport from convex to concave surfaces creating sintered ice grains, which are discussed later [Colbeck, 1997].

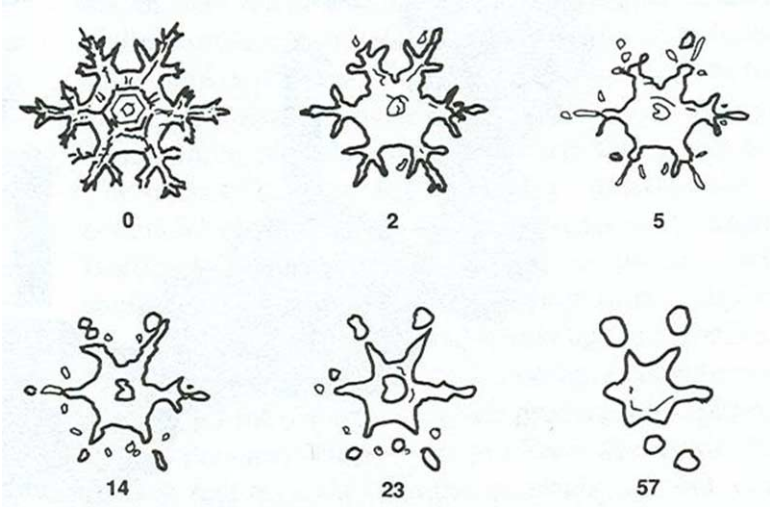

Figure 2. *Equilibrium metamorphism of a snow crystal (numbers indicate days)(Reproduced from McClung and Schaerer [1993]).*

Kinetic. High temperature gradients generally above the threshold of $10\,^{\circ}\mathrm{C}/m$ indicate a process where faceted snow grains form instead of rounded grains. These high temperature gradients induce vapor pressure gradients, which actually are responsible for the kinetic/facet growth. The process can be described as a "hand-to-hand" mechanism where vapor migrates from the warm side of the pore space to the cold side. Since saturated warm air is capable of holding more vapor than saturated cold air, a higher vapor pressure exists on the warmer side, which forces vapor to the cooler side by diffusion. It is when this diffusion process proceeds rapidly that facets are formed.[1] As vapor diffuses towards the region of lower pressure it sublimates from the relatively warmer grains and condenses onto the colder grain. This process then continues whereby the cold grain releases vapor from its cool side to next cooler

[1]Slower diffusion resulting from lower vapor pressure gradients, typically due to lower temperature gradients, leads to rounding.

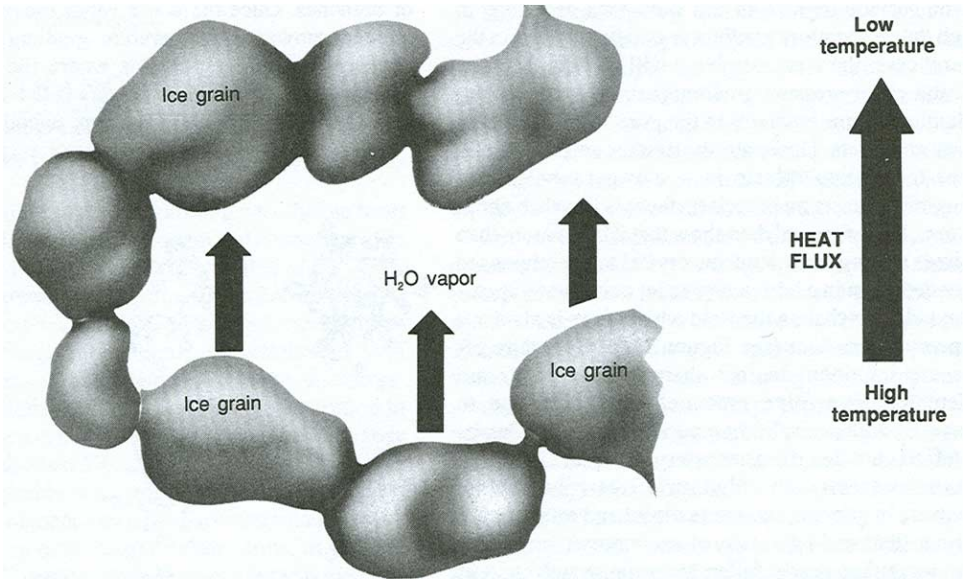

Figure 3. *Hand-to-hand diffusion process prevalent in kinetic metamorphism (Reproduced from McClung and Schaerer [1993]).*

grain thus partaking in the hand-to-hand process. Figure 3 shows a schematic of this process. Condensation on the grains results in various faceted shapes such as plates, needles, sheaths, columns, and dendritic growth. The shape produced is a function of the amount of excess vapor and the temperature at which this process is occurring. Figure 4 shows in the combinations of vapor and temperature where each facet shape is expected.

Aside from imposed temperature gradients, faceted growth is also dependent on several other factors including snow temperature, temperature gradient magnitude, and snow density. Warmer snow temperature increases faceted crystal growth rate because of increased available water vapor. When snowpack temperatures are

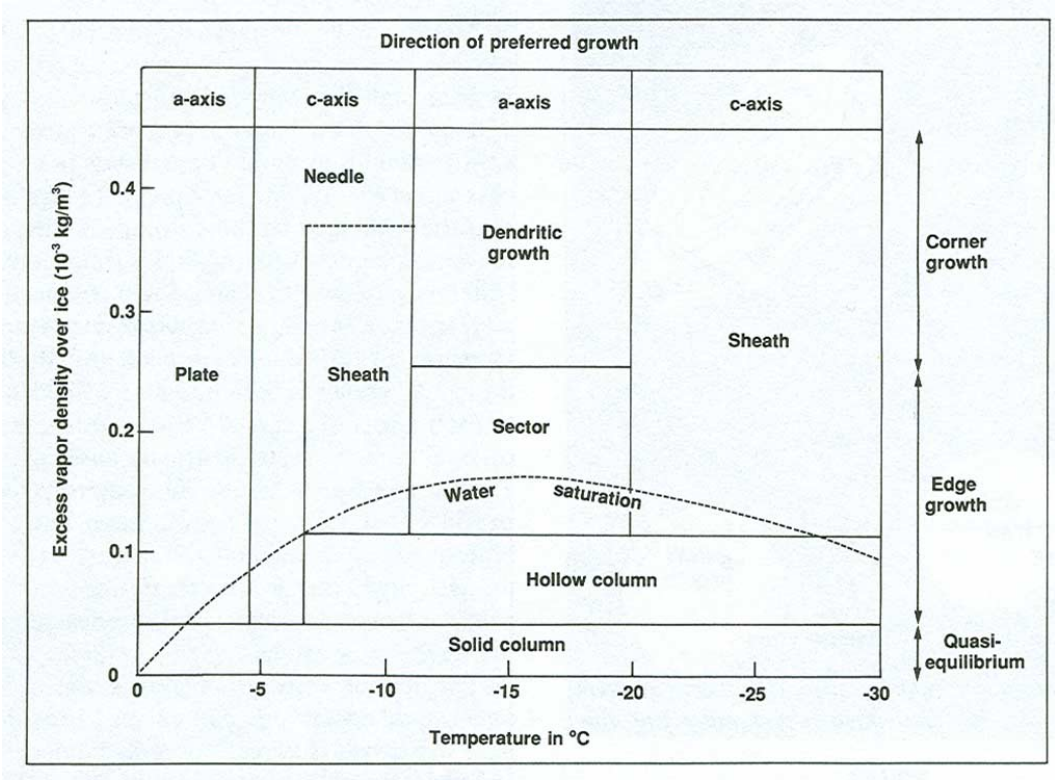

Figure 4. *Preferred snow crystal growth as a function of temperature and vapor density (Reproduced from McClung and Schaerer [1993], Figure 3.5).*

warmer, the inter pore air spaces are capable of holding more vapor mass increasing the amount of condensation in the hand-to-hand process and thus increasing the amount of faceted crystal growth [Colbeck, 1983; Marbouty, 1980]. A snow temperature of approximately $-5\,^{\circ}\mathrm{C}$ was found by Marbouty [1980] to be where maximum growth occurs. As the imposed temperature gradient increases beyond the often cited $-10\,^{\circ}\mathrm{C}/m$ threshold, faceted crystal growth rate increases. Fukuzawa and Akitaya [1993] found this behavior when snow samples were imposed with gradients ranging from $100\,^{\circ}\mathrm{C}/m$ to $300\,^{\circ}\mathrm{C}/m$. Lastly, snow density affects facet formation due to its

geometrical and heat transfer influence. As snow density increases pore space size decreases thereby constricting vapor movement. Snow thermal conductivity is also increased with an increasing snow density because of increased connectedness between snow grains allowing for more efficient heat flow, which is more efficient through the ice network. Increased conductivity transfers heat from warmer to cooler regions more efficiently, which can lower temperature gradients. Lower density snow, often having a lower conductivity, is more insulative and cannot remove built-up heat effectively, creating higher temperature gradients [Yosida, 1960]. To summarize, faceted crystal growth occurs more readily in low density snow (below $350\,kg/m^3$ [Marbouty, 1980]) with relatively warm temperatures and high temperature gradients (above $10\,^{\circ}\mathrm{C}/m$). Figure 5 shows three examples of faceted snow crystals.

Melt-Freeze. When snow reaches $0\,^{\circ}\mathrm{C}$ a three phase mixture is created where the presence of liquid water distinguishes this process from the others. Liquid water is associated with melting snow grains and depending on the water content different crystals form. When liquid water content is low large rounded grains and clusters of grains melting together result. Grains tend to increase in size as larger grains take over and incorporate smaller grains. At high liquid water content slush, which occurs when liquid water fills most of the pore spaces, can be observed. Upon freezing, the metamorphic melting process is stopped until the snow heats up again. This freezing can often result in ice crusts within the snowpack, which can cause adjacent layers to

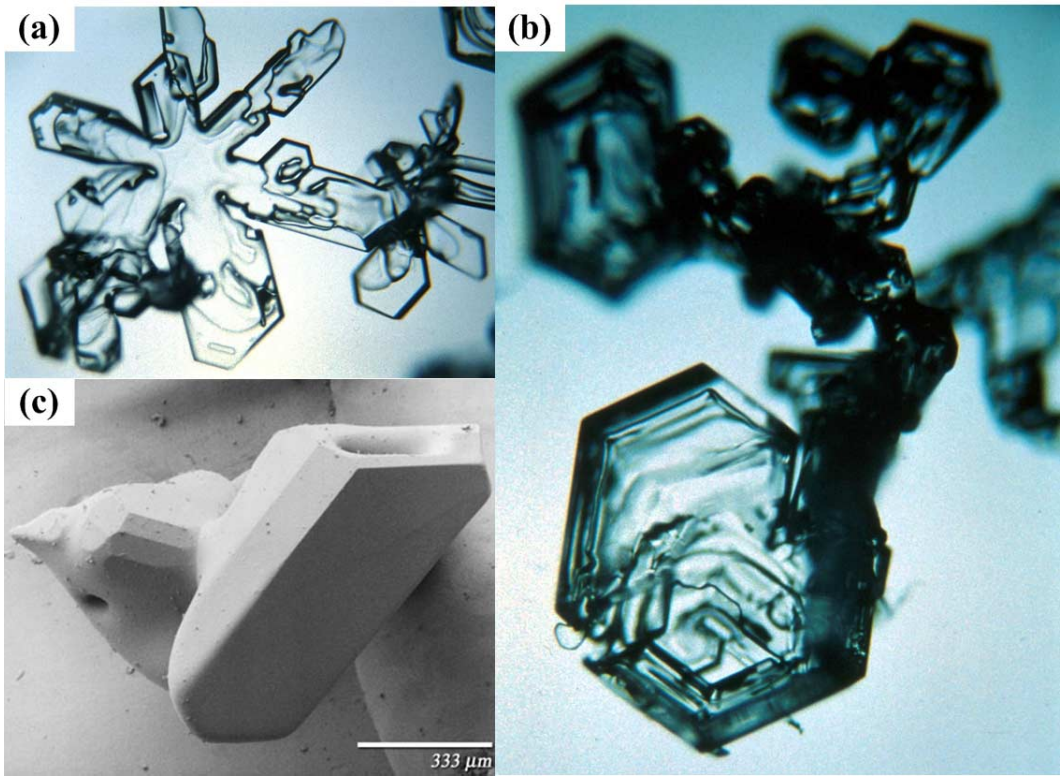

Figure 5. *Examples of facets: (a) near-surface facets after 36 hours (Joe Stock photo), (b) near-surface facets after 24 hours (Joe Stock photo), and (c) Scanning Electron Microscope of a faceted crystal (http://www.anri.barc.usda.gov).*

facet [Colbeck and Jamieson, 2001; Jamieson and van Herwijnen, 2002] creating an ideal weak layer-avalanche running surface scenario.

Characteristics

The following sections describe snowpack characteristics with an emphasis on faceted crystals produced by kinetic metamorphism.

Snow Crystal Classification. A widely accepted system of describing snow crystals is the ICSI[2] classification system [Colbeck et al., 1990], which defines four types of faceted crystals. The first type is given the abbreviation 4fa and represents solid faceted crystals and are usually hexagonal prisms. These crystals are further classified under the kinetic growth process with "strong grain-to-grain vapor diffusion driven by large temperature gradients and excess vapor density above critical value for kinetic growth" [Colbeck et al., 1990]. The second facet type has the symbol 4sf and describes small faceted crystals formed near the surface $< 0.5\,mm$ in size. Birkeland [1998a] observed 4sf grains up to $1.0\,mm$ in size with some grains reaching 1.5 to $2.0\,mm$. The last two remaining facet types are considered mixed forms where both facet and rounds are present. The symbol 4mx is used to describe faceted crystals that are showing signs of rounding due to a decreased temperature gradient. The last facet type has the symbol 3mx and occurs when rounded crystals are starting to show signs of faceting due to an increasing temperature gradient.

All of these facet types can occur anywhere in the snowpack where high temperature gradients are coupled with snow types conducive to growth. In addition to near-surface facets other faceted examples include depth hoar and surface hoar

[2]The International Commission on Snow and Ice

growing respectively, as their names imply, at depth and at the surface. Depth and surface hoar result in faceted crystals with weak inter-granular bonds and therefore weak layers with little shear strength. Depth hoar is formed at depth in a snowpack under sustained temperature gradients in the kinetic regime. Striations and hollow or cup type crystals form in this gradient environment and are described in the ICSI system for three types of depth hoar crystals. Surface hoar is not a result of any of the three metamorphic processes described. When the surface cools below the dew point of the overlying air, condensation occurs resulting in feathery-like faceted crystals growing up from the snow surface. When this growth is covered by subsequent snow it can form a persistent weak layer responsible for many slab avalanches.

Snow Crystal Bonds. Faceted crystals exhibit hexagonal features with weak bonding between grains. As a result of this poor inter-granular bonding, faceted layers are one of the most significant weak layers. Facet layers are often relatively strong in compression, but are weak in shear strength, which makes for weak layers that are unable to resist imposed shear loads. The compressive strength often allows buried facet layers to resist settlement, allowing the layer to remain intact. Facet layers often form persistent weak layers lasting on the order of weeks or longer [Tremper, 2001].

Rounded snow crystals under equilibrium metamorphic conditions exhibit strengthening throughout layers due to increased inter-granular bonding. A process termed sintering refers to how snow and ice crystals bond together below freezing [Colbeck,

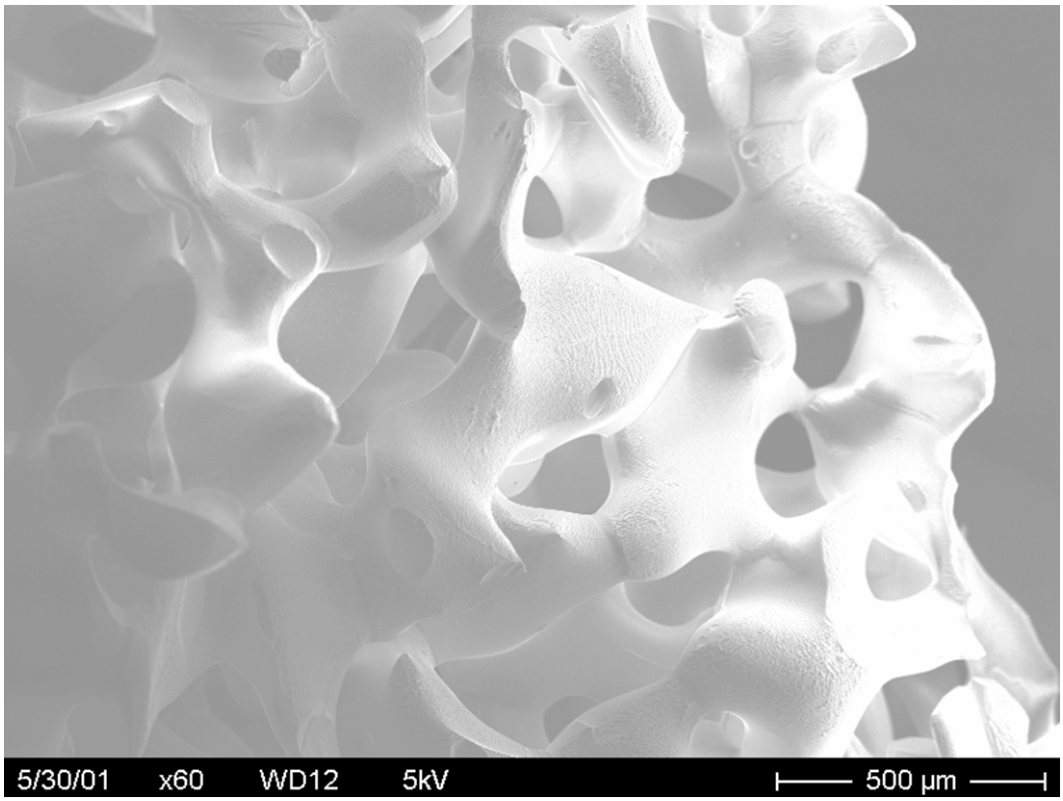

Figure 6. *A Scanning Electron Microscope picture of a sintered snow sample.*

1997]. This process is slow and only proceeds under the equilibrium condition. However, once grains are sintered they form relatively strong layers or slabs in the snowpack. It is when these layers overlay a weaker layer that prime conditions for slab avalanches occur. Figure 6 shows a picture of a sintered snow sample.

Energy Exchange at the Snow Surface

At the snow surface, interactions to stimuli from the atmosphere can be characterized by processes involving the three basic modes of heat transfer consisting of conduction, convection, and radiation. This may be expressed for the top surface layer as

$$Q_M = Q_{SW} + Q_{LW} + Q_H + Q_E + Q_C \tag{2.1}$$

where,

Q_M	=	total heat input flux (energy that is available to change temperature)
Q_{SW}	=	solar absorption flux
Q_{LW}	=	net longwave radiation flux
Q_H	=	sensible heat flux
Q_E	=	latent heat flux due to phase change
Q_C	=	conduction heat flux with layer below surface.

The first two terms, Q_{SW}, Q_{LW}, and the next two terms, Q_H, Q_E, are radiation and convection heat transfer modes, respectively. Q_M represents the total energy balance for the surface layer. When $Q_M = 0$ snow temperature is in equilibrium with no heating or cooling occurring. When $Q_M < 0$ the snow is cooling and when $Q_M > 0$ the snow is warming. Each term in Equation 2.1 is presented in detail in the following discussion.

Shortwave Radiation

Radiation from the sun, known as *solar radiation* or *insolation*, is the primary source of energy forcing atmospheric motions and many different processes in the atmosphere, both at the Earth's surface and in the oceans [Plüss, 1997]. The sun

emits radiation as approximately equivalent to the emission of a blackbody at $5800\,K$. From the Planck distribution, shown in Figure 7, the spectral (wavelength dependent) emissive power of a blackbody at this temperature reaches a maximum in the visible spectrum ($0.40 - 0.75\,\mu m$). In fact, at the top of the Earth's atmosphere more than 99% of this solar radiation exists in the waveband from $0.2 - 4.0\,\mu m$ [Iqbal, 1983]. As solar radiation passes through the atmosphere interactions with molecules and aerosols cause scattering (i.e. Rayleigh and Mie) leading to *diffuse radiation*. The remainder that does not experience scattering is referred to as *direct radiation*. Both the diffuse and direct components reach the Earth's surface and can be combined in one term referred to as *global radiation* [Plüss, 1997]. The global radiation is usually subdivided into several wavelength ranges shown in Table 1. Figure 8 shows the electromagnetic radiation spectrum for the values in Table 1.

At the snow surface a large fraction of the solar radiation is typically reflected. The measure of reflectivity is termed the albedo, α.[3] The amount that is available to penetrate the snow, $1 - \alpha$, attenuates differentially throughout the snowpack depending on the snowpack characteristics. This attenuation can be described by considering how light interacts in a transparent particulate medium through two mechanisms: absorption and scattering. Consider electromagnetic radiation impinging upon a transparent medium. Scattering occurs when this radiation interacts with inhomogeneities in the medium resulting in light changing directions. After passage through the medium some amount of the scattered light exits. The difference between

[3]Discussion of snow albedo is given further attention on page 26.

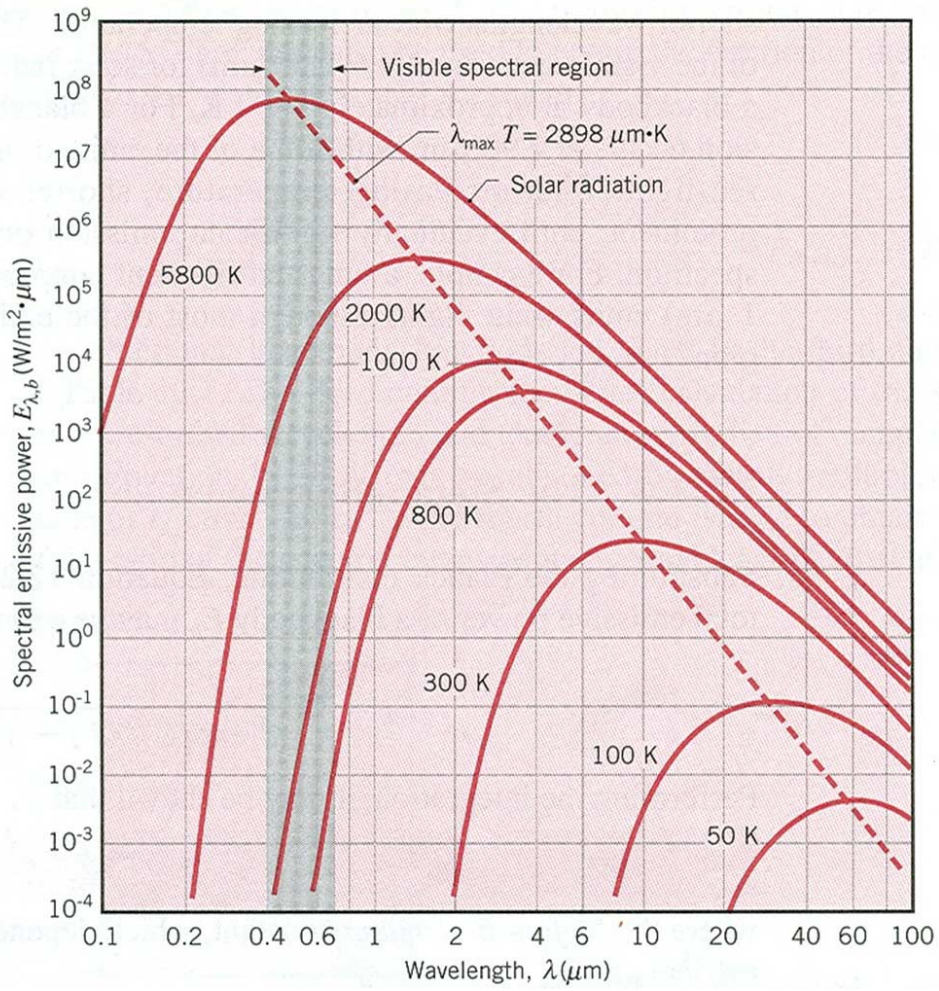

Figure 7. *The Planck distribution shown for selected temperatures and wavelengths. The ordinate axis shows the spectral emissive power as a flux (W/m^2) per wavelength (μm) (Reproduced from Incropera and Dewitt [1996], Figure 12.13).*

Table 1. *Wavelength subdivisions of global solar radiation. Radiative transfer models generally separate* VIS *and* NIR *at wavelengths of either 0.7 or* 0.9 μm *(Reproduced from Plüss [1997]).*

Wavelength (μm)	Name	Mean radiation energy at the Earth surface
0.20–0.40	Ultraviolet (*UV*)	9%
0.40–0.70	Visible (*VIS*)	49%
0.70–5.0	Near-Infrared (*NIR*)	41%

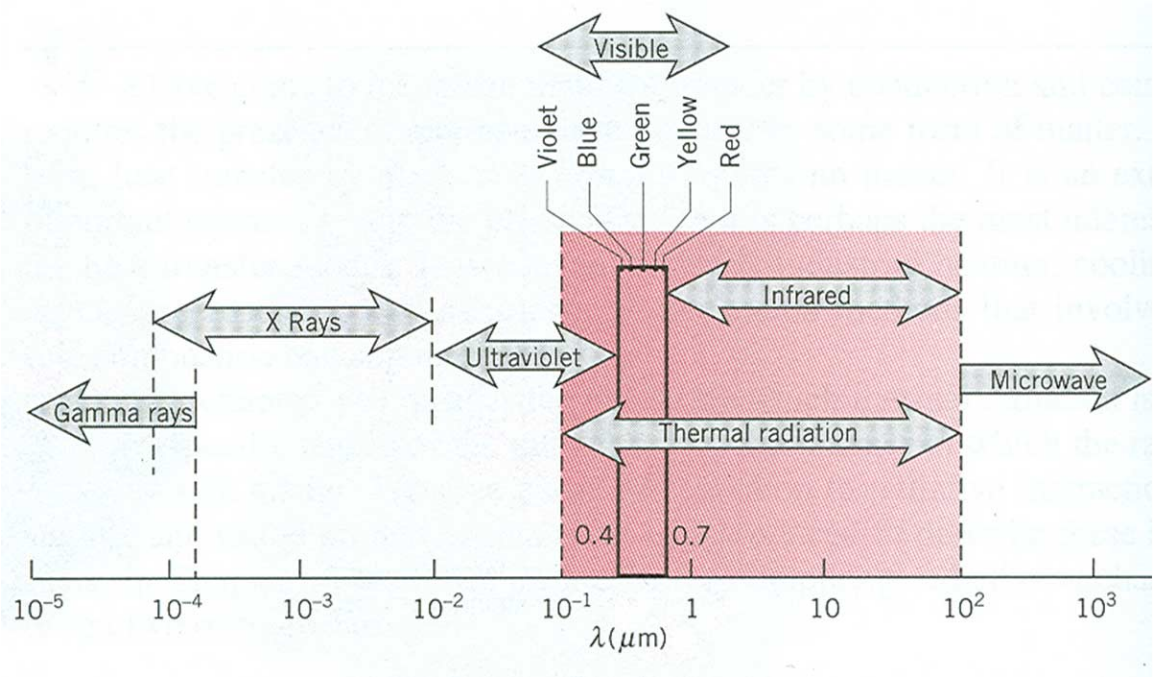

Figure 8. *Spectrum of electromagnetic radiation (Reproduced from Incropera and Dewitt [1996], Figure 12.3).*

the impinging and exiting radiation indicates the amount of radiation absorbed within the medium's constituents. Radiation absorption contributes energy to the medium by raising the internal energy.

The Bouguer-Lambert [AMS, 2004] equation describes attenuation of radiation in a homogeneous medium as,

$$I \downarrow (z + \Delta z, \lambda) = I \downarrow (z, \lambda) \cdot \exp(-\kappa_\lambda \, \Delta z) \tag{2.2}$$

This equation provides a reasonable approximation for determining flux at depth when applied to a snowpack [Brandt and Warren, 1993; Warren, 1982]. The term $I \downarrow (z, \lambda)$ (W/m^2) is the downward solar radiation flux at position z (m) and wavelength λ.

$I \downarrow (z + \Delta z, \lambda)$ is the remaining downward flux after passing through a thickness of Δz from position z in the medium [Warren, 1982]. κ_λ (m^{-1}) is the asymptotic flux-extinction coefficient at wavelength λ. This extinction coefficient is related to absorption and scattering coefficients κ_a and κ_s as,

$$\kappa_\lambda = \kappa_a + \kappa_s \tag{2.3}$$

An extinction coefficient determines the degree of absorption and scattering within a medium. As this coefficient increases, the amount of absorption and/or scattering in the medium increases. The asymptotic extinction coefficient for snow describes a coefficient unaffected by snow surface boundary effects and independent of snow depth [Warren, 1982]. Plots of $\ln |I \downarrow (z, \lambda)/I \downarrow (0, \lambda)|$ versus z are approximately straight lines with the slope equal to κ_λ. This relationship has been observed experimentally in snow using narrow band-pass filters[4] in homogeneous snow of uniform density (e.g. Grenfell and Maykut [1977]). If too wide of a band-pass is used this linear relationship fails because of the changing spectral composition of light at depth within a snowpack. Near the surface the wavelengths of light with high κ_λ values (*NIR*) attenuate rapidly. Wavelengths of light with small κ_λ values (*VIS*) penetrate into the snowpack at greater depth. This effect changes the composition of light from the snow surface to a given depth making the overlying snow an effective filter. At great depths, the last wavelengths to attenuate are near $\lambda = 0.47\,\mu m$ (where κ_λ is

[4]A device that filters out all wavelengths except those within the desired waveband.

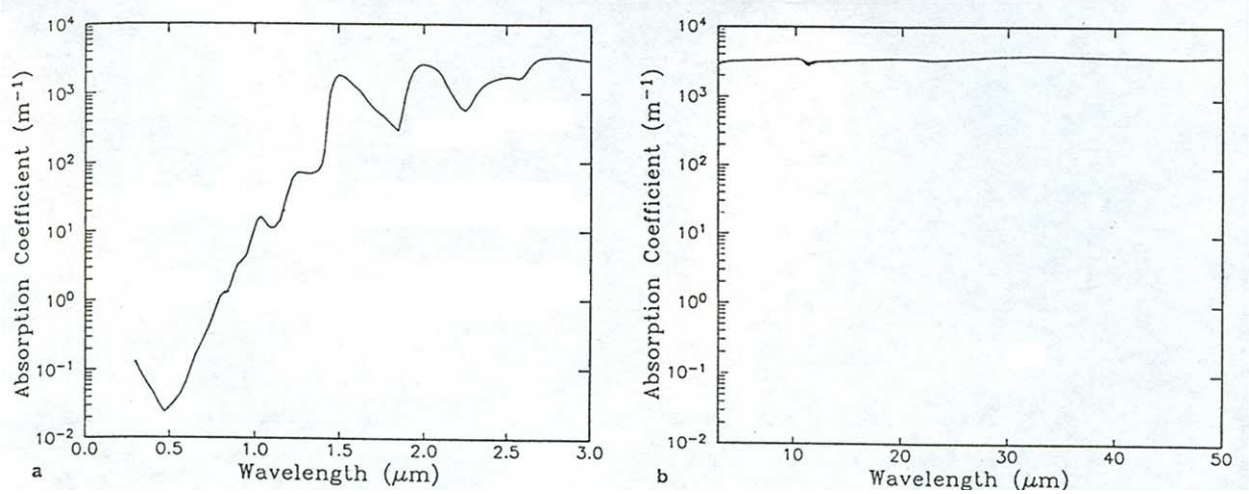

Figure 9. *Absorption coefficient, κ_a, of snow as a function of wavelength, for snow grain radius $100\,\mu m$ and density $400\,kg/m^3$ (Reproduced from Brandt and Warren [1993], Figure 2).*

minimum) explaining the blue tinted light often seen through a thickness of snow [Brandt and Warren, 1993; Warren, 1982].

Figure 9(a) shows typical absorption values for snow in the shortwave spectrum ($0.20 - 3.0\,\mu m$). Notice that nearly five orders of magnitude differentiate absorption between the *VIS* and *NIR* wavelengths. Brandt and Warren [1993] state that of the total amount of solar radiation absorbed in a snowpack, nearly all is a result of the *NIR* being absorbed in the top few millimeters while little *VIS* is absorbed.

Longwave Radiation

Longwave exchange deals with terrestrial radiation in the wavelengths of $5.0 - 100\,\mu m$. The Stefan-Boltzman law describes the amount of emission occurring from

an object above $0\,K$ as,

$$E = \varepsilon\sigma T^4 \tag{2.4}$$

where E (W/m^2) is the emissive flux, σ is the Stefan-Boltzman constant ($\sigma = 5.670 \times 10^{-8}\,W/m^2 \cdot K^4$), T is the temperature of the emitting object, and ε is the emissivity of the body [Incropera and Dewitt, 1996]. Equation 2.4 comes from integration of the Planck distribution (shown in Figure 7) for a given temperature. This distribution shows that higher temperature bodies emit radiation in shorter wavelengths, and that cooler bodies emit in longer wavelengths.

Longwave exchange for snowpacks is a surface phenomenon not directly affecting the snowpack at depth. This can be surmised from Figure 9(b) showing high absorption coefficients in the longwave. Terrestrial radiation is emitted from sources such as carbon dioxide and water vapor in clouds [McClung and Schaerer, 1993; Plüss, 1997]. Clear skies provide the least amount of longwave emission when compared to cloudy skies, which are generally warmer and thus emit more energy. Atmospheric emission contributes energy to the snow surface while the snow surface itself is concurrently emitting longwave radiation to the atmosphere based on its temperature and emissivity. This exchange yields the net longwave radiation and represented by the amount that is received minus the amount emitted by the snow and can either result in the snow surface being heated or cooled. Typically under winter conditions with clear skies, the net longwave radiation lends to the snow surface being cooled.

Turbulent Exchange

Turbulent flux exchange can be classified as a convective transfer mode. It includes the interaction of both latent and sensible heat fluxes occurring at the snow surface. Latent heat flux is driven by vapor pressure gradients between the air and snow surface causing phase change at the snow surface. Sensible heat flux accounts for non-phase change heat transfer between the snow surface and the air and is driven by a temperature difference between the air and snow temperatures. Turbulent fluxes lend to a cooling of the snow surface when the air is colder than the snow surface.

Conduction

A final mode of heat transfer at the snow surface is conduction. It occurs through energy exchanged by direct molecular contact in a direction of decreasing temperature. Fourier's Law (e.g. Incropera and Dewitt [1996]) describes heat flow in a solid and can be written for a one-dimensional case in local form as,

$$q'' = -k_{\mathit{eff}} \frac{dT}{dz} \tag{2.5}$$

where q'' is the heat flow (W/m^2), k_{eff} ($W/m^2 \cdot K$) is the effective thermal conductivity, T (K) is temperature, and dT/dz is the temperature gradient in the z-direction [Incropera and Dewitt, 1996]. The effective thermal conductivity of snow is defined in a continuum sense where it is assumed to be based up an average across many snow grains and grain clusters, which do not explicitly appear in the formulation even though they actually control the thermal conductivity (e.g. Sturm et al. [1997]).

Within a snowpack, heat can propagate by three predominant processes: (1) conduction through the ice lattice, (2) conduction through the air mixture in the pore spaces, and (3) vapor diffusion across pore spaces due to vapor sublimation and condensation. These three modes are usually combined to form an effective thermal conductivity. Conductive heat transfer through snow grains can be approximately 100 times greater than through the pore air spaces [Sturm et al., 1997]. As a result, grain-connectedness increases are coupled with conductivity increases [Adams and Sato, 1993]. Increased connectedness is often coupled with an increased density, which therefore can be used to predict the conductivity to a good degree. Gray and Male [1981] give such a model with the following equation,

$$k_{eff} = 0.021 + 2.5 \cdot \left(\frac{\rho}{1000}\right)^2 \tag{2.6}$$

where ρ (kg/m^3) is snow density and k_{eff} has units $W/m^2 \cdot K$.

Energy Storage

The energy storage term indicates the energy that is added to the snowpack from all contributions. This energy is then available to increase the temperature of the snowpack. Later in this thesis, the time rate of change of this storage term will be relevant in the thermal model. This determination requires knowledge of how fast the snowpack reacts to thermal influences, which requires knowledge of the snowpack's heat capacity.

Heat capacity, C $(J/mol \cdot K)$, is defined as the amount of heat, Q (J), required to increase the temperature, T (K), of a substance by one degree defined as,

$$C \equiv \frac{dQ}{dT} \tag{2.7}$$

Specific heat, c, represents the heat capacity per unit mass of substance and has units of $J/kg \cdot K$ [Incropera and Dewitt, 1996]. Gray and Male [1981] give the specific heat of ice as a function of temperature as,

$$c = 1000 \cdot (2.115 + 0.00779 \cdot T) \tag{2.8}$$

where T (°C) is temperature. A unit conversion factor of $1000\, J/kJ$ was applied to keep units consistent.

Energy Balance Models

Energy balance models are used to determine the effect of the energy components interacting with the snowpack eventually predicting snowpack temperature profiles (e.g. SNTHRM Jordan [1991]). These profiles can then be used to help determine the types of metamorphism that might be occurring within the snowpack. A model initiated by Beddoe [2001] and later expanded by Bristow [2002] provides the starting point for analyzing the energy balance with the intention of investigating near-surface faceting.

Albedo

Albedo, α, is a measure of reflectance of a surface that depends on physical snow properties and the spectral and angular composition of solar irradiance. An all-wave[5] albedo value is calculated as the ratio of the reflected radiation to the incident radiation given as,

$$\alpha_{SOLAR} = \frac{I_r}{I_{atm}} \tag{2.9}$$

where the subscript $SOLAR$ refers to the all-wave $(0.4 - 5.0\,\mu m)$ snowpack albedo and I_r and I_{atm} refer to the reflected and incident shortwave radiation, respectively. This all-wave albedo is a value considering contributions from all wavelengths in the wavebands $0.2 - 5.0\,\mu m$. From the albedo value a portion that is not reflected and that is absorbed may be determined as,

$$I_{a,TOTAL} = (1 - \alpha_{SOLAR}) \cdot I_{atm} \tag{2.10}$$

This equation gives the total amount absorbed throughout the entire snowpack, but yields no information as to how this absorption is actually distributed.

Properties

A comprehensive review of the optical properties including snow albedo was published by Warren [1982] and many other articles have described albedo in detail (e.g. Warren and Wiscombe [1980a,b]; Bohren and Barkstrom [1974]). A brief synopsis

[5] All-wave refers to the entire shortwave spectrum usually in the band $0.4 - 5.0\,\mu m$, which includes both the *VIS* and *NIR* components.

of this review discussing the factors influencing albedo is presented. Snow albedo is primarily dependent upon spectral wavelength, solar zenith angle, impurity concentrations, snow grain size, and snow depth. Figure 10 shows albedo variations relative to these influences.

Spectral Wavelength. Albedo varies across the shortwave spectrum, depending on wavelength. In the UV $(0.20-0.40\,\mu m)$ and VIS $(0.40-0.75\,\mu m)$ wavebands the solar albedo is very high (over 90%), while in the NIR $(0.75-5.0\,\mu m)$ albedo is much lower ($\sim$50%) [Warren, 1984]. Therefore most absorption in a snowpack is due to the NIR component of the solar irradiance. The UV and VIS absorb weakly in snow, which is evident by the blue hue snow exhibits when solar radiation passes through a thickness of snow (e.g. igloo or snow caves).

Solar Zenith Angle. The solar zenith angle, θ, is measured as the angular difference between the outward normal from the snow surface and the vector to the sun's position. When this angle increases, corresponding to a low sun position, the snow albedo increases [Warren and Wiscombe, 1980a; Warren, 1982]. For small zenith angles ($\theta < 50^{\circ}$), the albedo is a weak function of zenith angle [Warren and Wiscombe, 1980a].

Impurity Concentrations. Impurities within the snowpack can greatly alter snow albedo depending on concentration [Warren and Wiscombe, 1980b; Warren, 1984].

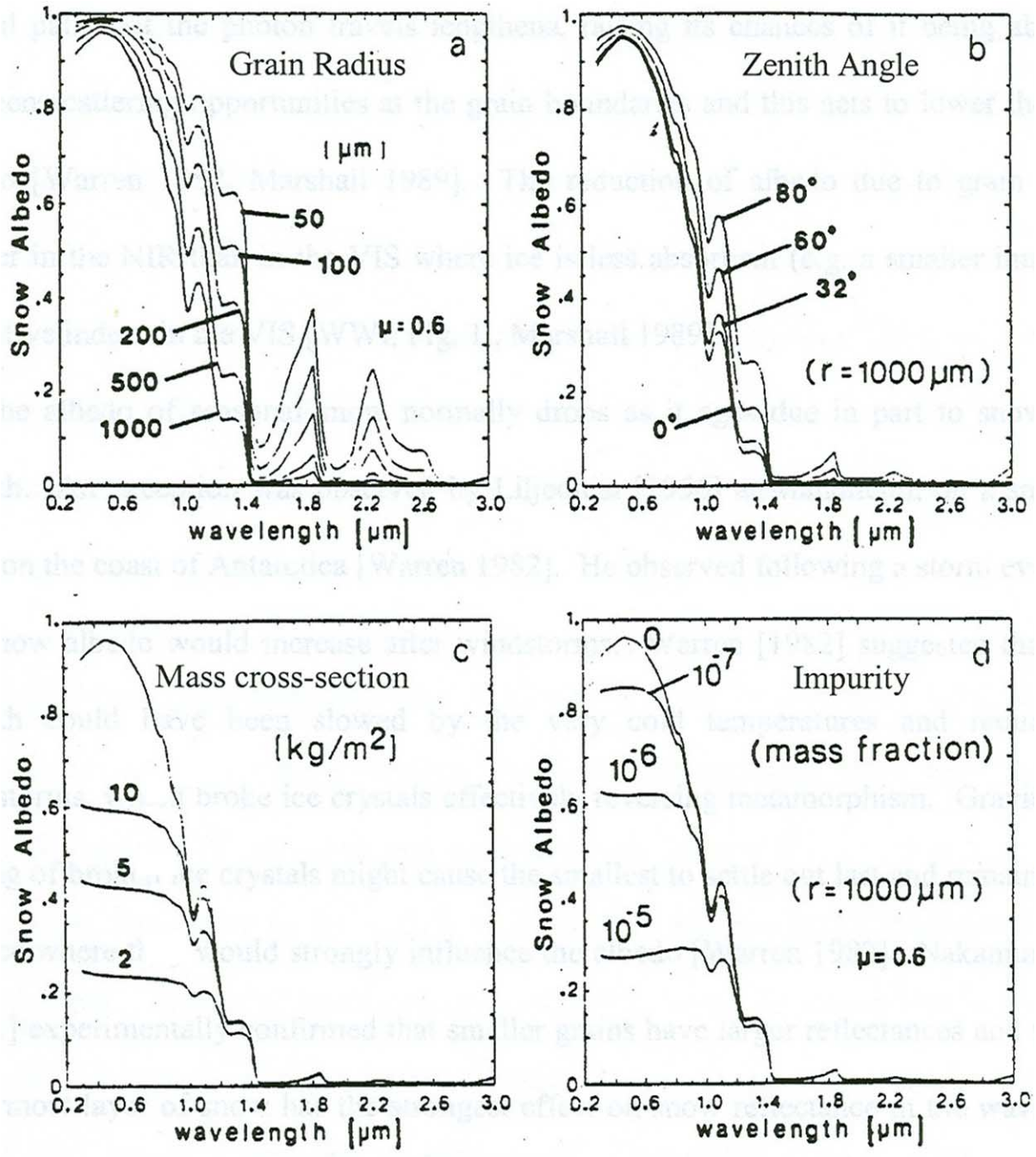

Figure 10. *The influence of (a) grain radius, (b) zenith angle, (c) mass cross-section and (d) impurity concentration (soot) of the spectral albedo of snow (Reproduced from Beddoe [2001]; originally from Marshall [1989] (Figure 2.1)).*

The effect is substantial in the *VIS* wavebands where the impurities act as strong absorbers. This contrasts to "clean" snow where *VIS* light experiences little absorption. Figure 10 shows how albedo can drastically change for increased impurity concentrations from 0 to $10^{-5}\,ppmw$.[6] Some common types of impurities found in seasonal snow are carbon soot, desert dust, and volcanic ash [Warren, 1984].

Grain Size. The snow albedo decreases as the grain size increases at all wavelengths [Warren, 1982]. This correlation can be explained by considering how a photon (light ray) scatters within a snowpack. Scattering occurs when photons cross an air-ice interface and absorption occurs when photons pass through the ice grain. Therefore if the grain size increases an increased chance of absorption results, thereby reducing the snow albedo [Warren, 1982]. An increase in grain size is common in natural snow due to grain growth as snow ages [Marks, 1988]. When specifying grain size an effective grain size is used, which is defined as an optically equivalent grain radius of an ice sphere exhibiting the same optical properties as actual snow grains [Warren, 1982]. Values for the grain radius vary depending on the snow-type. For new snow, the effective grain size is in the range $20 - 100\,\mu m$, fine-grained older snow in the range $100 - 300\,\mu m$, and older snow near melting point in the range $1.0 - 1.5\,mm$ [Warren and Wiscombe, 1980a].

Snow Depth. As the thickness of the snowpack decreases, the optical influence of the underlying surface increases, which can alter the all-wave ($0.4 - 5.0\,\mu m$) snow

[6] $ppmw$ is parts-per-million of impurity on a weight basis.

albedo. If the surface has a lower reflectivity than the snow overlying it, the all-wave albedo could decrease depending on the snowpack thickness. This albedo decrease is caused primarily by a reduction of the *VIS* albedo, which is a result of the *VIS* spectrum being absorbed at the substrate. This absorption only becomes significant when the snowpack's thickness is below a value where the substrate starts to affect the snow albedo. The *NIR* component is unaffected by reductions in snow depth [Warren and Wiscombe, 1980b] since it is typically absorbed in the top few millimeters [Brandt and Warren, 1993]. Albedo may also decrease when impurities are present as mentioned. A layer of impurities beneath a relatively clean snow layer can act as an albedo reducer like the substrate.

To describe the quantity of snow overlying a substrate, a term called the *mass cross-section* is used, which is a function of the snow depth, d_{snow} (m), and snow density, ρ_{snow} (kg/m^3) given as [Marshall, 1989; Beddoe, 2001]

$$m_{xs} = \rho_{snow} \cdot d_{snow} \tag{2.11}$$

The threshold value of the mass cross-section describing the point at which an underlying surface or a layer of impurity is negligible is called the *critical mass cross-section*, $m_{xs,critical}$ (kg/m^2). This term can be thought of as a material parameter for a snow layer with given optical properties. It describes a snow depth, $d_{snow,critical}$, needed to achieve complete attenuation of light through a snowpack with a given volumetric density. The critical mass cross-section may be expressed in a similar fashion to

Equation 2.11 as

$$m_{xs,critical} = \rho_{snow} \cdot d_{snow,critical} \tag{2.12}$$

When $m_{xs,critical}$ is known for the snow comprising a snowpack, the influence of the substrate or impurity can be determined by comparison to the actual m_{xs}. When $m_{xs} > m_{xs,critical}$ the snow albedo reaches its maximum value and the snowpack can be classified as optically semi-infinite meaning that the substrate has no influence. If $m_{xs} < m_{xs,critical}$, the underlying surface or impurity has an influence on the snowpack albedo. In the limiting case where $m_{xs} = 0$, the snowpack does not exist and the albedo simply equals that of the underlying surface. Figure 11 shows the mass-cross section schematically. The critical depth varies for differing types of snow and waveband considered [Marshall, 1989]. In the *VIS* spectrum, values can range from 20 (new snow) to $200\,kg/m^2$ (old melting snow) [Marshall, 1989] while in the *NIR* critical depths are smaller and are generally below $10\,kg/m^2$ [Warren and Wiscombe, 1980a]. Low values for *NIR* are expected because this waveband almost completely attentuates near the snow surface [Brandt and Warren, 1993].

CAR Model

To predict snow albedo, complex optical models based on radiative transfer theory are utilized (some are listed in Warren [1982]). One such model was created by Warren and Wiscombe [1980a,b], which predicted snow albedo as a function of the primary albedo influencing factors listed on page 26. This model requires an extensive amount of computation time and data to obtain snow albedo, which is more involved than

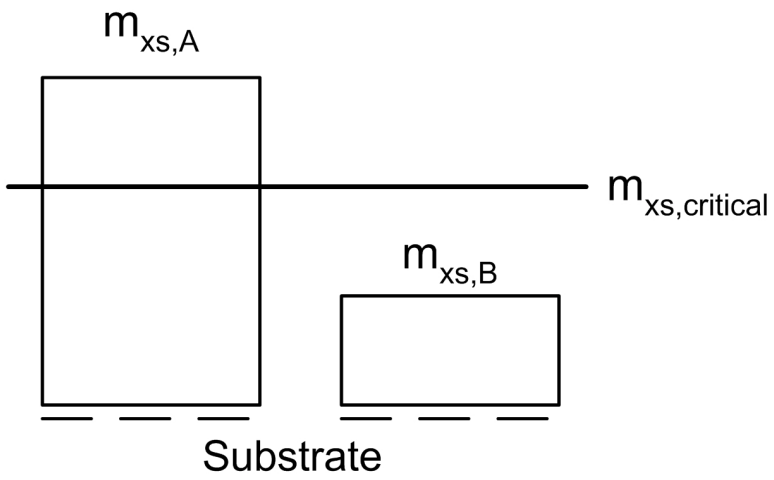

Figure 11. *Schematic showing two snowpacks, A and B, with identical snow properties. The only difference between the two snowpacks is that A is thicker than B. The term $m_{xs,critical}$ is the amount of snow needed to ensure negligible influence from the substrate. Since $m_{xs,A} > m_{xs,critical}$, the substrate has no effect on the albedo value of snowpack A. Conversely, snowpack B is influenced by the substrate because $m_{xs,B} < m_{xs,critical}$.*

convenient for general application. To overcome this fact, Marshall [1989] created a simpler model named SNOALB, which parameterized the model of Warren and Wiscombe [1980a,b]. This model included the most relevant influence factors, yet improved the computation time. SNOALB was initially written in Fortran, but later recoded in C++ by professor R.L. Brown of Montana State University. Beddoe [2001] took this recoded version and modified the program by creating a user interface via input and output text files and applied the model to highways. Bristow [2002] utilized the model by calculating albedo for multiple layered snowpacks on highways allowing distinct snow-type properties in each layer. The current work modified the input files slightly by allowing all unique snow-type layers to be processed in one model

run and added a capability to extract the critical depth values for a given snow-type. Additionally a flag (named *lab*) was added allowing the user to specify whether the model is being applied to natural or laboratory conditions. When the flag was set for laboratory conditions certain assumptions are made, which are described in the ensuing discussion. The source code is listed in Appendix B. For details regarding the snow albedo parameterization refer to either Beddoe [2001] or Marshall [1989].

CAR essentially calculates an all-wave, *VIS*, and *NIR* albedo of a snow layer overlying a substrate with known albedo in the *VIS* and *NIR* wavebands. The inputs required in CAR are similar to those required in SNOALB and can be divided into snow and atmospheric parameters. The atmospheric inputs include the following: solar zenith cosine ($\cos\theta$), atmospheric pressure ($mbar$), diffuse fraction for *VIS* and *NIR*, surface downflux for *VIS* and *NIR*, and atmospheric transmittance for *VIS* and *NIR*. The snow inputs include snow grain radius (μm), snow density (kg/m^3), impurity concentration (mass fraction; $ppmw$), mass cross-section (kg/m^2), and underlying surface albedo in both the *VIS* ($\alpha_{SUB,VIS}$) and *NIR* ($\alpha_{SUB,NIR}$) wavebands. In addition, CAR included an option named *iwvl* to specify the breaking point between the *VIS* and *NIR* wavebands as either 0.7 or $0.9\,\mu m$. The flag *lab* was set to either a lab or natural setting to use corresponding default parameter values. The atmospheric pressure and transmittance are used to calculate the diffuse fraction, which describes the fraction of irradiance that is diffuse. The surface downflux parameter indicates the fraction of irradiance existing in the *VIS* and *NIR* wavebands, which are set to

default values unless specified. When *iwvl* was set to break at $0.7\,\mu m$, default surface downflux values are 0.46 for the *VIS* and 0.54 for the *NIR*. A sensitivity study was performed by Beddoe [2001] investigating the influence of snow grain size, underlying surface albedo, zenith angle, and diffuse fraction input parameters on the albedo (see Beddoe [2001] Chapter 3, p.71–74).

Outputs from CAR included snow surface spectral albedo values in the *VIS* and *NIR* wavebands, an all-wave solar albedo (α_{SOLAR}), critical depth values in the *VIS* and *NIR* wavebands, and a calculated extinction coefficient (described in detail on page 61). Both the calculation of the critical mass cross-section and the extinction coefficient were added to CAR from this thesis project.

Near-Surface Facets

As outlined by Birkeland [1998b] most research attention regarding faceted weak layers had been focused on depth hoar and surface hoar. Until recently little attention has been given to the formation of near-surface facets, which as discussed, can form dangerous weak layers. Birkeland [1998b] described three predominant known processes resulting in the temperature gradients driving kinetic growth metamorphism and thus faceted crystals, including radiation recrystallization, melt-layer recrystallization, and diurnal recrystallization. These processes are not necessarily distinct, as combinations are possible.

Radiation Recrystallization

This process is characterized by a balance between shortwave radiation and net longwave radiation creating faceted snow in the top few centimeters as shown in Figure 12 [LaChapelle, 1970; Armstrong, 1985; Birkeland, 1998a,b]. Shortwave radiation irradiates the snow surface with some portion absorbing at depth in the snowpack. Concurrently net longwave radiation loss cools only the surface [Brandt and Warren, 1993] thus providing a heat sink. It is also possible to have cooling at the surface from turbulent flux exchange. Low density snow is usually considered to be a necessity for this process due to its relatively insulative behavior, which causes heat added by solar absorption to build-up. Conversely, higher density snow having a higher conductivity moves heat quickly causing lower heat build-up. With the combination of low density snow and a cool surface, large temperature gradients result, leading to large vapor pressure gradients, which can force the upper snow layer into the kinetic growth metamorphic regime ($> 10\,^{\circ}\mathrm{C}/m$). Vapor gradients as high as $50 - 100\,mbars/m$ can cause significant recrystallization, resulting in facets within hours (the kinetic-to-equilibrium threshold vapor pressure gradient is about $5\,mbars/m$ [Armstrong, 1985]). The amount of solar absorption in the snowpack can also lead to the formation of melting snow at depth. As night approaches this melting can freeze and create a melt-freeze crust within the snow. Temperature gradients associated with this process are negative, meaning that the snow is warmer at depth with a cooler surface. Birkeland [1998b]

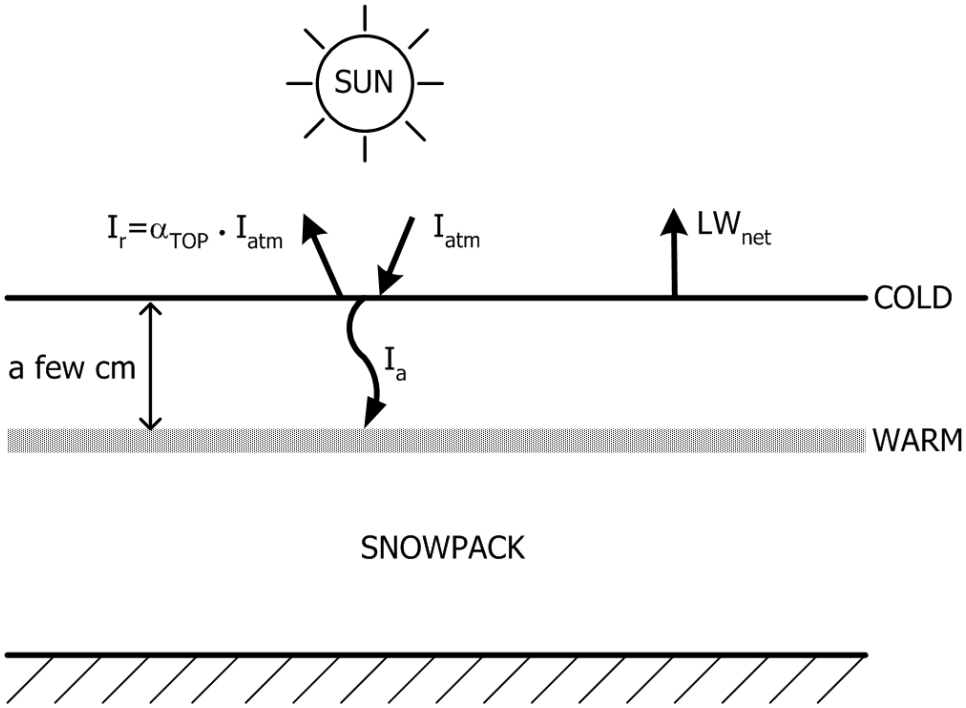

Figure 12. *The radiation recrystallization process forms near-surface facets when a balance between shortwave and longwave radiation exchange is achieved. Shortwave radiation absorbs at depth within the snowpack causing heating. Concurrently net longwave radiation loss cools only the snow surface creating a temperature gradient between the cool surface and warm sub-surface (Reproduced from Birkeland [1998b] Figure 1).*

notes that crystal forms typically observed include 4fa, 4sf, or a more advanced facet form of 5cp crystals (hollow or partly solid cup-shaped) [Colbeck et al., 1990].

Melt-Layer Recrystallization

Another process creating near-surface facets is the melt-layer recrystallization process where a melt-layer forms as a result of absorbed radiation, rain events or heating of the snow from turbulent flux exchange (Figure 13) [Birkeland, 1998b; Jamieson and van Herwijnen, 2002; Colbeck and Jamieson, 2001]. If additional snow

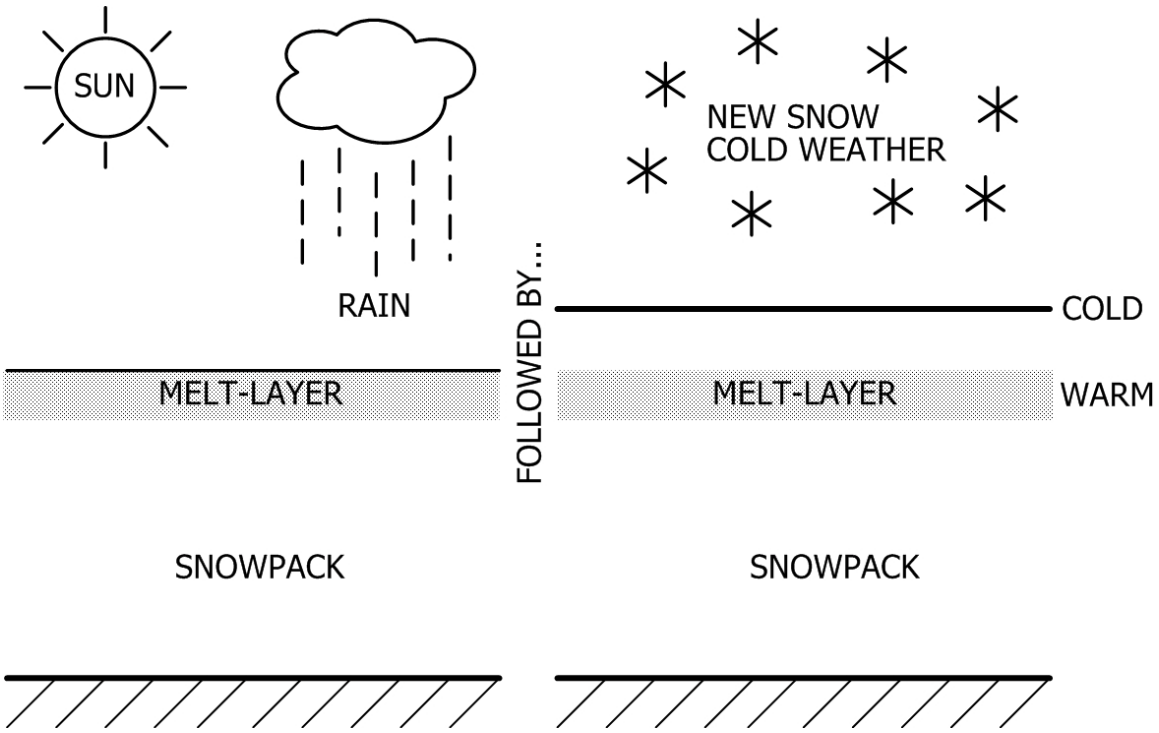

Figure 13. *The melt-layer recrystallization process forms near-surface facets when a surface melt-layer formed by solar absorption or a rain event is buried by new snow. At night net longwave radiation loss cools the surface of the new snow setting up a large temperature gradient along with the relatively warmer melt-layer (Reproduced from Birkeland [1998b] Figure 2).*

falls on top of this melt-layer, significant temperature gradients can occur [Birkeland, 1998b]. This melt-layer stays at 0 °C, sustained by the released latent heat during the refreezing process. With a temperature near 0 °C and a large vapor supply, the melt-layer scenario can grow near-surface facets rapidly [Jamieson, 2000; Colbeck and Jamieson, 2001]. Fukuzawa and Akitaya [1993] observed the formation of 1 mm faceted crystals over the period of one night due to temperature gradients of $100 - 300\,°\mathrm{C}/m$ caused by a melt-layer covered with 2 cm of fresh snow.

Diurnal Recrystallization

The third process, diurnal recrystallization, creates near-surface facets as a result of large swings in the snow surface temperatures between night and day (Figure 14). During diurnal cycles only the top $30\,cm$ of snow significantly changes temperature while below this depth, temperature varies little [Armstrong, 1985]. At the $30\,cm$ depth a diurnal average was approximated and was considered to remain relatively constant [Birkeland, 1998b]. During the day the snow surface typically warms from solar absorption. This warming sets up a positive temperature gradient between the warm surface and relatively cool diurnal depth averaged temperature. The reverse can occur at night when the heating sources are no longer available. Instead net longwave cooling occurs at the snow surface which can rapidly cool the snow surface. A negative temperature gradient is achieved between the now cool surface and the relatively warm diurnal depth temperature. In southwest Montana, Birkeland et al. [1998] observed this process experimentally and found near-surface facets about $1\,mm$ in size forming in about 36 hours. Temperature gradients were measured at $200\,^{\circ}\mathrm{C}/m$ at night and $100\,^{\circ}\mathrm{C}/m$ during the day. Once this layer was buried 9 days of avalanche activity involving this weak layer was observed. In the Swiss Alps, Fierz [1998] observed similar near-surface facet formation caused by diurnal recrystallization, which persisted in the snowpack for several months.

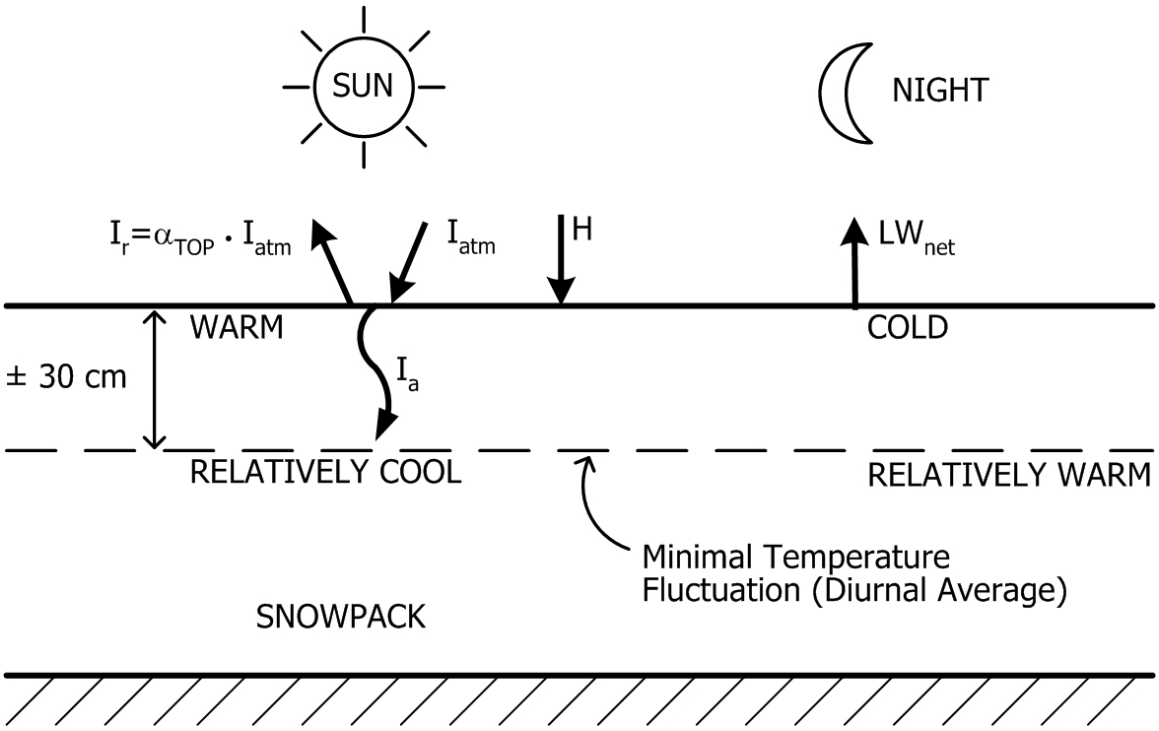

Figure 14. *The diurnal recrystallization process forms near-surface facets as a result of large surface temperature swings. A temperature gradient is created from the surface temperature and the diurnal depth temperature where temperature varies little. During the day solar absorption and sensible heat fluxes warm the snow surface creating a positive temperature gradient while at night the surface is cooled by net longwave exchange (Reproduced from Birkeland [1998b] Figure 3).*

CHAPTER 3

METHODOLOGY

Within this section the instrumentation and computer models used to perform the current research are presented. The models utilized, include the Computational Albedo Routine (CAR) and the thermal model. Appendices A & B contain the source code for both of these models.

Instrumentation

Environmental Chamber

In an attempt to carefully monitor and study the formation of near-surface facets a refrigerated environmental chamber (EC) was utilized, which enabled controlled conditions that are not attainable in a field study. The chamber consisted of an insulated room with the following dimensions: $2.5\,m \times 2.5\,m \times 2.5\,m$. Figure 15 shows the access door to the chamber. The chamber mimicked actual atmospheric conditions through the following components.

Solar Simulation. A metal-halide (MHG) lamp (Figure 16) supplied from K.H. Steuemagel (KHS) provided the solar simulation source. According to KHS, the MHG lamp produces "a dense multi-line spectrum of the rare earths that is comparable to a continuous spectrum" [KHS, 2001]. The MHG provides a spectral distribution close

Figure 15. *Montana State University's Cold Regions Lab environmental chamber.*

Figure 16. *KHS metal-halide global solar lamp as used in the environmental chamber.*

to the atmospheric solar spectrum. The standard for artificial solar spectral irradiance is outlined by the International Commission of Illumination (CIE) contained in Publication 85 [CIE, 1989]. Figure 17 shows CIE's standard as well as the percentage of light in various wavebands. Figure 18 shows the MHG lamp compared to the CIE standard.

The lamp is computer controlled through a program used to run the environmental chamber. Variation in lamp irradiance was achieved by adjusting power input. Filtration was combined with the adjustable power resulting in room radiance values ranging from 1-100% of the total lamp power, which was around $1140\,W/m^2$ measured $\sim 1\,m$ from the lamp. A total of fifteen separate filter and power settings were available to achieve the many radiance combinations. Four filters were installed providing the following filtration percentages: 43, 57, 68, and 78%. These filters consisted of sliding meshed screens that moved in front of the solar lamp thus blocking some of the irradiance.

Longwave Simulation. Longwave radiation exchange with the atmosphere was simulated in the EC by a cooled ceiling panel. The panel was run separately from the chamber's room temperature allowing for a significantly cooler ceiling that was capable of attaining $-40\,^{\circ}\mathrm{C}$ when the room temperature was set at $-10\,^{\circ}\mathrm{C}$. The panel itself consisted of a steel plate painted with a matte black finish approaching blackbody behavior.[1] A series of copper coils behind the plate provided the cooling

[1]For a matte black painted surface the emissivity, ε, value is approximately 0.98.

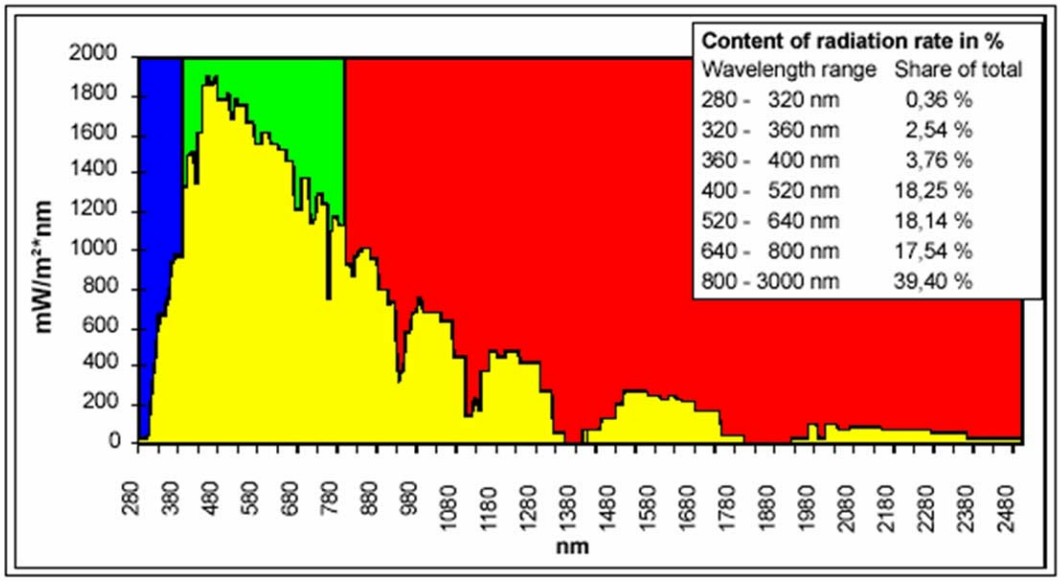

Figure 17. *CIE standard for artificial solar lamps showing the recommended spectral distribution of simulated solar radiation (Reproduce from Publication 85, Table 4 [CIE, 1989]).*

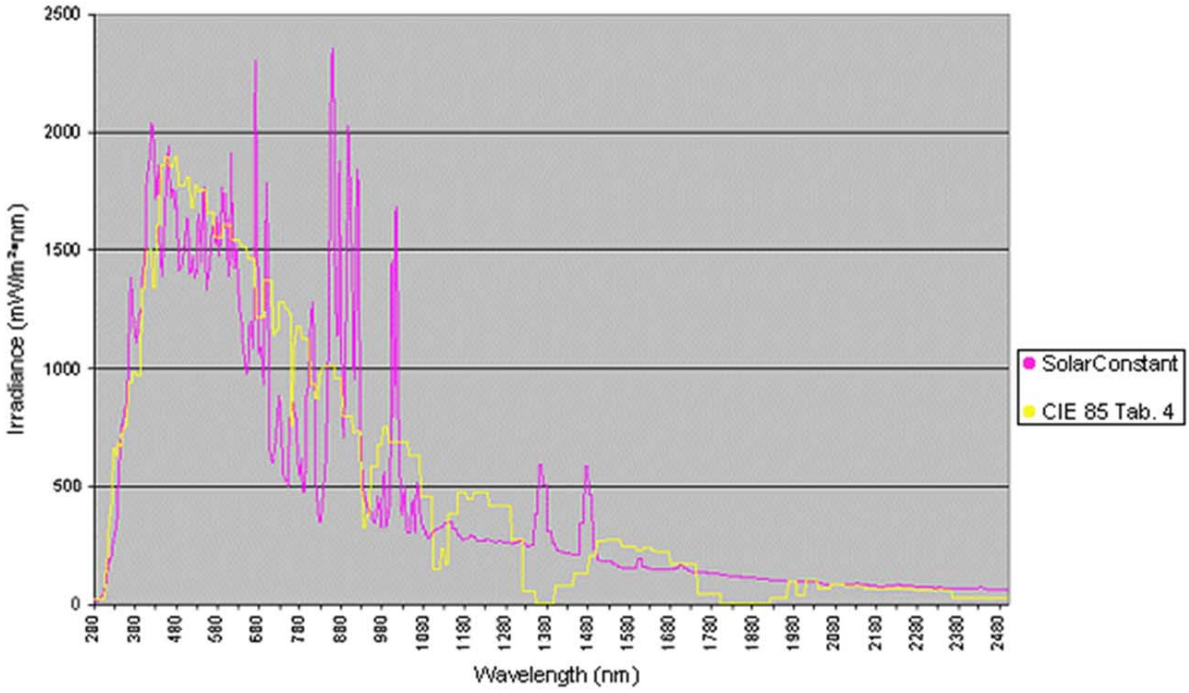

Figure 18. *Comparison of a measured solar irradiance to the CIE recommended irradiance standard.*

to a desired temperature. Condensation frequently formed on the panels because the temperature of the plate was below the dew point temperature of the room. Performance of the plate was not altered significantly due to this occurrence since snow and similarly frost behaves as a blackbody in the longwave region of the spectrum [Warren, 1982; Plüss, 1997]. The longwave panel spans across the top of the chamber and has a cutout for the solar light source to irradiate the room. A special, low absorption pane of insulative glass provided a transparent medium for the solar lamp to irradiate the chamber. Figure 19 shows the panel with a small of amount of frost on the surface.

Figure 19. *Longwave simulation panel mounted on the chamber's ceiling. Note the condensation on the ceiling panel. The solar lamp is shown in the upper right.*

Chamber Conditions. Temperature within the room, controlled by the EC's computer, had an accuracy of $\pm 0.5\,^{\circ}\mathrm{C}$. Fans drawing air over refrigerated coils provided

the means of cooling. Air velocity in the room was measured using an Omega digital handheld anemometer for a set fan speed, which was not altered throughout the study. Relative humidity was recorded near the outlet of the fans utilizing a bulb type instrument. A spray mister located upwind of the fans provided the means to increase humidity in the room, however this feature was not used. Humidity could not be lowered in the room to a set value, but was nonetheless measured and accounted for in the study. The only time that the humidity lowered in value was for the case described above when condensation would occur on the panel. This condensation effectively removed humidity from the chamber by frosting the panel.

Irradiance Measurements

Measurement of the shortwave and longwave radiation fluxes were taken for each experiment. Shortwave radiation measurements were performed using an Eppley Laboratories, Inc. Precision Spectral Pyranometer (PSP). This device measured incoming hemispherical shortwave radiation in a waveband from $0.285\,\mu m$ to $2.8\,\mu m$. Voltage output from the PSP was measured and used along with the device's sensitivity (approximately $9\,\mu V/W \cdot m^{-2}$) to obtain an all-wave irradiance over the waveband.

Longwave measurements were obtained using an Eppley Precision Infrared Radiometer (PIR), which measures total, all-wave irradiance in a waveband from $3.5\,\mu m$ to $50\,\mu m$ with a sensitivity of $4.31\,\mu V/W \cdot m^{-2}$. The PIR is essentially a type of pyrgeometer, which is a device used to measure global longwave terrestrial radiation. A

voltage output from the device divided by the sensitivity gave the net longwave radiation, R_{net}. The radiation emission of the device was taken into account by recording resistance output of a thermistor. From the known resistance value a device or case temperature (T_{case}) was calculated using a manufacturer provided equation. The resulting longwave radiation input into the device accounting for the case temperature was calculated as

$$R_{in} = R_{net} + R_{out} = Voltage/Sensitivity + \sigma \cdot {T_{case}}^4 \tag{3.1}$$

This value represents the total incoming longwave radiation emitted from the cooled ceiling, the glass pane for solar lamp, the solar lamp itself and the surrounding chamber walls. This method of obtaining the longwave irradiance flux, ($Q_{LW,IN}$), was one of two methods outlined by the manufacturer and is considered the most accurate of the two Eppley Laboratories, Inc.. The other method, referred to in the literature as the "simple" method, involved measuring compensated pyrgeometer output, which required a battery as an internal power source. This measurement required measuring only one voltage from the instrument.

Reflectivity Measurements

Obtaining an energy balance of a snowpack requires a good prediction of solar radiation energy transfer, which implies knowledge of the snow albedo. Measurement of reflectivity or albedo allows calculation of how much solar radiation has been absorbed into the snowpack. Once the total absorbed amount is known it can

be distributed throughout the snowpack with depth, which aids in thermal modeling efforts. Knowing snow reflectivity allowed for further validation of the CAR snow albedo model. Generally reflectivity measurements are made using a spectrometer (spectral radiometer), measuring spectral reflectance of objects. If the amount measured is then spectrally integrated, a total reflectance can be found for desired wavebands such as the shortwave band from $0.40\mu m$–$0.70\mu m$.

A HyperSpectral Imaging System (HSI) (Figure 20) from Resonon, Inc. was used to measure reflectivity of snow samples. This device is a type of spectrometer akin to a digital camera that is able to take individual pictures of the snow at distinct wavebands. The wavebands were all located within the visible region of the spectrum in the range $0.42 - 0.90\,\mu m$. Two lamps on either side of the camera provided diffuse illumination while the camera scanned images with a moving stage. The camera's image files are called a datacube, which store for each pixel spectral data. The datacube can be post-processed to achieve an average reflectance by selecting an area of the image. The selected area contains numerous points for which spectral data are available. Taking an average across all of these points provides a spectral average across the area. The resulting spectral information was then taken and averaged over the desired waveband to provide a direct comparison to the CAR reflectivity model. In this manner, the HSI behaved similar to a conventional spectrometer. Since the HSI was on loan for a limited time it was not available for most of the experimental study.

Figure 20. *HyperSpectral Imaging System from Resonon, Inc.*

Insulated Snow Box

Snow samples subjected to thermal conditions in the environmental chamber were contained within an insulated box with dimensions of $60\,cm \times 60\,cm \times 40\,cm$ (L×W×D) (see Figure 21). Two inches of pink polystyrene insulation lined the sides of the box reducing lateral heat conduction. A plywood shell was built around the insulation to provide rigidity during transport. A $\sim 1.5\,mm$ sheet of 6061-T6 aluminum was used as the bottom of the box allowing for efficient heat conduction from an imposed bottom boundary condition.

Figure 21. *The insulated snow box and boundary condition plate used in experiments.*

Lower Boundary Condition Plate

Control of the bottom boundary condition underlaying the snow sample was necessary to approximate actual field conditions as well as to provide a known boundary condition for the thermal model. Several boundary condition types were considered for the experimental study. A Dirichlet or specified temperature boundary condition was chosen for ease of instrumentation. A Neumann or specified heat flux boundary condition required more sophisticated instrumentation to create a constant flux. An insulated or zero flux boundary condition was also considered, but was eliminated because it does not closely correspond to natural thermal conditions.

A Dirichlet condition was created by making a heat exchanger surface, cooled and heated as necessary by a coolant fluid (propylene glycol). The exchanger consisted of a serpentine assembly of copper tubes connected to aluminum Thermofins^{TM} composing a flat boundary surface (see Figure 21). The Thermofins, intended for radiant floor heating installations, allowed for efficient heat transfer from the copper tubes to the boundary surface. The fins essentially spread out the heat from the copper tubes creating a uniform, constant temperature surface. The underside of the plate with exposed copper pipes was insulated with polystyrene to minimize any thermal disturbances.

Cooling and heating of the coolant was achieved with a VWR Scientific Products heated/refrigerated circulator bath shown in Figure 22. The chiller consisted of a circulated bath with heating and cooling elements that allowed for precise control

of fluid temperature. Temperature accuracy of the chiller bath was verified using a mercury glass-bulb thermometer. A constant temperature value was chosen for each experiment and was maintained within 1/10 °C. The fluid in the bath was constantly pumped through the copper tubes and was cooled or heated depending on the adjustment necessary. The cooling fluid in the bath was DowFrost© propylene glycol with a 50% mixture of deionized water.

Figure 22. *VWR Scientific Products heated/refrigerated circulator.*

Temperature Measurement

Thermocouple Sensors. An array of thermocouples provided temperature measurement throughout the snow sample in the insulated box. The array, shown in Figure 23, consisted of a drilled piece of wood and mylar-wrapped hematocrit glass tubes ($1.2\,mm$ diameter) inserted into each hole. Tubes were spaced from $+1\,cm$ to $-10\,cm$ relative to the snow surface in one centimeter increments. Below $-10\,cm$, tubes

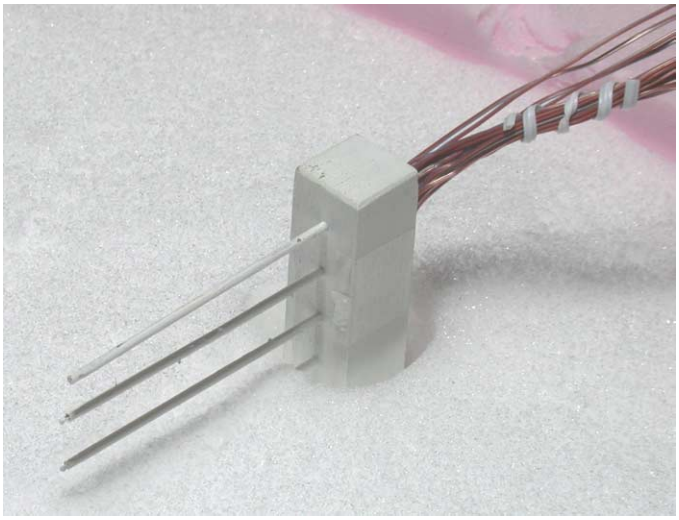

Figure 23. *Thermocouple array used to measure snowpack temperature profiles.*

were placed in five centimeter increments at the following depths: $-15, -20, -25, -30, -35, -40\,cm$. Thermocouples were threaded into each glass tube until the sensor head was exposed. Once completely assembled, the array was then coated with white acrylic paint in an effort to minimize solar contamination on the thermocouple measurements. The paint also ensured that snow immediately around the array would not melt due to absorbed shortwave energy within the array. Wood and glass were selected for the array because both had thermal conductivities closely matching snow, which eliminated unwanted heat conduction near the array. Thermocouples were also placed in the boundary condition plate and in the chamber to measure the air temperature. The air thermocouples were shielded with an enclosure blocking out radiation from the solar lamp to prevent solar contamination.

Type T thermocouples were selected for the study because of good performance in the intended temperature range from 0 to $-20\,^{\circ}\mathrm{C}$ [Omega Engineering Inc., 2003]. The thermocouples, purchased from Omega Engineering, Inc. were 30 gauge wires with a special limits of error (SLE) designation. The SLE thermocouples have an ANSI error standard of the greater of $0.5\,^{\circ}\mathrm{C}$ or 0.4% of a given temperature measurement [Omega Engineering Inc., 2003]. Beads at the ends of the thermocouples were created using a thermocouple welder ensuring a good mechanical contact between both wires. Short sections of this wire were run to a type T connector joining type T thermocouple extension wire. The extension wire was run to a data acquisition system to record temperature. Thermocouples measure voltage difference from two contacting dissimilar metals, which for type T thermocouples consist of a wire made from Copper and a wire made from Constantan. Fluctuations in temperature at the joined wire interface causes an electromotive force creating a voltage difference that is termed the Seebeck effect [Kerlin, 1999; Beckwith et al., 1993].

A calibration routine was performed on the thermocouples to check accuracy. Thermocouples were placed into the chiller used to control the boundary condition. Several chiller bath set-points were set and corresponding temperature readings were recorded from the thermocouples. Deviations from the constant bath temperatures were compared to find an offset for each individual thermocouple. Results showed a consistent offset for each set temperature point per thermocouple. This offset was then utilized when measuring snow temperatures during experiments. Figure 24 shows

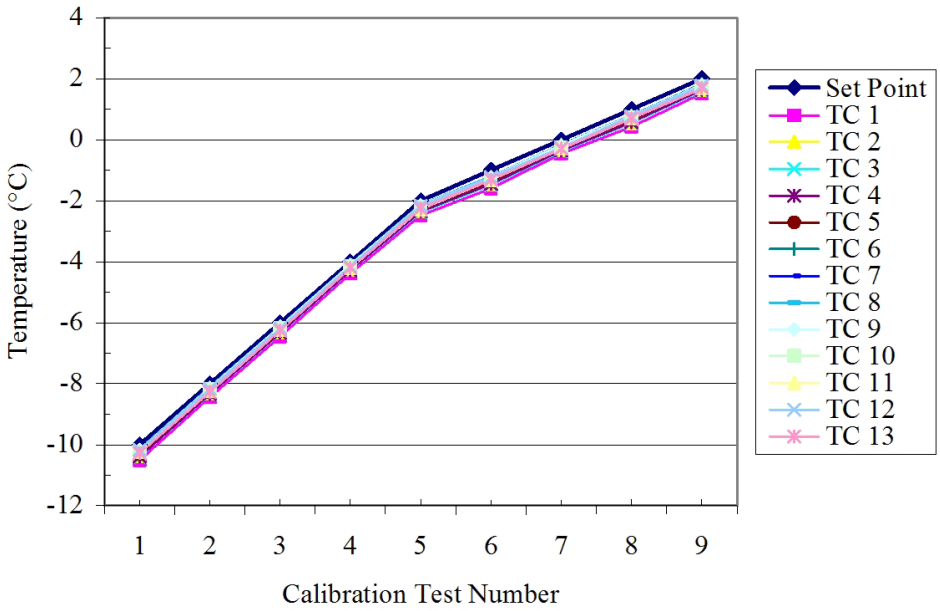

Figure 24. *Typical thermocouple offsets from actual measured temperature during calibration. Offset errors were no greater than* $0.5\,^{\circ}C$ *for all of the temperatures measured.*

a typical calibration curve displaying the actual chilled bath temperature and the individual thermocouple temperature measurements. Notice that for all temperatures tested, the thermocouples were off by less than 0.5 °C.

Infrared Temperature Sensor. An Everest Interscience Model 4000-4ZL infrared temperature sensor was used to provide an additional temperature measurement at the snow surface. An Infrared (IR) sensor is not affected by solar loading like thermocouples and as a result provides an accurate temperature reading. The IR sensor was mounted on a tripod about $0.5\,m$ above the snow surface as shown in Figure 25 and was aligned by line of sight from the sensor's IR port to the snow surface. The

sensor, requiring a $12\,V$ power source, had an accuracy of $\pm 0.5\,^{\circ}$C once calibrated. Calibration was performed by creating an ice-bath, which when well mixed exists at $0\,^{\circ}$C. The IR sensor had an emissivity compensation ranging from values of 0.2 to 0.98 depending on the material that the sensor is reading. Snow has an emissivity of 0.985-0.990 [Dozier and Warren, 1982; Plüss, 1997; Warren, 1982], which is a close approximation of a blackbody in the infrared $(4-100\mu m)$ region of the electro-magnetic spectrum [Berger, 1979]. The water and ice in the ice-bath also approximate blackbody behavior and as a result a calibration using an ice-bath also allows for accurate temperature measurement with dry snow. Using the $0\,^{\circ}$C temperature from the ice-bath, a voltage output from the IR sensor was recorded. This output was converted to a temperature reading utilizing the sensor's sensitivity $(10\,mV/\,^{\circ}\mathrm{C})$ and any value beyond the ice-bath temperature was corrected by applying a compensatory voltage offset.

Data Acquisition

An Agilent 34970A data acquisition unit connected to a PC along with three 34901A 20-channel modules were used to log data throughout experiments. Data was sampled in 30 second intervals. The modules had a built-in thermocouple reference allowing direct measurement of thermocouple temperatures. Two of the three modules had thermocouples wired into the channels while the last module had output signals from the Eppley PIR (longwave), PSP (shortwave), and Everest IR sensor. Post-processing was performed to convert the PIR's voltage and resistance outputs

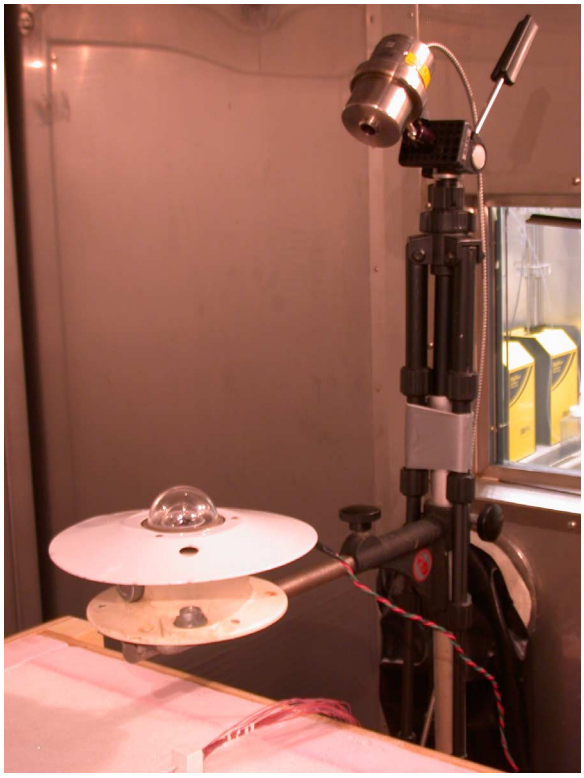

Figure 25. *Infrared sensor setup overlooking snow surface. The shortwave sensor and the top of the thermocouple array are visible.*

into an incoming longwave flux, $Q_{LW,IN}$. The PSP and IR sensor voltages were converted into a corresponding incoming shortwave flux and surface temperature by the Agilent system.

Experimental Protocol

Snow was collected for all experiments utilizing large insulated boxes. Collection was taken from a mountainous site 25 km away to minimize any transportation induced changes such as melting and settling. At the collection site dry snow was selected and carefully shoveled into the insulated boxes attempting to avoid unwanted

snow density increases. Snow was typically collected immediately after a new snow event to harvest lower density, clean snow. The boxes were stored in one of two freezers set at $-24\,^{\circ}\mathrm{C}$ and $-10\,^{\circ}\mathrm{C}$, depending on space availability. Snow pulled from these freezers intended for use in the environmental chamber was allowed to equilibrate to the chamber temperature prior to all but one of the experiments. As mentioned, dry snow was the first preference in snow collection, however some wet snow was taken from the field. Once in a storage freezer this wet snow quickly dried out although density was not as low as desired.

Once at chamber temperature, the snow was then placed into the experimental insulated snow box to the box-top. A piece of plywood was held in place while filling the box to create space to insert the thermocouple temperature array into the snowpack. The void behind the inserted array was then filled with snow. Placing the array into the snow required attention to avoid creating air pockets around the thermocouple sensor heads, which would introduce error in temperature measurements. Care was taken to provide a homogenous snowpack within the box by breaking up snow chunks and non-uniformities. Sieving the snow into the insulated box was utilized for a few experiments, but the resulting high density snow was not desirable. In an attempt to conserve the snow supply, remaining snow after a test was reused in some experiments by leaving the bottom $25 - 30\,cm$ of snow in the box. The removed snow, which was the most thermally affected, was replaced with fresh snow from the storage boxes thus starting a new experiment. Before adding the new snow, the older

snow was given a chance to equilibrate to chamber temperature if not already there. In this manner the snow supply was conserved allowing for experiments running into early summer when natural snow was melting.

Snow density of the homogeneous layers in the insulated snow box was measured prior to all experiments. At most, two unique layers existed in the insulated box consisting of possibly an older snow layer (described above) and a newly inserted layer. A triangle density sampler with a volume of $250\,cm^3$ was used to take all density measurements. Any unique type of snow in the insulated box was also characterized by grain size in order to provide the albedo model (CAR) with a required input and to give initial condition. Grain size was measured by taking samples of each homogeneous layer and taking digital photographs of the grains. A millimeter ruler or grid was placed near the grains in all photographs in order to measure sizes. During experiments samples of surface grains were photographed in an attempt to look at crystal growth. Several such samples were taken for a given experiment. Grains at depth were also photographed for a few experiments to observe sub-surface behavior. At each sampling time, the height of the snow relative to the snow box was recorded to see how much the snow sublimated or settled during the previous time period.

Once the snow was prepared in the box and relevant physical parameters were recorded the environmental chamber was then set to begin an experiment. The cooled ceiling, representing the longwave simulation, was set prior to snow sample preparation because of time needed for the ceiling to reach the desired setting. The

metal-halide lamp, representing the shortwave simulation, needed minimal time before reaching the desired set-point. As mentioned, fan speed was kept constant throughout all experiments and consequently room wind velocity remained constant. The room humidifier was always set to off to keep the relative humidity from increasing. While the increase of humidity could be controlled, decreasing room humidity was not possible with the current chamber configuration for reasons described. The data logging system was then set to record the thermocouple, PIR, PSP, and IR sensor readings. During one of the initial experiments the thermocouples were observed heating beyond reasonable values due to solar heating of the heads. To counter this problem snow temperature measurements were made immediately following the end of the experiment when the solar lamp was turned off. Such a measurement allowed the effect of the solar contamination to be determined since the thermocouples chosen quickly equilibrated with the snow temperature when the solar source was removed.

Computational Albedo Routine

Albedo

The CAR program was used to determine the overall snowpack reflectivity or albedo, which was necessary for the thermal model to predict temperature profiles. CAR calculated albedos for both layered and homogeneous snowpacks as described in Chapter 2. The flag *lab* was set to the laboratory setting for all of the experiments, which resulted in modification to some of the inputs as they were no longer

needed. These included disregarding the atmospheric transmittance, diffuse fraction, and atmospheric pressure. The transmittance and pressure parameters are used in the calculation of the diffuse fraction, which was set to be zero based on the assumption that the metal-halide light provided nearly all direct radiation. The *iwvl* parameter indicating the desired *VIS/NIR* breakpoint was set at $0.7\,\mu m$, the upper limit of the *VIS* spectrum. The solar zenith angle cosine had a value of one ($\theta = 0°$) as the solar lamp was positioned parallel to the outward normal of the snow surface.

For most of the experiments run in the environmental chamber the snow samples consisted of two layers, one layer termed *old* existing underneath another layer termed *new*.[2] The model treated layered snowpacks as a series of separate homogeneous snow layers. This evaluation was done in the two layer case by first considering the *old* layer. Using the substrate surface albedos (α_{VIS} and α_{NIR}), which in the experiments was the boundary condition plate, and relevant snow properties for the *old* layer, CAR was used to calculate albedo values for this situation. These albedo values were then used as the new substrate values for the *new* layer overlaying this *old* layer. Again CAR was run and finally albedos for this *new* layer were calculated as a function of the underlying layer. The output albedos values, α_{VIS} and α_{NIR}, were combined together into the overall solar or all-wave albedo, α_{SOLAR}, by multiplying the *VIS* and *NIR* albedos by the fractions of incoming shortwave radiation (surface downflux fraction parameter). This single solar albedo was then input directly to the thermal model, which enabled calculation of an overall, snowpack absorbed shortwave radiation flux.

[2]Table 3 shows density and depth values for these two *old* and *new* layers

A similar routine was followed for snowpacks consisting of many layers. An example on page 64 will show in detail how CAR was used to calculate albedo.

Extinction Coefficient

More important than knowing the total amount of absorbed radiation is knowing how this total amount is distributed into the snowpack's layers. This is a difficult task to accurately predict. A distribution attempt was made in the thermal model by deriving extinction coefficients from the CAR program. These coefficients were found in the following manner. First CAR is used compute a critical mass cross-section for a given snowpack, which is a function of the effective radius and soot contamination. The effective radius parameterizes the actual grain radius and the solar zenith angle. This critical term represents the thickness of a snow layer required to remove any influence of the substrate on the overall snow albedo. For example when a thin snow layer overlays a low albedo surface such as the case of snow on a highway, the upper surface snow albedo is influenced by the highway surface's albedo. However when the snow layer becomes thick enough, the effect of the highway surface is no longer detectable in the surface snow albedo. At this point the snow albedo has reached a maximum value that is dependent solely on the snow properties. The critical mass cross-section, $m_{xs,critical}$, which has units of kg/m^2, is attained when this maximum albedo is within 1% of the theoretical maximum albedo. The derivation of the critical mass cross-section is listed in Marshall [1989] in Appendix A.

Secondly, once $m_{xs,critical}$ was known from CAR it was utilized to find an extinction coefficient for a given snow layer. A modified form of the Bouguer-Lambert law (Equation 2.2, page 19) considered for all wavelengths given as

$$I \downarrow (z + \Delta z) = I \downarrow (z) \cdot \exp(-\kappa \Delta z) \tag{3.2}$$

may be solved for κ yielding

$$\kappa = -\frac{\ln [I \downarrow (z + \Delta z)/I \downarrow (z)]}{\Delta z} \tag{3.3}$$

As mentioned, the critical mass-cross section is determined at the point when the albedo reaches within 1% of its maximum. Following along with this 1% assumption, the ratio of the radiation fluxes in the numerator from Equation 3.3 can be expressed as

$$\frac{I \downarrow (z + \Delta z)}{I \downarrow (z)} = 1\% \tag{3.4}$$

This 1% assumption here assumes that at a critical mass cross-section an all-wave average of 1% of solar radiation flux remains. The medium thickness, Δz, now considered to be the snow thickness, was replaced by the snow depth, $d_{snow,critical}$, which along with Equation 3.4 yields

$$\kappa = \frac{-\ln(0.01)}{d_{snow,critical}} \tag{3.5}$$

The snow depth, $d_{snow,critical}$, can be solved from Equation 2.12 (page 31) as

$$d_{snow,critical} = \frac{m_{xs,critical}}{\rho_{snow}} \tag{3.6}$$

which may be used in Equation 3.5 to yield

$$\kappa = \frac{-\ln(0.01)}{m_{xs,critical}/\rho_{snow}} \tag{3.7}$$

This equation represents the final equation used to calculate the extinction coefficient for use in the thermal model solar radiation distribution. The extinction coefficient from this equation was calculated for each unique snow type in a given snowpack and was used as an input for the thermal model. This approach assumes that the extinction coefficient may thought of as a material parameter that can describe radiation attenuation for a particular layer anywhere in a snowpack.

CAR outputs two unique mass cross-section values, one for the *VIS* and one for the *NIR* wavebands. Thus the calculation of two extinction coefficients is possible. In this thesis only the *VIS* mass cross-section value was used and consequently only the *VIS* extinction coefficient is calculated. Use of both of the extinction coefficients in a two-stream or divided approach (where the *VIS* and *NIR* are handled separately) resulted in a absorption distribution that failed to accurately predict temperature profiles in the thermal model when compared to the method using only the *VIS* extinction coefficient. The two-stream method failed because CAR predicted too high a value for the *NIR* extinction coefficient that forced nearly all of the shortwave absorption to occur in the topmost snow layer. While a majority of solar radiation does in fact absorb in the top layer, there is a portion that penetrates further into the snowpack before absorbing [Brandt and Warren, 1993]. The two-stream approach

attempted here failed to account for this portion absorbing beyond the top layer and thus premature absorption of nearly all of the total solar energy resulted.

CAR Example

To show how CAR computed both the snowpack albedo and extinction coefficients consider a three layer snowpack as shown in Figure 26. Shown in the figure are three distinct layers overlying a substrate with known albedo, α_{sub}. Upon processing, CAR calculates the overall snowpack albedo, $\alpha_{overall}$, as a function of the snowpack's snow layers. When CAR is run for a given snowpack the albedo and extinction coefficients are found simultaneously for each snow layer.

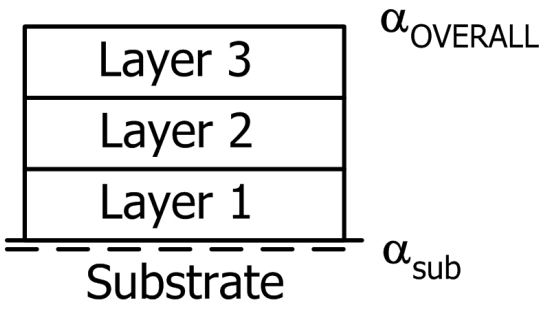

Figure 26. *Three layer snowpack with unique snow layers.*

Each layer in CAR is treated separately as shown for layer 1 in Figure 27. This layer has the following snow properties, grain radius, r_1, density, ρ_1, layer depth, d_1, and mass cross-section, $m_{xs,1}$. From these properties, CAR calculates an all-wave albedo, α_1, based on the substrate albedo, α_{sub}. To calculate α_1, CAR required

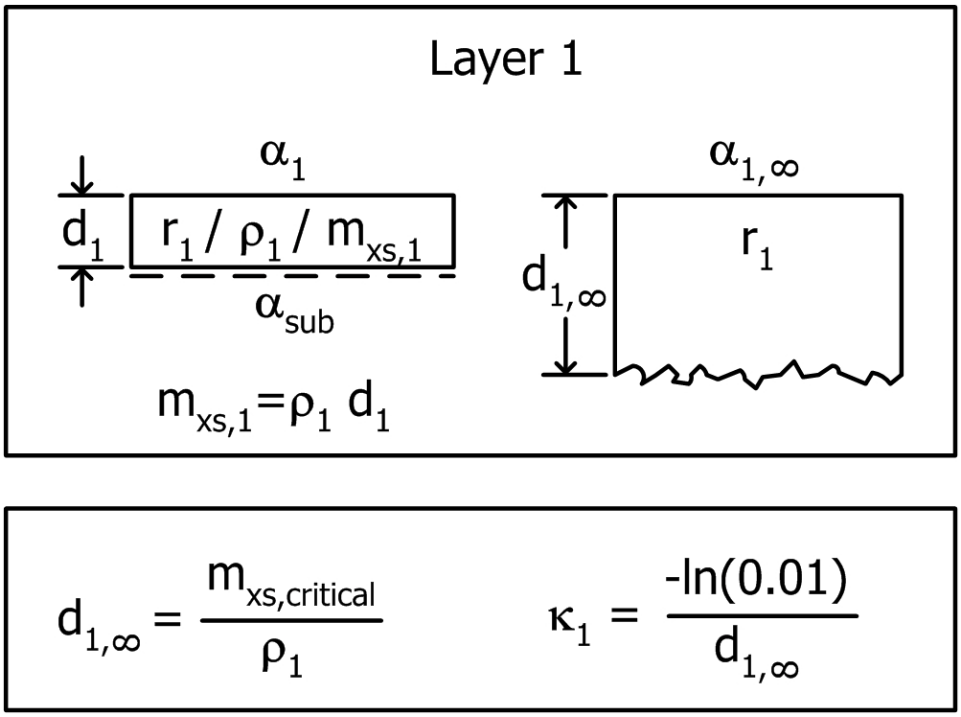

Figure 27. *Layer 1 of the three layer snowpack.*

a known value of the maximum albedo (to within 1% of the theoretical maximum albedo) denoted in Figure 27 as $\alpha_{1,\infty}$. For this maximum albedo value, a corresponding critical depth, denoted as $d_{1,\infty}$, was found from the CAR determined critical mass cross-section, $m_{xs,critical}$. This enabled the calculation of the extinction coefficient, κ_1, for layer 1.

CAR then computed an albedo and extinction coefficient for the next overlying layer in the snowpack as shown in Figure 28. Layer 2 has the shown snow properties that are used to find an albedo for this layer denoted as α_2, which was determined

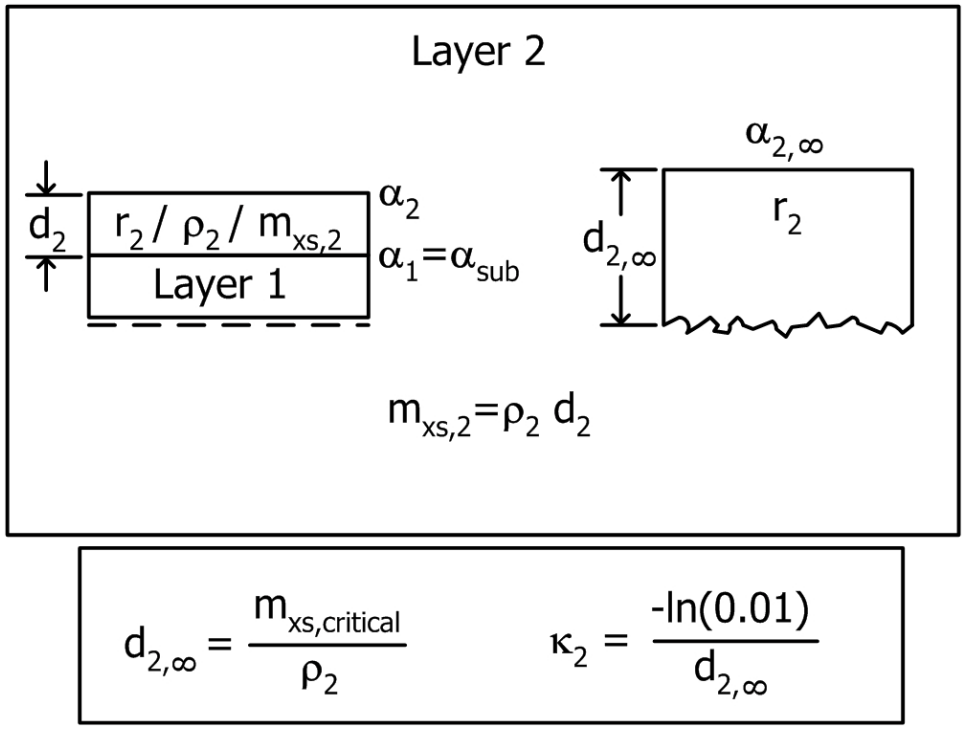

Figure 28. *Layer 2 of the three layer snowpack.*

using α_1 as the "substrate" albedo value. Again for this layer an extinction coefficient was calculated based on the CAR computed critical mass cross-section for layer 2.

The third layer follows in the same manner as the previous two layers. Again, the albedo of the third layer was computed by considering α_2 as the substrate albedo. The layer 3 albedo, α_3, is considered the overall snowpack albedo, $\alpha_{overall}$. This overall albedo was determined as a function of all of the underlying snow layers and substrate.

The resulting iterations through CAR yielded the overall snowpack albedo as well as the individual layer extinction coefficients as shown in Figure 30. These coefficients

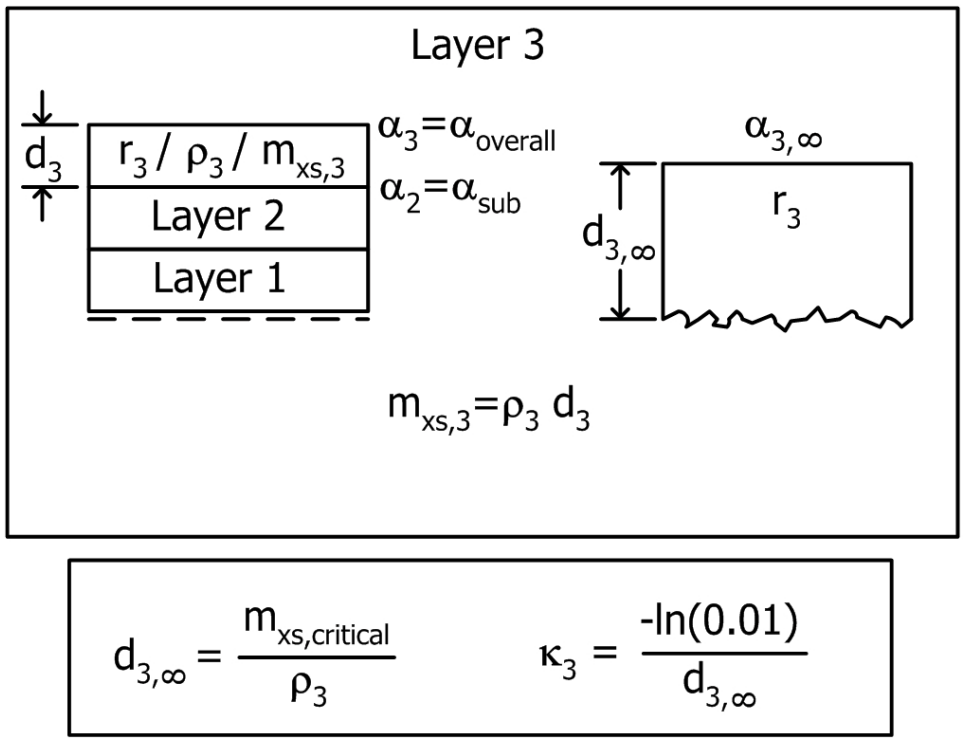

Figure 29. *Layer 3 of the three layer snowpack.*

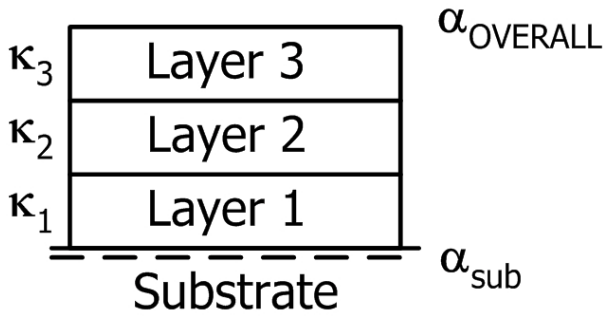

Figure 30. *Resulting CAR albedo and extinction coefficients for the three layer snowpack.*

are crucial in determining the distribution of the solar absorption throughout the snowpack.

Thermal Model

The above instrumentation served as the means to perform the experimental study. Several experiments were performed using this setup for various boundary conditions and snow densities. Two limiting factors were encountered experimentally including lack of available dry, low density snow and a limited time frame constraining the number of performed experiments. These factors, along with the primary goal of understanding the physics behind radiation-recrystallization formation, warranted development of an analytical, snow thermal model. The model, validated using experimental results, was used to test snow-types and boundary conditions not possible by using "hypothetical" experiments taking considerably less time. The model thus alleviated snow-type and time constraints by essentially serving as a means to extrapolate experimental results allowing exploration into radiation-recrystallized facet formation. Additionally, the validated model allowed single variables to be changed between hypothetical calculations allowing for isolation of the effect each variable has on facet formation. This isolation of variables is often not possible when performing experiments where several variables (e.g. grain radius, albedo, density, extinction coefficient) can change despite efforts to only modify one at a time. This approach

creates the problem of not being able to separate each variable's influence on the end result.

The thermal model used in this study originated from research done by Bristow [2002]. The main focus of this original model was prediction of temperature profiles in a natural snowpack on highways based on physical, atmospheric energy terms including radiation, convection, and conduction. This study required some modifications of the original model including changing inputs from atmospheric to environmental chamber boundary conditions and deleting unneeded sections. The model was written using Matlab, a technical computer language combining programming, computation, and visualization modules. A description of the modified thermal model including inputs, solution method, and the energy terms considered follows.

Matlab Model Overview

The snowpack in the model was simplified to a one-dimensional case neglecting any lateral energy exchanges. The model took into account various strata in the snowpack to calculate a temperature profile. Calculation of these profiles was performed numerically utilizing a Crank-Nicolson finite-difference scheme, which is described in detail on page 90. Temperature prediction was performed at discrete points throughout the snowpack based on the number of nodes specified. Figure 31 shows the 1-D geometry along with node spacing. Node spacing was set at $1\,cm$ in the model with total snowpack depths of $40\,cm$ yielding 40 layers and 41 nodes. The bottom node

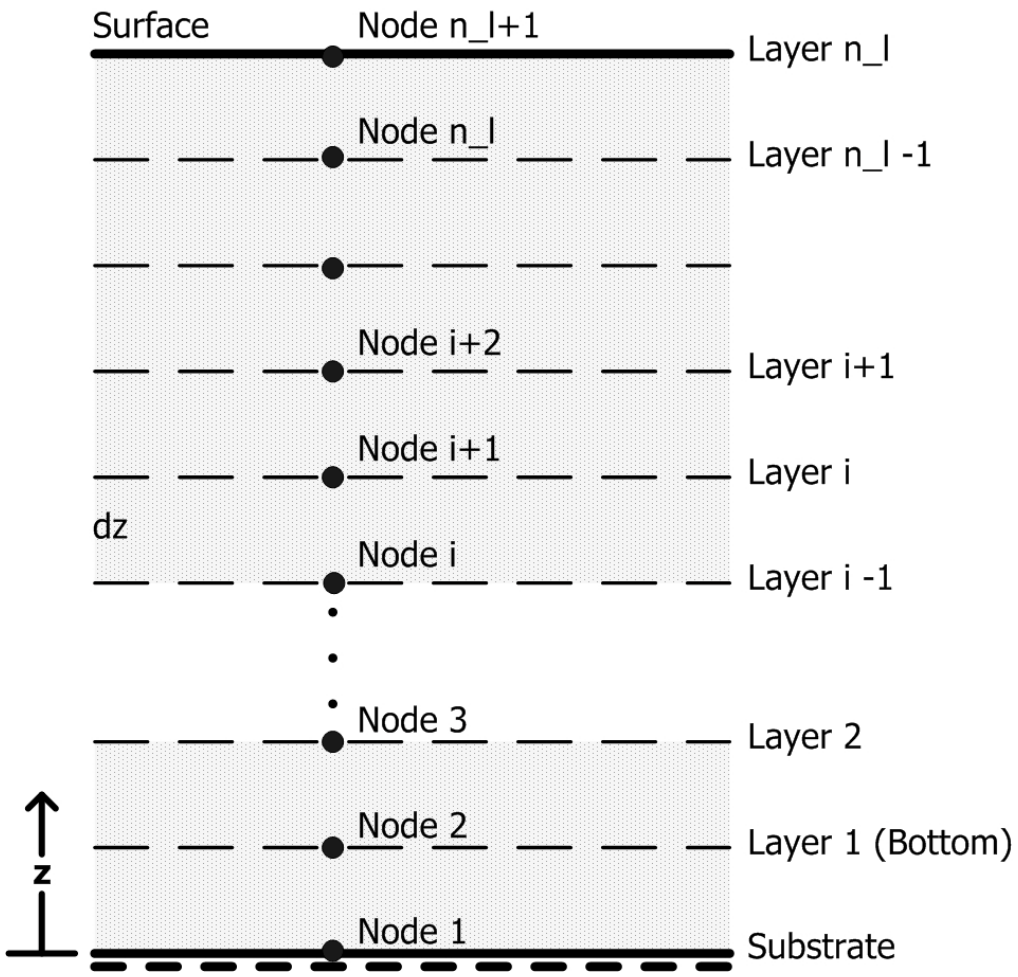

Figure 31. *Finite-difference nodal geometry.*

coincided with the boundary condition plate from the experimental setup while the top node coincided with the snow surface.

Inputs and Structure

The energy balance model utilized inputs from the CAR model, acquired meteorological-type data, snowpack parameters, and user-defined numerical parameters. Inputs were directed to the model for both experimental and hypothetical cases. CAR

model inputs included the overall snowpack albedo, α_{TOP}, which was was calculated as a function of the underlying snow layers. Additionally, extinction coefficients, κ_{layer}, were calculated based on the semi-infinite depth for each unique snow layer. For the experimental cases, meteorological-type inputs included the following chamber measurements obtained from the data acquisition system: incoming solar and longwave radiation (W/m^2), air temperature ($^\circ$C), relative humidity (%), wind speed (m/s), and barometric pressure ($mbars$). When hypothetical cases were considered during model extrapolation, user-defined data was given for these meteorological-type inputs. Snowpack parameter inputs included each layer density (ρ_{layer}), an average snowpack temperature (T_{avg}) used to find the specific heat, $C_{p,layer}$, substrate (plate) temperature (T_{plate}), and substrate reflectivity (albedo) (α_{SUB}). Inputs for numerical parameters consisted of a specified node spacing (z), total number of snow layers (n_l), and time step (Δt) corresponding to the meteorological inputs. The Matlab computer code for the thermal model is listed in Appendix A while the C++ CAR code is listed in Appendix B.

Longwave Radiation

In the longwave (LW) radiation region ($5.0 - 100\,\mu m$) only the top few millimeters of a snow surface are affected due to snow's opaque nature in these wavelengths [Brandt and Warren, 1993; Warren, 1982; Plüss, 1997], which implies that this influence is a surface phenomenon rather than a volumetric effect. Brandt and Warren [1993] state that "radiation emitted by one grain is absorbed by a neighboring grain,

so only the topmost grains can lose radiation to space." As a result, longwave exchange is only considered to affect the top node in the energy model. The surface longwave radiation exchange consists of two components: the incoming ($Q_{LW,IN}$) and outgoing ($Q_{LW,OUT}$) fluxes. The difference of these two components represents the net longwave radiation (Q_{LW}) loss from the snow surface as shown in Equation 3.8 [Plüss, 1997; Ishikawa et al., 1999; Marks, 1988].

$$Q_{LW} = Q_{LW,IN} - Q_{LW,OUT} \tag{3.8}$$

The incoming LW flux originates from the environment external to the snow sample. The LW flux depends on the absolute temperature of the chamber walls and ceiling including the glass and solar lamp. Calculating analytical radiation exchange from these objects was difficult to determine because of the effect of the solar lamp. Additionally, accurate emissivity values were not known for the various surfaces. The mentioned Precision Infrared Spectrometer (PIR; see page 45) was used to overcome these difficulties by making a direct, broad band measurement of the incoming LW irradiance ($Q_{LW,IN}$) from all of the chamber surfaces. The PIR also measured the exchange contribution from the lamp's warm filament and any heating occurring in the glass to the snow surface, which would not have been accurately calculated with an analytical approach. Incoming longwave values measured with the PIR showed differences of up to $90\,W/m^2$ between the cases where the solar lamp was turned on and off.

Emitted LW radiation from the snow surface was calculated by the Stefan-Boltzmann law with known emissivity described by,

$$Q_{LW,OUT} = \varepsilon_{snow}\,\sigma\,{T_{surface}}^4 \tag{3.9}$$

where $\sigma = 5.670 \times 10^{-8}\,W/m^2 \cdot K^4$ represents the Stefan-Boltzman constant, $T_{surface}$ is the surface (top node) snow temperature, and ε is the snow emissivity. Emissivity values range from 0.988–0.990 when grain size is above $r = 75\,\mu m$ to 0.985 when grain size is $r = 50\,\mu m$ representing fine-grained snow [Dozier and Warren, 1982; Marks, 1988]. From these emissivity values an average value of 0.988 was used in the model. Plugging Equation 3.9 into 3.8 yielded the final form used to calculate the net snow-surface, longwave radiation exchange,

$$Q_{LW} = Q_{LW,IN} - \varepsilon_{snow}\,\sigma\,{T_{surface}}^4 \tag{3.10}$$

Shortwave Radiation

The penetration of visible radiation $(0.4 - 0.75\,\mu m)$ causes an increase in snowpack temperature due to energy absorption. Amounts of absorbed energy in ice and consequently snow in the *VIS* spectrum is low, however heat can accumulate, due to the relatively low thermal conductivity of snow [Yosida, 1960]. The energy absorption assumes a "clean" snowpack, however when the pack is contaminated with highly absorptive impurities, energy absorption can increase by 50–200 times, depending on the type and quantity of impurity [Warren, 1984]. Absorption in the near-infrared (*NIR*) region occurs within the top few millimeters of the snowpack [Brandt and

Warren, 1993]. Determining the amount of solar radiation absorption due to both *VIS* and *NIR* components is crucial to predicting snow temperature profiles. As outlined, Marshall [1989] developed a computer program (SNOALB) to calculate the albedo of a homogeneous snowpack. This model was utilized by Beddoe [2001] and furthered by Bristow [2002] who applied the albedo model (changed name to CAR) to a layered, snow-covered highway. In this thesis, layers with differing density and grain radius values were used in the model.

The layering was input into the CAR model, which computed the all-wave albedo, α_{SOLAR}, that was then used by the thermal model. This albedo value represented the entire snowpack reflectivity considering all underlying layers and their properties, which was used to determine the total available absorbed solar radiation in the snowpack as

$$I_{a,TOTAL} = Q_{SW,TOTAL} = I_{atm}(1 - \alpha_{TOP}) \tag{3.11}$$

where $\alpha_{TOP} = \alpha_{SOLAR}$, $I_{a,TOTAL}$ and $Q_{SW,TOTAL}$ (W/m^2) represent the *total* available absorbed atmospheric solar energy and $I_{atm} = Q_{SW,IN}$ (W/m^2), which represents the initial incident solar radiation at the snow surface. I_{atm} is the sum of diffuse and direct beam solar radiation [Plüss, 1997]. The total absorption, $I_{a,TOTAL}$, was then distributed or broken into absorbed energy amounts at each layer, which was of use in the temperature profile determination. The following discussion explains this distribution.

Snow attenuates solar radiation through scattering and absorption. Due to this attenuation less radiation is present after passing over a given depth of snow. The difference between what initially enters the snow surface and what is present at depth is the amount that has been scattered or absorbed through the given snow. The amount of scattering and absorption is a function of snow parameters such as grain radius, density, and impurity amount. To determine present radiation at depth Bouguer's Law was utilized (Equation 2.2, page 19), which assumes snow behaves a diffusive homogeneous medium [Anderson, 1976; Male and Granger, 1981; Plüss, 1997; Jordan, 1991]. Equation 2.2 presents this law for over all wavelengths given in a slightly modified form as

$$I_{depth} = I_{initial} \cdot \exp(-\kappa \, \Delta z) \tag{3.12}$$

where I_{depth} is the energy available after an initial, incident energy quantity, $I_{initial}$, passes through a medium with thickness Δz and extinction coefficient κ. As discussed on page 61, the extinction coefficient represents a combination of the absorption and scattering coefficients and was calculated using the CAR model through Equation 3.7. Since the extinction coefficients were derived from the CAR albedo model, they represent a measure of attenuation for a given snow-type. If unique snow-types are present in a snowpack, then unique extinction coefficients exist for each layer.

In the thermal model, Equation 3.12 was used to calculate the amount of solar absorption occurring in a layer with thickness, Δz. This was done by subtracting the radiation present at depth (obtained by Equation 3.12) from the initial radiation

amount, $I_{initial}$, described for a given layer as

$$Q_{SW} = I_{absorbed} = I_{initial} - I_{depth} \tag{3.13}$$

or expressed with Equation 3.12 inserted,

$$Q_{SW} = I_{absorbed} = I_{initial} - I_{initial} \cdot \exp(\kappa \, \Delta z) \tag{3.14}$$

where Q_{SW} and $I_{absorbed}$ (W/m^2) represent the absorption flux for a given layer with an extinction coefficient, κ, and thickness, Δz. This equation was used in an algorithm within the model for each layer throughout the snowpack thus calculating absorption distribution. The following discussion describes this absorption algorithm in detail for a simplified snowpack, which is representative of the actual snowpack used in the experiments.

Figure 32 shows a three layer snowpack ($n_{layers} = 3$) with snow thicknesses (m): z_1, z_2, z_3, and extinction coefficients $(1/m)$ (determined from CAR): κ_1, κ_2, and κ_3, which are all allowed to take on distinct values. An initial, all-wave atmospheric amount of solar radiation, I_{atm}, irradiates the snow surface. A reflected value, I_r (W/m^2), is obtained based on the albedo value computed from CAR labeled as α_3, which is equivalent to the variable α_{TOP} or α_{SOLAR} discussed on page 74.[3] Recall that α_{TOP} is an all-wave albedo calculated as function of the underlying layers and snow-types. The reflected term, I_r, is not merely a planar, surface reflection, but is rather the sum of this planar surface reflection and volumetric reflections emanating

[3]This reflection, I_r, is identical to a value obtained if a spectrometer were measuring reflectivity of the snow surface.

from everywhere within the snowpack. The amount that is not reflected represents the amount of energy that is absorbed (W/m^2) through the entire snowpack labeled as $I_{a,TOTAL}$ and calculated by Equation 3.11. This total amount is then distributed throughout the snowpack layers depending on the optical properties of each layer. Once distributed, the sum of these distributed layer absorptions must sum to $I_{a,TOTAL}$.

Distribution of $I_{a,TOTAL}$ starts by using Bouguer's Law (Equation 3.12) written for layer 3 as

$$I_2 = I_{a,TOTAL} \cdot \exp(-\kappa_3 \, z_3) \tag{3.15}$$

I_2 represents the radiation quantity at depth after light passes through thickness z_3 and $I_{a,TOTAL}$ represents the initial radiation quantity available to absorb into the layer. Equations 3.13 or 3.14 are then used to find the absorption, $I_{a,3}$ or $Q_{SW,3}$ (W/m^2), as shown. The algorithm then moves to layer 2 with I_2 now representing both the initial radiation available to absorb as well as the remaining portion of the total available to absorb, $I_{a,TOTAL}$. At this point the above equations are repeated to find layer absorptions for layers 1 & 2. At the substrate (bottom boundary condition plate) level the material of interest is non-transparent thus voiding Bouguer's law. Calculation of the absorbed radiation at the substrate is determined by the irradiance, I_0, multiplied by the absorptivity $(1 - \alpha_{sub})$. For snowpacks containing a larger number of layers, an identical approach was used to partition the total absorbed solar radiation, $I_{a,TOTAL}$. Jordan [1991] used a similar method to determine absorption for

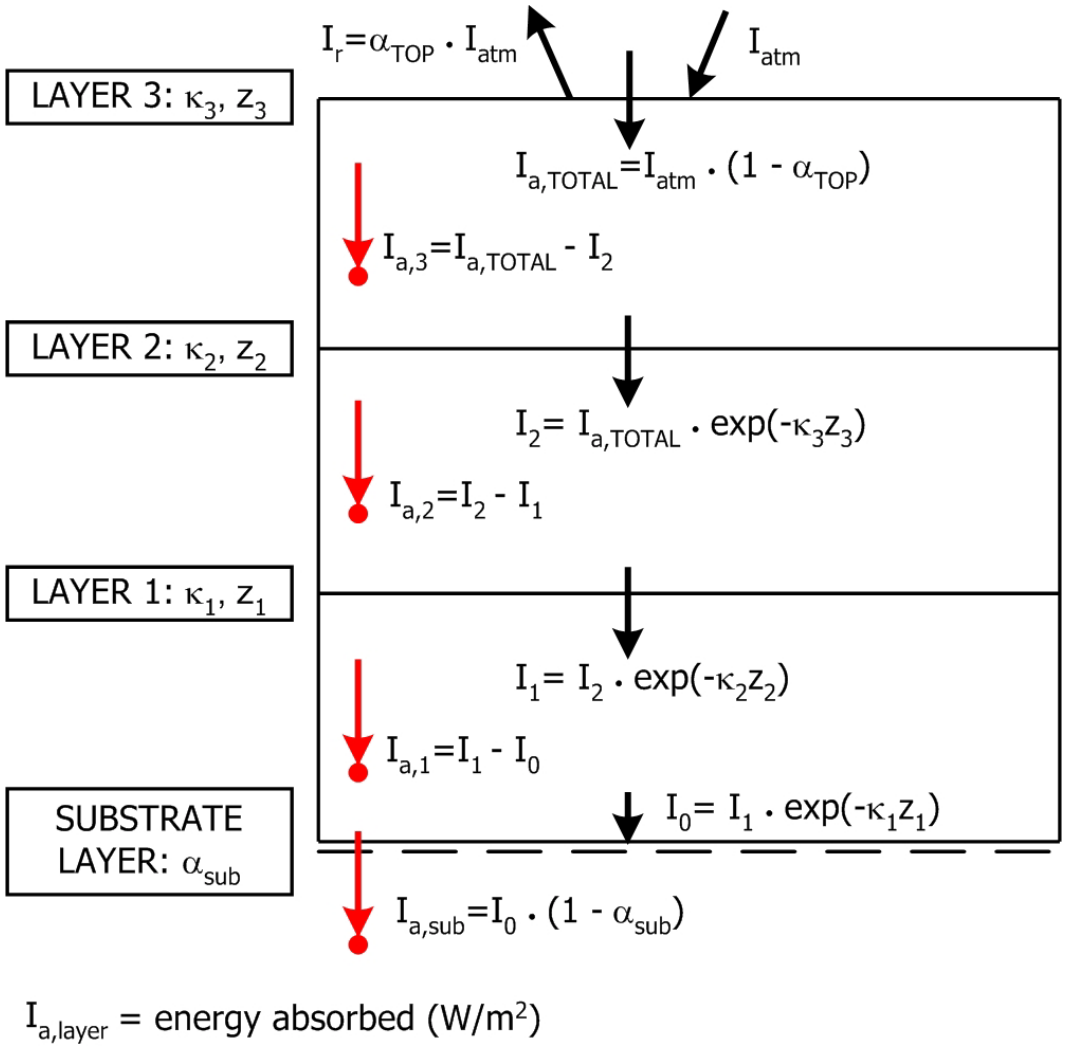

Figure 32. *Three layer example illustrating the solar radiation absorption scheme used in the thermal model.*

the SNTHRM temperature model though she obtained κ and α in a different fashion than outlined in this thesis.

Turbulent Exchange

Energy exchange due to latent heat flux, Q_E (W/m^2), and sensible (convective) heat flux, Q_H (W/m^2), comprise the fluxes of turbulent exchange. These fluxes act upon the surface of a snowpack and are thus treated to only influence the top node in the thermal model similar to the longwave radiation exchange. These fluxes are secondary to the radiation exchange in importance as far as the influence they have on energy exchange [Marks, 1988]. They generally provide surface cooling to the snowpack during mid-winter conditions [Plüss, 1997].

Sensible Heat. The sensible heat flux accounts for non-phase change heat transfer between the snow surface and the air and is driven by a temperature difference between the two as [Ishikawa et al., 1999; Martin and Lejeune, 1998; Marks, 1988],

$$Q_H = \rho_{air}\, C_p\, K_h\, V_w\, (T_{air} - T_{surface}) \tag{3.16}$$

where

$$\begin{aligned} \rho_{air}, C_p &= \text{density } (kg/m^3) \text{ and specific heat capacity of air } (J/kg \cdot K) \\ K_h &= \text{dimensionless turbulent transfer coefficient} \\ V_w &= \text{wind speed } (m/s) \\ T_{air}, T_{surface} &= \text{air and surface temperature } (K) \end{aligned}$$

The air density, ρ_{air}, is obtained from the ideal gas law as

$$\rho_{air} = \frac{P_{atm}}{R_{air} \cdot T_{air}} \tag{3.17}$$

where P_{atm} is the atmospheric air pressure (kPa), and R_{air} is the air gas constant ($0.287\,kJ/kg \cdot K$).

Latent Heat. The latent heat flux is driven by vapor pressure gradients between the air and snow surface, which causes phase change at the snow surface and is given as [Ishikawa et al., 1999; Martin and Lejeune, 1998],

$$Q_E = 1000 \frac{M_v}{M_a} \rho_{air} L_s K_e V_w (e_{air} - e_{surface}) {P_{atm}}^{-1} \tag{3.18}$$

where

L_s	=	latent heat of sublimation phase change ($2833\,kJ/kg$)
K_e	=	dimensionless turbulent transfer coefficient for water vapor
e_{air}, $e_{surface}$	=	air and surface water vapor pressures (kPa)
M_v/M_a	=	ratio of dry-air and water-vapor molecular weights (0.622)
P_{atm}	=	atmospheric air pressure (kPa)

The addition of the $1000\,J/kJ$ factor was included to change units to be consistent with the other flux terms used in the thermal model (W/m^2). Under neutral atmospheric conditions K_e and K_h from Equations 3.16 and 3.18, respectively, are considered to be equal [Ishikawa et al., 1999; Stull, 1988; Brun et al., 1989]. For the thermal model a value of 2.3×10^{-3} was used for these transfer coefficients. Neutral atmospheric conditions refer to the stability of the atmosphere. Stability is achieved even during strong winds events [Beddoe, 2001]. The $1.7\,m/s$ wind velocity existing in the environmental chamber can be readily considered as a stable, neutral condition.

Depending on the vapor pressure differences between the air and snow, heat can be added or taken from the snow surface. When air vapor pressure is less than snow

vapor pressure over the snow surface, energy is removed from the snowpack from the sublimation process, which requires energy to initiate. The opposite case occurs when the snow surface has a higher vapor pressure than the air. In this case, vapor in the air is reduced in energy as it condenses and freezes to the snow surface, which causes snowpack heating. Phase change can be due to evaporation or sublimation, however in all experiments the snow surface stayed cool enough that phase change due to sublimation was the only change considered.

Vapor Pressure. To calculate the vapor pressures, e_{air} and $e_{surface}$, from Equation 3.18, the Clausius-Clapeyron equation was used, which gives the relationship between the temperature of water and its vapor pressure. It is described by a differential equation as

$$\frac{de_s}{dT} = \frac{L}{T\, v_{fg}} \tag{3.19}$$

where e_s is the vapor saturation pressure (kPa), T is temperature (K), L is the latent heat of phase change (kJ/kg), and v_{fg} is the specific volume (m^3/kg) difference between the two phases: f, saturated liquid, and g, saturated vapor ($v_{fg} = v_g - v_f$). The latent heat of phase change refers to the amount of heat lost or gained when water undergoes phase change. Four latent heat terms are possible depending on the phase constituents, including the latent heats of condensation, fusion, sublimation, and vaporization. For the experiments in the environmental chamber where low relative humidity and freezing temperatures prevailed, the latent heat of sublimation, L_s, was

used, which described the amount of heat lost or gained when ice (snow) changes phase to vapor or vice versa. L_s was assumed to be constant over the temperature range of interest, as L_s changes little for low pressures. Equation 3.19 can be simplified by finding an expression for the water specific volume difference, v_{fg}. The ideal gas equation approximates the saturated specific volume of water vapor as

$$v_g = \frac{R_v \cdot T}{e_s} \tag{3.20}$$

where R_v is the gas constant for water vapor ($0.462\,kJ/kg\cdot K$) and e_s is the saturation water vapor pressure (kPa). The specific volume of saturated liquid, v_f, can be assumed to be zero when compared to the specific volume of saturated vapor, $v_g \gg v_f \;\Rightarrow\; v_f \approx 0$. Using this assumption and Equation 3.20, Equation 3.19 becomes

$$\frac{de_s}{dT} = \frac{L_s\, e_s}{R_v\, T^2} \tag{3.21}$$

where the latent heat of phase change was replaced with the latent heat of sublimation. This equation can be solved for an unknown pressure, e_i, at temperature T_i by separation of variables and integration as

$$\int_{e_o}^{e_i} \frac{de_s}{e_s} = \frac{L_s}{R_v} \int_{T_o}^{T_i} \frac{dT}{T^2} \tag{3.22}$$

$$\ln\left(\frac{e_i}{e_o}\right) = \frac{L_s}{R_v}\left(\frac{1}{T_o} - \frac{1}{T_i}\right) \tag{3.23}$$

$$e_i = e_o \cdot \exp\left[\frac{L_s}{R_v}\left(\frac{1}{T_o} - \frac{1}{T_i}\right)\right] \tag{3.24}$$

where

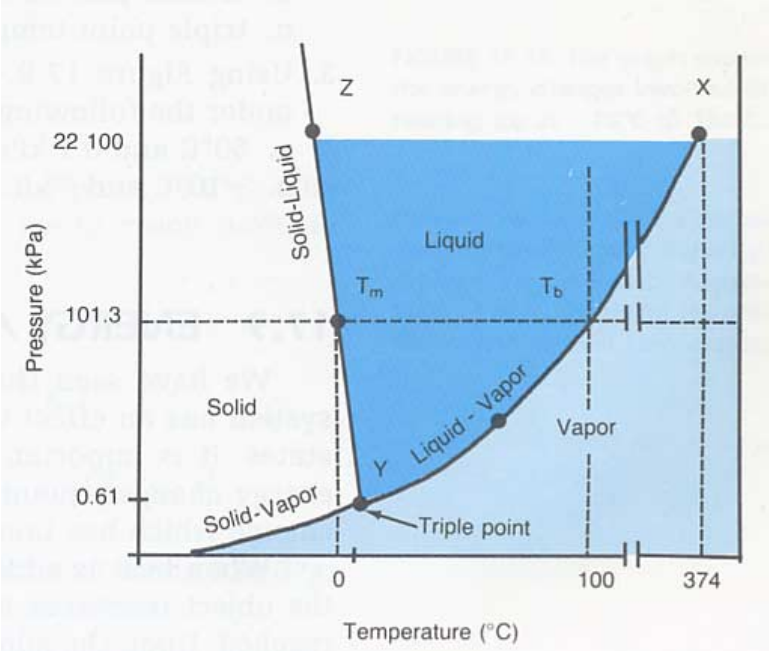

Figure 33. *Water phase diagram.*

L_s = latent heat of sublimation phase change ($2833\,kJ/kg$)
R_v = gas constant for water vapor ($0.462\,kJ/kg \cdot K$)
T_o, e_o = reference temperature (K) and pressure (kPa)
e_i = saturation vapor pressure of interest (kPa)
T_i = temperature of interest (K)

Equation 3.24 was the final form of the Clausius-Clapeyron equation used to solve for an unknown vapor pressure, e_i, in the thermal model. Known data points for saturation vapor pressure at a given temperature are needed in this equation in order to solve for e_i. These reference points exist on the solid-vapor saturation line in a water phase diagram as shown in Figure 33. Accuracy is increased in Equation 3.24 when small temperature differences are used between T_i and T_o. The reference temperature used was $T_o = -5\,°\text{C}$ corresponding to a saturation vapor pressure $e_o = 0.402\,kPa$.

Before Equation 3.24 was usable in the thermal model the water vapor partial pressure in the air and at the snow surface was required. This pressure was determined from the definition of relative humidity, ϕ, defining the ratio of water vapor pressure, e_v (kPa), to the water saturation vapor pressure, $e_g(kPa)$ as

$$\phi = \frac{e_v}{e_g} \tag{3.25}$$

At the snow surface, the water vapor pressure, e_v, was assumed to be saturated implying that $\phi = 1$ [Adams and McDowell, 1991] and

$$e_v = e_g \tag{3.26}$$

This result allowed the direct calculation of the snow surface water vapor pressure, $e_{surface}$, from the Clausius-Clapeyron equation (3.24). In the air, the relative humidity value was known as a measured quantity in the environmental chamber. Therefore the air saturation vapor pressure, e_{air}, was calculated by taking the result from Equation 3.24 and multiplying it by the relative humidity,

$$e_v = \phi \cdot e_g \tag{3.27}$$

Energy Balance Equation

The preceding flux terms (longwave, shortwave, and turbulent exchange) all influence the snow temperature profile. Derivation of a differential equation describing snow temperature will show their contributions. To begin, the First Law of Thermodynamics provides an expression describing the conservation of energy within a

system interacting with its surroundings [Moran and Shapiro, 2004; Incropera and Dewitt, 1996] given in the rate form as

$$\frac{dE}{dt} = q - \dot{W} \tag{3.28}$$

where q ($Watts$) is the rate of net heat transfer into the system at time t, $\dot{W}$ ($Watts$) is the rate of net mechanical (work) energy transferred out of the system at time t, and dE/dt is the time rate of energy change within the system at time t. A system is defined as a control volume for a fixed amount of mass implying that mass neither is gained or lost. The control volume is a region in space defined by a bounding control surface through which energy or matter might pass. An assumption was made that a control volume bounding a portion of the snowpack was in fact a system with no mass flux. In the snowpack the control volume was defined as the thickness of a layer.

The energy rate term in Equation 3.28 can be expanded to include the following

$$\frac{dE}{dt} = \frac{dKE}{dt} + \frac{dPE}{dt} + \frac{dU}{dt} = q - \dot{W} \tag{3.29}$$

which includes the rates of change of kinetic (KE), gravitational potential (PE), and internal (U) energy [Moran and Shapiro, 2004]. Assumptions were made that kinetic, potential, and mechanical ($\dot{W}$) energy changes were negligible leading to the following expression,

$$\frac{dU}{dt} = q \tag{3.30}$$

which relates the internal energy of the system to the rate of heat transfer to the system. Internal energy is considered a volumetric phenomenon that occurs over the volume of the system and is an extensive property meaning that the energy is proportional to the volume magnitude. This internal energy term was considered to include only the effects of sensible or thermal components. Internal energy can also consist of latent (phase change), chemical, and nuclear components. The net heat transfer rate, q, can be broken into two components as

$$q = q_c + q_g \tag{3.31}$$

describing contributions from conduction, q_c $(Watts)$, and energy supply, q_g $(Watts)$. q_g in the model contains heat sources or sinks whose energy converts to thermal energy within the control volume. Shortwave radiation absorption and the turbulent and longwave exchanges were included in this term. The turbulent and longwave exchanges actually occur at the surface as opposed to over the volume, however for numerical solution of the top node they were considered as heat sources [Bristow, 2002]. The shortwave absorption, while given as a flux (W/m^2), is absorbed over a volume. The final form of the energy conservation equation stated here before further manipulation is given as

$$\frac{dU}{d\,t} = q_c + q_g \tag{3.32}$$

It should be noted that for steady-state conditions where the energy gained is equal to the energy lost in the control volume the sum of q_c and q_g equals zero. Derived

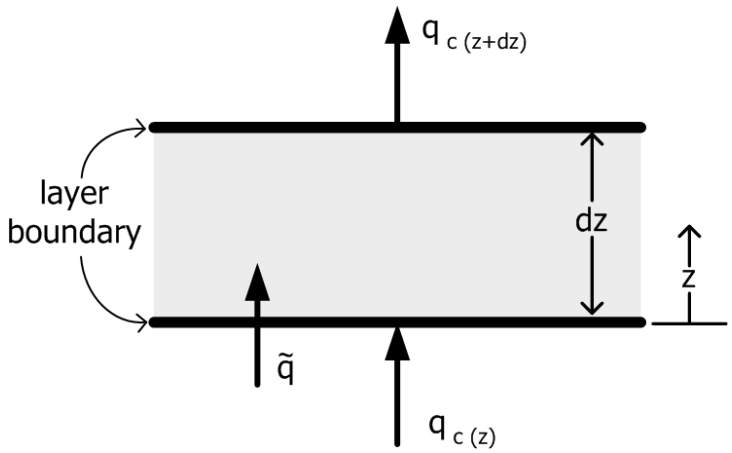

Figure 34. *One-dimensional differential control volume used in derivation of Fourier-Biot heat diffusion equation.*

expressions for the components of Equation 3.32 follow with the goal of deriving a differential equation[4] describing the temperature profile of the snowpack for prescribed boundary conditions. Figure 34 shows a typical control volume and is used as an aid in the component derivation.

The control volume in Figure 34 has a thickness in the z direction of dz and is assumed for the time being to be infinitesimal. Since only conduction in the vertical direction is assumed, components in the x, y directions are neglected. Entering the control volume perpendicular to the volume surface is the conduction component $q_{c(z)}$ $(Watts)$. Leaving the control volume is the component $q_{c(z+dz)}$ $(Watts)$, which can be expressed as a truncated Taylor series (neglecting higher order terms),

$$q_{c(z+dz)} = q_{c(z)} + \frac{\partial q_{c(z)}}{\partial z} dz \tag{3.33}$$

[4]This equation is known as the Fourier-Biot Heat Diffusion Equation [Kakaç and Yener, 1993]

This equation states that the "z component of the heat transfer rate at $z + dz$ is equal to the value of this component at z plus the amount by which it changes with respect to z times dz" [Incropera and Dewitt, 1996]. To relate the two conduction fluxes from Figure 34 to the final form of the energy conservation equation (3.32) the net conduction heat transfer rate is needed, which is simply the difference between these fluxes. Since $q_{c(z)}$ is entering the control volume it is considered positive, which was the sign convention used throughout the thermal model. The sum of the net conduction heat transfer rate is given as

$$q_c = q_{c(z)} - q_{c(z+dz)} \tag{3.34}$$

The q_g $(Watts)$ energy supply term containing solar radiation and longwave and turbulent fluxes are considered as heat source terms, q''_g (W/m^2), per unit area given as

$$q_g = q''_g \cdot dx\, dy \tag{3.35}$$

and summed as

$$q''_g = Q_{LW} + Q_{SW} + Q_H + Q_E \tag{3.36}$$

The change of internal energy may further be expressed for the entire control volume [Incropera and Dewitt, 1996] as

$$\frac{dU}{d\,t} = \rho C_p \frac{\partial T}{\partial t} \cdot dx\, dy\, dz \tag{3.37}$$

where ρ and C_p represent the density (kg/m^3) and specific heat capacity ($J/kg \cdot K$). Combining Equations 3.34, 3.35, and 3.37 into the final energy conservation equation (3.32) yields

$$\rho C_p \frac{\partial T}{\partial t} \cdot dx\, dy\, dz = q_{c(z)} - q_{c(z+dz)} + q''_g \cdot dx\, dy \tag{3.38}$$

Substituting Equation 3.33 yields

$$\rho C_p \frac{\partial T}{\partial t} \cdot dx\, dy\, dz = -\frac{\partial q_{c(z)}}{\partial z} dz + q''_g \cdot dx\, dy \tag{3.39}$$

Fourier's law of conduction [Incropera and Dewitt, 1996] in the z direction is given as

$$q_{c(z)} = -k \frac{\partial T}{\partial z} \cdot \, dx\, dy \tag{3.40}$$

Inserting this equation into Equation 3.39 and dividing out the dimensions of the control volume (dx, dy, dz) yields the final differential equation describing temperature as a function of time and z-direction with energy supply,

$$\rho C_p \frac{\partial T}{\partial t} = k \frac{\partial^2 T}{\partial z^2} + \tilde{q} \tag{3.41}$$

where the thermal conductivity, k ($W/m \cdot K$), is assumed constant and the energy supply term, $\tilde{q}$ (W/m^3), is presented as

$$\tilde{q} = \frac{q''_g}{dz} \tag{3.42}$$

Equation 3.41 is classified as a parabolic type of partial differential equation (PDE) that is a function of time and space variables (i.e. $T = T(x,t)$). Discussion on the solution method follows.

As for any differential equation, boundary and initial conditions are needed in the solution process. For the experimental procedure described, the measured snow temperature profile at the beginning of an experiment was used as the initial condition. A Dirichlet (specified temperature) boundary condition was specified for the bottom of the snowpack and given the value of the plate temperature. The top boundary condition consisted of a snow surface exposed to both radiation (longwave and shortwave exchange) and convection (turbulent exchange). This top condition poses a difficult problem to solve analytically because radiation exchange is non-linear in temperature thus hampering efforts to solve the differential equation. As a consequence, numerical methods were utilized because of their ability to handle such non-linearities.

Numerical Solution

Solution of the PDE in Equation 3.41 was solved using the Crank-Nicolson finite-difference method, which provides second-order accuracy in both time and space [Chapra and Canale, 1998; Özisik, 1994; Patankar, 1980]. The method can be developed to provide good approximations of temperature for each node in the snowpack as shown in Figure 31 describing the finite-difference grid. This solution was done by essentially discretizing the PDE (Equation 3.41) by providing discrete approximations for the derivatives. Equation 3.41 has a first-order temporal (time) partial derivative

on the left-hand side of the equation and a second-order spatial partial derivative on the right-hand side. The temporal derivative can be discretized with the following central-difference representation,

$$\rho C_p \frac{\partial T}{\partial t} \cong \rho_i C_{p_i} \frac{T_i^{j+1} - T_i^j}{\Delta t} \tag{3.43}$$

where the terms T_i^{j+1} and T_i^j represent temperatures at the node of interest, i, for both the current, j, and future, $j+1$, times. The future time designation refers to those temperatures which are not currently known and need to be solved for while the current temperatures are known values. Notice the density and specific heat variables are given a subscript i indicating that they are now defined on a nodal basis. The specific heat was calculated using Equation 2.8 (page 24) for the entire snowpack based on the average pack temperature. The spatial derivative is approximated by an arithmetic average of a central difference expression as

$$k \frac{\partial^2 T}{\partial z^2} \cong k_{\mathit{eff},i} \cdot \frac{1}{2} \left[\frac{T_{i+1}^j - 2T_i^j + T_{i-1}^j}{(\Delta z)^2} + \frac{T_{i+1}^{j+1} - 2T_i^{j+1} + T_{i-1}^{j+1}}{(\Delta z)^2} \right] \tag{3.44}$$

where the subscripts $i-1$ and $i+1$ represent the two nodes surrounding the node of interest with subscript i. The effective thermal conductivity replaces the constant value specified previously. This effective value was calculated using Equation 2.6 (page 24) for each layer with density ρ_i used above. Equations3.43 and3.44 can be visualized with Figure 35, which shows how the four nodal temperatures are used to find an average as shown by the dashed circle, which is found for the averaged time indicated by $t^{j+1/2}$. Inserting Equations 3.43 and 3.44 into Equation (3.41 yields,

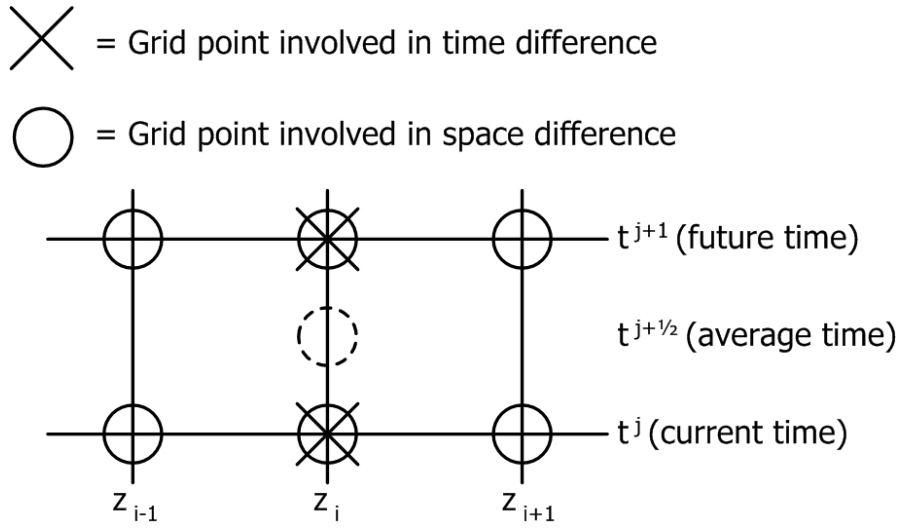

Figure 35. *Computational schematic for the Crank-Nicolson method where the circles represent the temperature values at each location and time [Chapra and Canale, 1998].*

$$\rho_i C_{p_i} \frac{T_i^{j+1} - T_i^j}{\Delta t} = k_{\mathit{eff},i} \cdot \frac{1}{2} \left[\frac{T_{i+1}^j - 2T_i^j + T_{i-1}^j}{(\Delta z)^2} + \frac{T_{i+1}^{j+1} - 2T_i^{j+1} + T_{i-1}^{j+1}}{(\Delta z)^2} \right] + \tilde{q}_i \quad (3.45)$$

where $\tilde{q}_i$ represents the energy generation assigned to each node. This equation is the Crank-Nicolson finite-difference approximation of the energy balance equation (3.41) applied to each snowpack node. The next task involved separating the current and future temperatures, T^j and T^{j+1}, to opposite sides of the equation yielding the following equation,

$$\begin{aligned} \left[\frac{-k_{\mathit{eff},i}}{2(\Delta z)^2} \right] T_{i-1}^{j+1} + \left[\frac{\rho_i C_{p_i}}{\Delta t} + \frac{k_{\mathit{eff},i}}{(\Delta z)^2} \right] T_i^{j+1} + \left[\frac{-k_{\mathit{eff},i}}{2(\Delta z)^2} \right] T_{i+1}^{j+1} = \ldots \\ \left[\frac{k_{\mathit{eff},i}}{2(\Delta z)^2} \right] T_{i-1}^{j} + \left[\frac{\rho_i C_{p_i}}{\Delta t} - \frac{k_{\mathit{eff},i}}{(\Delta z)^2} \right] T_i^{j} + \left[\frac{k_{\mathit{eff},i}}{2(\Delta z)^2} \right] T_{i+1}^{j} + \tilde{q}_i \end{aligned} \quad (3.46)$$

If the terms in square brackets are written as constants, then

$$-[a_i]\,T_{i-1}^{j+1} + [b1_i]\,T_i^{j+1} - [a_i]\,T_{i+1}^{j+1} = [a_i]\,T_{i-1}^{j} + [b2_i]\,T_i^{j} + [a_i]\,T_{i+1}^{j} + c_i \qquad (3.47)$$

The c_i term represents the heat source terms, including the radiation and turbulent fluxes. For the top layer, all of these heat source terms are included as

$$c_n = \tilde{q}_n = \frac{q''_{g,n}}{\Delta z}$$

which comes from Equation 3.42 where Δz replaces dz in this finite-difference approximation. The sum of the heat sources evaluated at the surface is

$$q''_{g,n} = (Q_{LW} + Q_{SW} + Q_H + Q_E)|_n \qquad (3.48)$$

For the interior layers, only a heat source contribution due to absorbed solar radiation is included as

$$c_i = \tilde{q}_i = \frac{q''_{g,i}}{\Delta z} = \frac{Q_{SW,i}}{\Delta z} \qquad \text{for } i = 1,\, 2,\, \ldots\,,\, n-1 \qquad (3.49)$$

where $Q_{SW,i}$ (W/m^2) is the absorption occurring at layer i.

This Crank-Nicolson method is classified as an implicit scheme meaning that new temperatures are solved using old, known temperature values, T^j, as well as future, unknown temperatures, T^{j+1}. In Equation 3.47 the left-hand side represents unknown, new temperature values while the right-hand side represents a series of "constants" consisting of known coefficients and the current temperatures. The above equation was written for each interior snowpack node. For the top and bottom nodes in the

snowpack boundary conditions were applied, which resulted in a slightly different equation. For the bottom boundary condition where a constant temperature was specified the nodal equation was simply

$$T_1^j = T_1^{j+1} = T_{plate} \tag{3.50}$$

The top boundary condition involved radiation and turbulent exchange, which were treated together as a prescribed heat flux boundary condition (Neumann condition) as

$$k_{\mathit{eff},n} \frac{\partial T}{\partial z} = q''_{g,n} \tag{3.51}$$

where the flux $q''_{g,n}$ represents the heat sources (Equation 3.36) for the top layer, n, (turbulent and radiation flux terms) and $k_{\mathit{eff},n}$ is the effective thermal conductivity of the top layer. This boundary condition can be discretized using a second-order accurate central-difference formula about the node n for both the current and new times respectively as

$$k_{\mathit{eff},n} \frac{T_{n+1}^j - T_{n-1}^j}{2\Delta z} = {q''_{g,n}}^j \tag{3.52}$$

$$k_{\mathit{eff},n} \frac{T_{n+1}^{j+1} - T_{n-1}^{j+1}}{2\Delta z} = {q''_{g,n}}^{j+1} \tag{3.53}$$

Notice that the terms T_{n+1}^j and T_{n+1}^{j+1} are actually temperatures outside of the snowpack at fictitious nodes [Özisik, 1994]. To eliminate these fictitious temperatures they

are first isolated from Equations 3.52 and 3.53 as

$$T_{n+1}^{j} = {q''_{g,n}}^{j} \cdot \frac{2\Delta z}{k_{eff,n}} + T_{n-1}^{j} \tag{3.54}$$

$$T_{n+1}^{j+1} = {q''_{g,n}}^{j+1} \cdot \frac{2\Delta z}{k_{eff,n}} + T_{n-1}^{j+1} \tag{3.55}$$

and then inserted into Equation 3.47 using the assumption that the ${q''_{g,n}}^{j+1} = {q''_{g,n}}^{j}$. This assumption means that the current, known heat source value (at time j) for the top layer is used to predict the future, unknown temperatures (at time $j+1$). Taking into account the boundary conditions, the top node equation is given as

$$-2(a_n)\, T_{n-1}^{j+1} + (b1_n)\, T_n^{j+1} = 2(a_n)\, T_{n-1}^{j} + (b2_n)\, T_n^{j} + 3\, c_n \tag{3.56}$$

To summarize, Equations 3.50 and 3.56 together with Equation 3.47 written for nodes $i = 2, 3, \ldots n-1$ provides a complete set of $n+1$ algebraic equations in $n+1$ unknown node temperatures. This set of equations provides the complete Crank-Nicolson finite-difference approximation for the snowpack with the specified boundary conditions.

Solution of the complete equation set is aided by placing all of the equations in matrix form shown as

$$\begin{bmatrix} 1 & 0 & 0 & 0 & \dots & 0 \\ -a_2 & b1_2 & -a_2 & 0 & \dots & 0 \\ 0 & -a_3 & b1_3 & -a_3 & \dots & 0 \\ \dots & & & & & \\ 0 & & \dots & -a_{n-1} & b1_{n-1} & -a_{n-1} \\ 0 & & \dots & 0 & -2a_n & b1_n \end{bmatrix} \cdot \begin{pmatrix} T_1^{j+1} \\ T_2^{j+1} \\ T_3^{j+1} \\ \dots \\ T_{n-1}^{j+1} \\ T_n^{j+1} \end{pmatrix} = \dots$$

$$\begin{bmatrix} T_{plate} \\ (a_2)\,T_1^j + (b2_2)\,T_2^j + (a_2)\,T_3^j + c_2 \\ (a_3)\,T_2^j + (b2_3)\,T_3^j + (a_3)\,T_4^j + c_3 \\ \dots \\ (a_{n-1})\,T_{n-2}^j + (b2_{n-1})\,T_{n-1}^j + (a_{n-1})\,T_n^j + c_{n-1} \\ 2(a_n)\,T_{n-1}^j + (b2_n)\,T_n^j + 3\,c_n \end{bmatrix} \tag{3.57}$$

This set of equations can be simply stated as

$$[A](T^{j+1}) = (B) \tag{3.58}$$

where column matrix (B) contains the current (known) temperatures, T^j, which are considered constants. Equation 3.58 was solved for the new (unknown) temperature column matrix, (T^{j+1}), by inverting matrix $[A]$ so that

$$(T^{j+1}) = [A]^{-1}(B) \tag{3.59}$$

This solution technique is known as a matrix inversion solution method for solving systems of equations. While more efficient and less computationally costly methods exist to solve a set of simultaneous equations (eg: Thomas Algorithm) the matrix inverse method worked fast enough for this problem to warrant its use.[5] The Crank-Nicolson method is considered an implicit method as a simultaneous solution of all

[5]Total run time of the thermal model averaged from 5-10 seconds.

equations is required to solve for the new temperatures. Conversely, an explicit method solves for new temperatures with the same current and future temperatures as the implicit method, but each equation can be solved explicitly without having to solve a set of simultaneous equations. This independence is a result of the ability of the new (unknown) temperature, T_{node}^{j+1}, to be isolated and defined *explicitly* as the method's name implies [Chapra and Canale, 1998; Özisik, 1994].

A benefit of the Crank-Nicolson method is that there is no restriction on the on the time step size, Δt. In other words this method has unconditional stability, which means that errors at any stage of the computation are not amplified but are attenuated as the computation progresses. Having no restrictions on the time step does not mean that any arbitrary value can be used to achieve accurate results. Rather, accurate results are obtained when the time step is chosen to be small enabling convergence, which means that as Δt approaches zero, the results of the finite-difference method approach the true solution.

CHAPTER 4

RESULTS AND DISCUSSION

Overview

Within this section results from the validation of the CAR program with the hyperspectral imaging system are presented, followed by the experimental results shown along with the thermal model calculations. The experiments were chosen in an attempt to form near-surface facets via radiation recrystallization. For each experiment a thermal model calculation was performed for validation purposes and to gain an understanding of the physics behind the formation of these facets. After confidence in the model is established through validation, it can then be further applied to conditions not actually tested in the environmental chamber. In this regard the model serves as a extrapolation tool for these "hypothetical" cases, which are presented last in this section.

CAR Validation

Accuracy of the Computational Albedo Routine (CAR) was studied by Beddoe [2001] where he reported an overall standard deviation of 0.11 when the program was used to predict snow albedo on a highway. Marshall [1989] found good accuracy with her SNOALB model (predecessor to CAR) when compared to Warren and Wiscombe

[1980a,b]. This was expected since Marshall formulated her model by parameterization of the Warren and Wiscombe [1980a,b] theoretical models, but nonetheless shows agreement with a complex scattering model. Marshall [1989] also made comparisons of SNOALB to measured albedo values and found good overall correspondence.

In this thesis, additional verification was performed to assess whether there were any differences in predicting albedo in the environmental chamber versus the natural setting. One possible difference is the spectral behavior of the solar lamp compared to actual solar radiation. Across most of the spectrum the lamp closely matches the sun, but there are some small wavebands that do not. Here the influence of these differences could not be predicted. To investigate this influence the described hyperspectral imaging (HSI) system was employed to measure albedo for several snow samples [Resonon, Inc., 2004]. The instrument measured reflectivity (albedo) in the wavelengths from $0.40 - 0.90\,\mu m$ with accuracy diminishing at the ends of this range. Since the range of the HSI exists within the visible region, comparison to the CAR model was only applicable to the computed visible albedo in the wavelength up to $0.70\,\mu m$. Therefore, only the HSI wavelength data from $0.40 - 0.70\,\mu m$ was used to compare to the CAR visible albedo.

Five snow samples labeled as D1, D2, D3, MX, and N with thicknesses of $30\,cm$ (D1–D3), $22\,cm$ (N), and $5\,cm$ (MX) were placed in a $-10\,^{\circ}\mathrm{C}$ environment. Four distinct snow types were used throughout these samples with two created with newly fallen natural snow collected at a density of $105\,kg/m^3$. Figure 36 shows the various

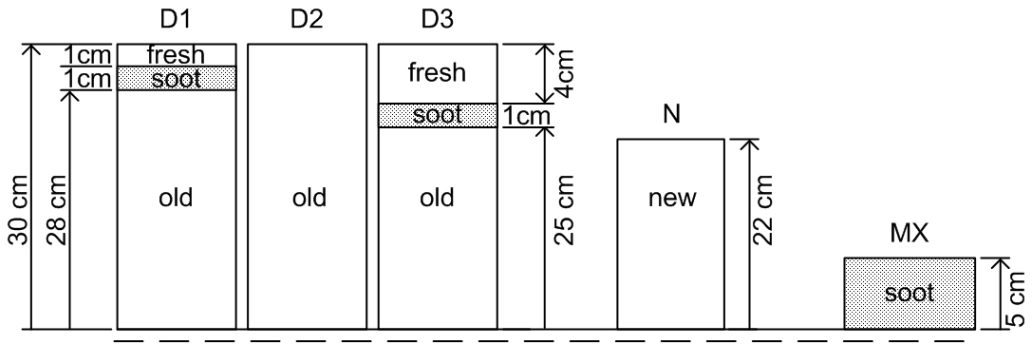

Figure 36. *Schematic of the five snow samples used for the HSI test. The four snow types are also shown configured for each sample.*

snow types and sample configurations. The first two snow types included an unaltered *new* type ($\rho = 105\,kg/m^3$) and a *fresh* type created with a #8 mesh US Standard Soils Sieve ($2.36\,mm$ openings)($\rho = 200\,kg/m^3$). The last two snow types were created with snow pulled from a storage freezer, which was used to create the following samples: a *old* type that was sifted ($\rho = 300\,kg/m^3$) and a *soot* type created by mixing powdered artist graphite throughout the *old* sample ($\rho = 300\,kg/m^3$). Samples D1–D3 were placed in an insulated, white styrofoam box with brown cardboard partitions while sample N was placed in a brown cardboard box. Each of these samples contained a combination of the snow-types described above. Sample N contained the *new* snow-type; samples D1, D2, and D3 contained the *old* snow-type while D1 and D3 contained a *soot* layer $1\,cm$ thick and *fresh* type. The *soot* type in D1 and D3 was respectively placed upon $28\,cm$ and $25\,cm$ of *old* with *fresh* added to each to complete the $30\,cm$ thickness. Sample MX contained a $5\,cm$ thick layer of *soot*.

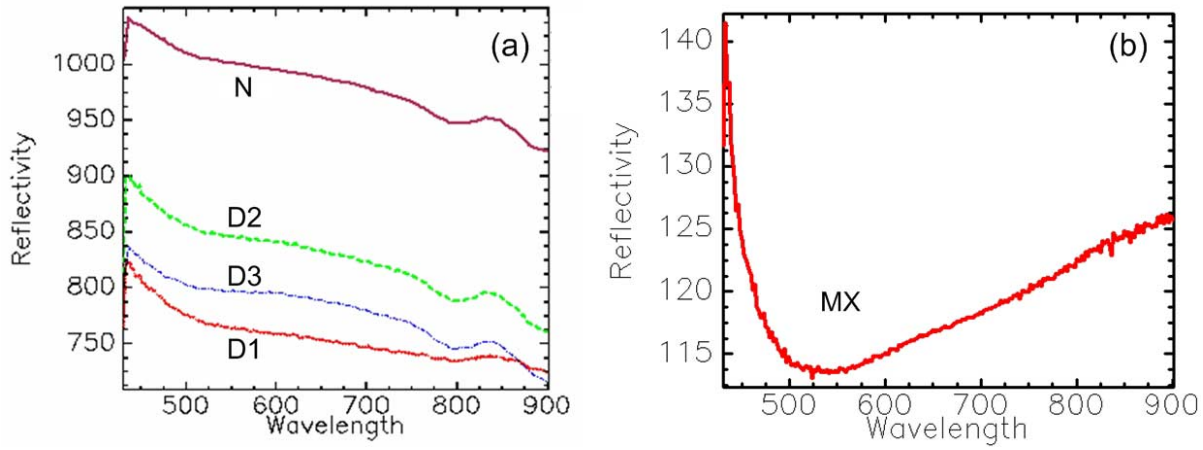

Figure 37. *Reflectivity measured with the HSI system. Reflectivity ranges from 0 to 1000, which corresponds to an albedo range from 0 to 1. In (a), sample N was the most reflective, followed by the sample D2, which had clean sifted snow. Samples D3 and D1 had* 1 *cm soot layers buried* 4 *cm and* 1 *cm below the surface, respectively. Since D3's soot layer is below that of D1, its reflectivity is higher indicating that the influence of the soot layer in D3 was less than D1. In (b) MX is shown as being the least reflective sample. MX's snow type was the same snow used for the soot layers in D1 and D3, which provides a good comparison of the effect of impurities in a snowpack.*

These snow samples were then measured with the HSI system yielding reflectivity values in the described waveband. Figure 37 shows the five samples and the corresponding reflectivity values. As expected the N sample was the most reflective followed by D2, which was the *old* snow type consisting of clean, sifted snow. Samples D3 and D1, which contained soot layers, followed as being less reflective than the other two samples. Sample MX was the least reflective of all the samples due to its purely homogeneous soot snow type. Critical mass cross-sections ($m_{xs,critical}$) were reached for all of the snow samples meaning that they could be considered semi-infinite with respect to the substrate. However critical values were not reached for some of the

distinct snow layers in the samples. For example in sample D1, the *fresh* layer itself could not be considered to be semi-infinite as the influence of the "substrate" or the soot layer had an effect on the overall albedo. In sample D3, this influence was less because the soot layer was placed deeper in the snowpack resulting in an albedo closer to *fresh*'s theoretical, semi-infinite albedo.

Table 2 shows the sample characteristics along with the HSI/CAR albedo (α_{VIS}) comparison. In order to compare a measured albedo from the HSI system a spectrally averaged value was obtained across the $0.40-0.70\,\mu m$ waveband to compare with the calculated albedo. Note the critical mass cross-section column in Table 2 showing the snow thickness required to reach a semi-infinite visible albedo value. For all of the samples, the critical mass cross-sections were less than the actual snow mass cross-sections implying that the cardboard and styrofoam substrates were negligible in the albedo calculation. The critical mass cross-section for the near-infrared (*NIR*) portion ($0.70-5.0\,\mu m$) of the shortwave spectrum was computed from CAR to occur in the top few millimeters, which follows results from Brandt and Warren [1993]. Since the *NIR* attenuates completely in the top few millimeters of the snowpack, the light available at depth contains just the visible (*VIS*) portion. Usually *VIS* does not absorb readily in the snowpack unless there exists some light absorbing impurities as in the case of the soot layers present in D1 and D3. These light absorbing impurities absorb some of the visible light thereby reducing the overall snowpack reflectivity/albedo.

Results show that the calculated CAR albedos corresponded reasonably well with the HSI measured values as shown in the last column of Table 2. It should be noted that when sieving snow, the optical properties of the snow are altered as the snow grains were broken resulting in different grain shapes, which can alter optical properties. To yield a computed CAR albedo close to the measured HSI values the samples with sifted snow required a large grain radius input value for CAR. These radius values are shown in Table 2 for each sample. Sample *new*, since it was not sifted, did not have this alteration of natural optical properties and did not require a modified grain size.

Table 2. *Properties of the snow samples used in the albedo validation. Shown are CAR calculated albedo values compared with the spectrally averaged measured values taken by the HSI system. Actual mass cross-section (m_{xs}) values are shown as well as the critical mass cross-section ($m_{xs,critical}$), which indicates the snow depth required to attain the maximum reflectivity value for a given snow type without the influence of an underlying substrate or different snow type. Also shown are the extinction coefficients as calculated by Equation 3.7 from CAR results.*

Sample	Layer	Radius (μm)	Soot ($ppmw$)	Density (kg/m^3)	Depth (cm)	m_{xs} (kg/m^2)	$m_{xs,critical}$ (kg/m^2)	Extinction Coefficient (cm^{-1})	α_{VIS} (CAR)	α_{VIS} (HSI)	Error (%)
N	new	50	0	105	22	23.1	9.9	0.49	0.98	0.98	0
D1	fresh	750	0	200	1	2	22.2	0.41	0.72	0.76	5.3
	soot	1000	0.001	300	1	3	0.36	38.38	0.13	-	-
	old	1000	0	300	28	84	24.2	0.57	0.91	-	-
D2	old	1000	0	300	30	90	24.2	0.57	0.91	0.86	5.8
D3	fresh	750	0	200	4	8	22.2	0.41	0.85	0.81	4.9
	soot	1000	0.001	300	1	3	0.36	38.38	0.13	-	-
	old	1000	0	300	25	75	24.2	0.57	0.91	-	-
MX	soot	1000	0.001	300	5	15	0.36	38.38	0.13	0.14	7.1

Experiments and Model Calculations

This section outlines the thirteen experiments performed in the environmental chamber and the criteria behind the chamber's settings for each experiment. Thermal model calculations are shown for each experiment along with the experimental results. Chamber settings and readings for each experiment are shown in Table 3. RH is the relative humidity, which was not an adjustable parameter but rather a measured chamber value. Most of the experiments involved two unique snow layers, which are indicated by the subscripts *new*, which is the top layer, and *old*, which is the bottom layer. Density and depth values for both of these layers are listed. The *Facets* column indicates whether any near-surface facets formed during the experiment.

Experiment #1

The first experiment was calculated at a relatively low shortwave value of $300\,W/m^2$ as measured by the Eppley PSP. This value was intended to find a rough lower bound of the needed incoming shortwave. The solar lamp was held constant throughout the duration of the experiment with no diurnal variations imposed. The reason for neglecting diurnal variations was to capture the quasi-steady state energy balance without adding further complexity. Density of the collected snow for the experiment was $195\,kg/m^3$ for the entire box depth. An initial snow grain picture was recorded and is shown in Figure 38(a) along with pictures taken at additional time steps. The ceiling temperature was set to $-40\,^{\circ}\mathrm{C}$ in the chamber. With the solar lamp set at

Table 3. *Environmental chamber experimental settings and measurements.*

EXP#	*Facets*	*Facet Size* (mm)	*SW* (W/m^2)	LW_{IN} (W/m^2)	*RH* (%)	T_{air} (°C)	T_{plate} (°C)	ρ_{new} (kg/m^3)	ρ_{old} (kg/m^3)	d_{new} (cm)	d_{old} (cm)	$\Delta T/\Delta x$ (°C/cm)
1		–	330	254	20	-10	-10	195	–	40	–	2.0
2	✓	1	595	273	15-20	-10	-10	174	–	40	–	3.5
3	✓	3/4	755	280	15-20	-10	-10	175	–	40	–	5.5
4	✓	1/2	1180	300	20-30	-10	-10	200	225	10	30	4.0
5	✓	1/4	755	280	30-35	-10	-10	250	305	12	28	4.0
6	✓	1/2	755	280	30-35	-10	-10	187	–	40	–	3.0
7	✓	1/2	755	280	30	-10	-10	270	320	10	30	1.5
8		–	208	242	30	-10	-10	170	320	16	24	1.0
9	✓	1/4	755	280	25	-10	-10	257	356	15	25	1.7
10	✓	1/4	755	266	27	-10	-10	240	360	15	25	2.0
11	✓	1/8	755	280	40	-10	-10	410	360	13	22	2.0
12		–	0	207	35	-10	-10	303	360	25	15	0.2
13	✓	1/2	755	280	30-35	-10	-10	300	360	25	15	2.0
H1	–	–	500	240	20	-10	-10	130	–	S.I.	–	–
H2	–	–	500	240	20	-10	-10	130	–	S.I.	–	–
H3	–	–	500	185	20	-10	-10	130	–	S.I.	–	–
H4	–	–	725	185	20	-10	-10	130	–	S.I.	–	–
H5	–	–	725	185	20	-10	-10	130	–	S.I.	–	–
H6	–	–	725	185	20	-10	-10	130	–	S.I.	–	–
H7	–	–	725	185	20	-10	-10	130	–	S.I.	–	–
H8	–	–	725	185	20	-10	-10	130	–	S.I.	–	–

NOTES:
- S.I. → Semi-infinite depth, i.e. $m_{xs} > m_{xs,critical}$
- *SW* → Shortwave irradiance setting of the solar lamp as measured by the Eppley PSP
- LW_{IN} → Incoming longwave radiation flux as measured by the Eppley PIR
- *RH* → Relative humidity measurement
- $\Delta T/\Delta x$ → Measured temperature gradient at 1 cm depth

$300\,W/m^2$, the incoming longwave radiation from the ceiling and lamp was measured by the Eppley PIR to be $220\,W/m^2$. The thermal contribution due to only the lamp's filament was approximately $15\,W/m^2$. Incoming longwave radiation when the solar lamp was off measured $205\,W/m^2$. Due to this additional longwave irradiance from the lamp's filament and separation glass temperature, future experiments where the solar lamp flux is increased are coupled with an increase in incoming longwave radiation because of the increased warmth of the lamp's filament and the ceiling glass. For reference, measured atmospheric incoming longwave radiation on a cold day with no cloud cover has been measured as $180 - 220\,W/m^2$ by Plüss [1997], which is within the flux range used for this first experiment. The chamber humidity value was measured at 20% (average) and recorded throughout the experiment. These values were then used in the thermal model to predict the turbulent flux exchange at the snow surface. The bottom boundary condition plate was set to $-10\,°C$, which varied little throughout the experiment due to plate temperature control. The room air temperature, set to $-10\,°C$, was kept constant throughout the experiment. The snow for this first experiment was stored in a freezer that was set at $-24\,°C$, where it had equilibrated. This storage temperature was the initial snow temperature for the experiment, which was carried out in the $-10\,°C$ chamber. Subsequent experiments were performed with the mean snowpack temperature close to the ambient chamber

Figure 39(a) shows the measured temperature profile throughout the snowpack at three hour intervals. The snow surface temperature was measured by the infrared

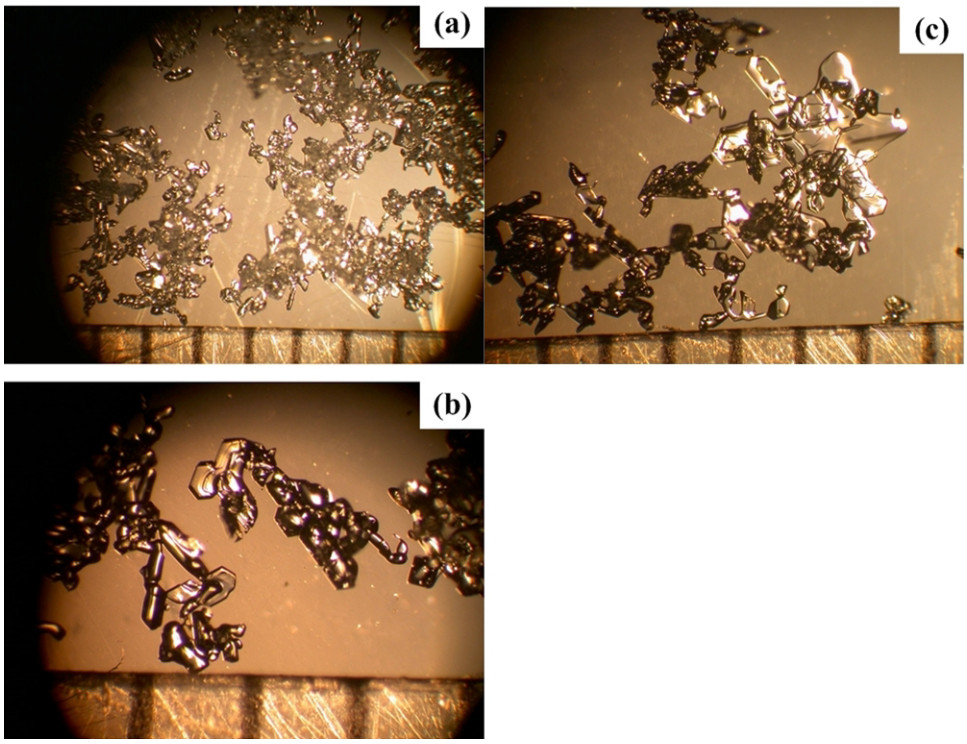

Figure 38. *Experiment #1 observed snow grains for (a) initial, (b) 10:00/surface, and (c) 18:00/surface (time=hr:min, grid scale=mm).*

temperature sensor and is included in the figure as the surface temperature. Notice the cold, initial temperature profile close to that of the storage freezer at $-24\,^{\circ}\mathrm{C}$. Part (b) of this figure shows a thermal model calculation of the temperature profile. For this profile the conductivity value used was $k_{eff} = 0.12\,W/m \cdot K$, which was calculated from Equation 2.6 restated here as,

$$k_{eff} = 0.021 + 2.5 \cdot \left(\frac{\rho}{1000}\right)^2$$

Grain observations were made at 10 and 18 hours into the experiment at the snow surface as shown in Figure 38(b) and (c), respectively. At these times only small facets

were found existing on the surface interspersed with a majority of rounded grains. Figure 39(d) shows the temperature gradients were measured to be over the threshold of $0.1\,^{\circ}\mathrm{C}/cm$, the point at where kinetic growth nominally occurs [Armstrong, 1985; McClung and Schaerer, 1993]. Even though the threshold gradient value was achieved, the mean snowpack temperature ($-11\,^{\circ}\mathrm{C}$ at 10 hours and $-9\,^{\circ}\mathrm{C}$ at 18 hours) was too cool and resulted in a too slow metamorphism rate to produce facets.

The occurrence of a "knee" near the surface in Figure 39(a-c) is common to nearly all of the experiments. The knee occurs when solar radiation penetrates a few centimeters and absorbs at depth. Some amount of *VIS* light can absorb in "clean" snow, and even "clean" snow can contain even a small amount of impurities that are capable of causing absorption. As shown in Figure 10(d) (page 26) the presence of impurities at $10^{-7}\,ppmw$ can alter the *VIS* absorption by lowering the *VIS* albedo (α_{VIS}). Most of the absorption occurs in the top few millimeters where the *NIR* shortwave radiation above $1.2\,\mu m$ attentuates [Brandt and Warren, 1993; Plüss, 1997]. In the next $3\,cm$ shortwave radiation in wavelengths above $1.0\,\mu m$ attenuates [Plüss, 1997]. While there still is a small amount of attenuation beyond $3\,cm$ most of the available solar energy available to absorb has been attenuated at this point. Cooling effects of longwave radiation and turbulent flux exchange counter the heating caused by solar radiation at the surface. However, these cooling fluxes occur only at the snow surface and do not directly cool the snow at depth. As a result, solar radiation absorbed at depth can only cool by heat conduction in the snow. At a quasi-steady

state time, the heating caused by solar absorption is balanced by the cooling effects mentioned at the surface with conduction.

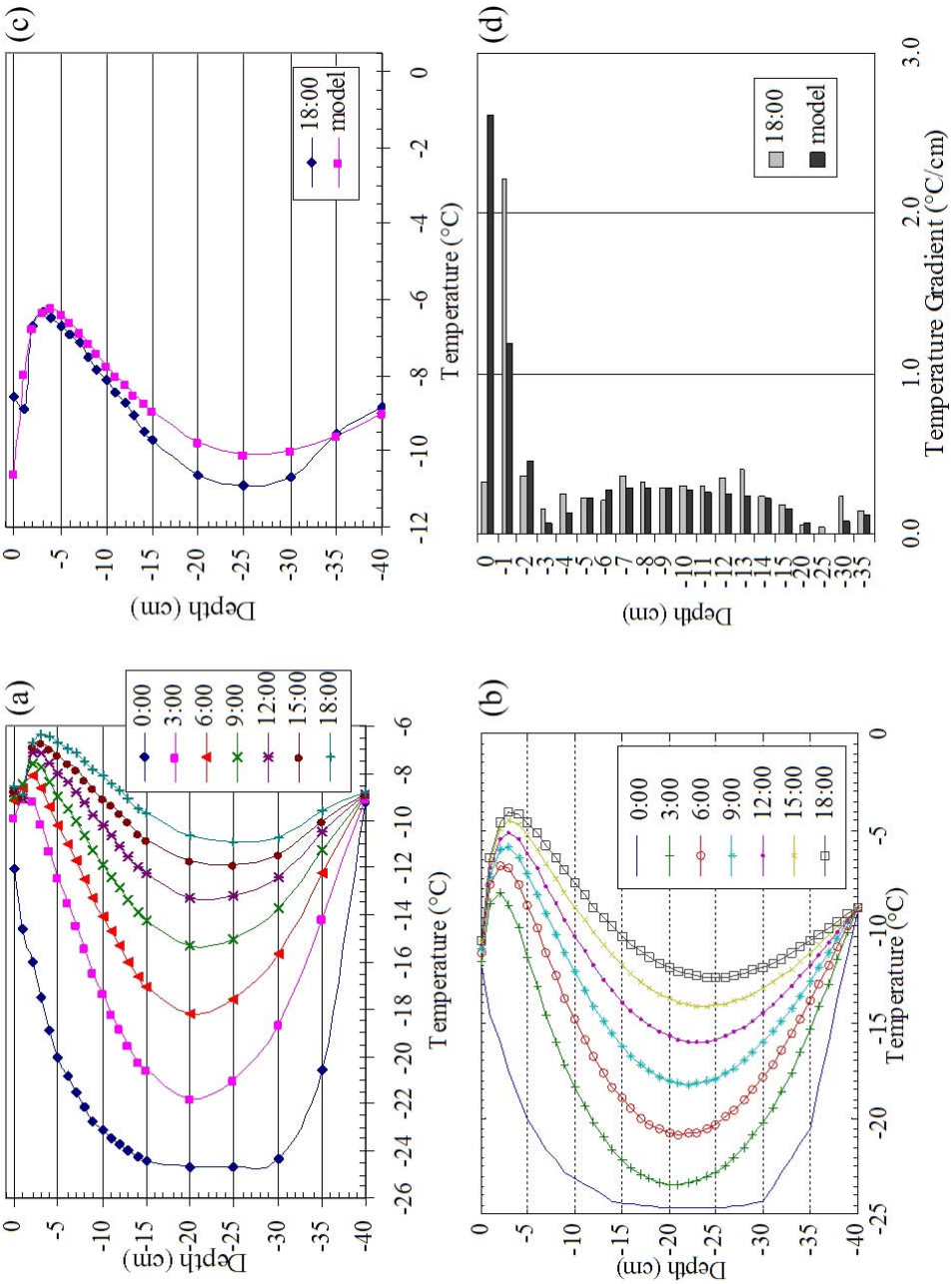

Figure 39. *Experiment #1 temperature profiles for the (a) experiment and (b) thermal model calculation with* $k_{eff} = 0.12\,W/m \cdot K$*. Comparative model/experiment temperature plots of the (c) profiles and (d) gradients are shown for the last recorded measurement time. A conductivity value of* $k_{eff} = 0.20\,W/m \cdot K$ *was used for (c) and (d).*

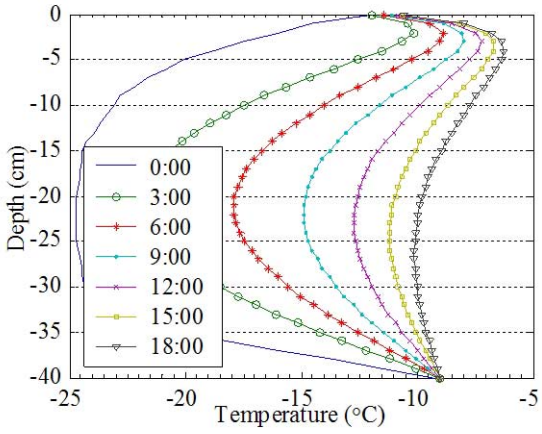

Figure 40. *Experiment #1 thermal model calculation for an increased thermal conductivity value of* $k_{eff} = 0.20\,W/m{\cdot}K$. *This model calculation was used for comparison to the experiment in Figure 39(c),(d).*

Figure 39(b) shows the thermal model result predicting the temperature profile with the boundary and snow conditions similar to the actual experiment and with the thermal conductivity calculated using Equation 2.6 (page 24) as $keff = 0.12\,W/m{\cdot}K$. Figure 40 shows the model calculation with a modified thermal conductivity value of $k_{eff} = 0.20\,W/m \cdot K$. This modified model calculation was used in Figure 39(c) and (d) to provide a comparison of the model and experiment for one time step, which was the experiment's last time step of 18 hours. The increased conductivity in Figure 40 created a cooler temperature profile because the snow became less insulative as compared to Figure 39(b). With a lower conductivity value, the model calculation in Figure 39(b) tended to build-up heat at depth. With the modification the model matches reasonably well with the experimental temperature profile in the top 15 cm of the snowpack. The experimental surface temperature does not show exact agreement

to the model where accurate estimation of surface conditions is difficult. Additionally, solar radiation absorption in the top snow layer is hard to estimate because of complex optics involving scattering and absorption occurring immediately at the surface. The described knee is evident in the model temperature profile. Table 4 shows the absorption of solar radiation in the top several centimeters of snow. Positive values indicate heat being added to the snowpack. Notice that the calculated contributions from Q_E (latent heat), Q_H (sensible heat), and Q_{LW} (net longwave radiation) are all surface phenomenon with values not specified below the surface. The sensible heat, Q_H is positive meaning that this term is adding energy to the snowpack. This addition is due to the air temperature being slightly warmer than the snow surface. The other terms are negative indicating energy loss. The column q''_g represents the additions of the first four columns for each snow layer or element. This value is compared to the computed net heat conduction flux occurring into the same layer. At a true steady state condition the conduction values will match the summed flux values where energy added to a differential element is balanced by conduction energy loss in the same element. The surface value for Q_{SW} shows a value smaller than the value in the layer below. This was due to the distance used to attenuate the solar radiation in the top layer where a value of $\Delta z/2$ was used in the Bouguer equation (3.14). This half distance is a result of the top node existing on the surface, which means that the control volume for this node is halved.

Table 4. *Experiment #1 flux values for several near-surface layers at time 18:00 using a conductivity value of $k_{\mathit{eff}} = 0.20\,W/m \cdot K$. The column q''_g is the sum of the preceding four columns.*

Depth	Q_{SW}	Q_E	Q_H	Q_{LW}	q''_g	q''_{cond}
-9	0.16	–	–	–	0.16	0.11
-8	0.30	–	–	–	0.30	-0.06
-7	0.58	–	–	–	0.58	-0.35
-6	1.10	–	–	–	1.10	-0.91
-5	2.12	–	–	–	2.12	-1.94
-4	4.05	–	–	–	4.05	-3.90
-3	7.76	–	–	–	7.76	-7.64
-2	14.87	–	–	–	14.87	-14.78
-1	28.49	–	–	–	28.49	-28.42
SFC	22.89	-13.66	2.21	-46.21	-34.78	34.83

The net heat conduction for a given layer was computed based on a finite difference approximation of the conduction component in the energy balance equation (3.41). This net conduction component may be approximated using a central-difference scheme as,

$$\begin{aligned} k\,\frac{\partial^2 T}{\partial z^2}dz &\cong k_{\mathit{eff},i} \cdot \left[\frac{T_{i+1} - 2\,T_i + T_{i-1}}{(\Delta z)^2}\right] \Delta z \\ &= k_{\mathit{eff},i} \cdot \frac{T_{i+1} - 2\,T_i + T_{i-1}}{\Delta z} \end{aligned} \tag{4.1}$$

which represents the net flux *into* the control volume for the z-direction. At the top boundary node, a similar central-difference approximation was made making use of

the fictitious node concept as given in Equation 3.54 (page 95),

$$
\begin{aligned}
k \left. \frac{\partial^2 T}{\partial z^2} dz \right|_n &\cong k_{\mathit{eff},n} \cdot \left[\frac{T_{n+1} - 2\,T_n + T_{n-1}}{(\Delta z)^2} \right] \Delta z \\
&= k_{\mathit{eff},n} \cdot \frac{T_{n+1} - 2\,T_n + T_{n-1}}{\Delta z} \\
&= k_{\mathit{eff},n} \cdot \frac{-2\,T_n + 2\,T_{n-1} + q''_{g,n} \cdot (2\Delta z / k_{\mathit{eff},n})}{\Delta z}
\end{aligned} \tag{4.2}
$$

Parameters used within the thermal model are presented in Table 5 for both this first experiment and all others. Snow parameters for only the top layer in the case of a double layer experiment are presented as these top layer properties are the most significant to temperature prediction. The effective thermal conductivity is strongly dependent on both density, which is a variable in Equation 2.6, as well as the ratio of the grain contact in the snow structure [Adams and Sato, 1993], which is not part of this equation. To some degree the conductivity is also a function of temperature although this dependence is weaker than the preceding two variables [Adams and Sato, 1993]. While the snow structure was not observed in situ, a reasonable variance in the effective thermal conductivity can be expected depending on structure. As a result the conductivities in some of the model calculations were increased. Snow handling procedure could increase the conductivity through agitation and breakage of the snow grains such that grain contact increases when sintering occurs.

Table 5. *Thermal model parameters used for each experimental temperature profile calculation.*

EXP#	ρ (kg/m^3)	C_p $(J/kg \cdot K)$	k_{eff} $(W/m \cdot K)$	Grain Radius (μm)	α_{top}	κ (m^{-1})	Parameters Changed
1	195	2030	0.20† (0.12)	150	0.75	65	k_{eff}
2	174	2030	0.10	50	0.81	82	–
3	175	2030	0.10	50	0.81	82	–
4	200	2030	0.12	88	0.78	78	–
5	250	2030	0.18	125	0.76	88	–
6	187	2030	0.11	188	0.74	59	–
6 (R2)	187	2030	0.20† (0.11)	–	0.84	70	k_{eff}, κ, α
7	270	2030	0.20	125	0.76	95	–
7 (R2)	270	2030	0.20	–	0.85	70	κ, α
8	170	2030	0.15† (0.09)	190	0.73	53	k_{eff}
9	257	2030	0.40† (0.19)	77	0.79	105	k_{eff}
10	240	2030	0.17	90	0.78	94	–
11	410	2030	0.75† (0.44)	100	0.78	80	k_{eff}
12	300	2030	0.25	–	–	–	–
13	300	2030	0.25	150	0.75	100	–
H1	130	2030	0.06	50	0.82	70	–
H2	130	2030	0.06	50	0.86	76	$\theta = 60°$
H3	130	2030	0.06	50	0.86	76	–
H4	130	2030	0.06	50	0.86	76	–
H5	130	2030	0.06	50	0.83	76	–
H6	130	2030	0.06	50	0.84	76	–
H7	130	2030	0.06	50	0.84	76	–
H8	130	2030	0.06	50	0.85	76	–

NOTES: All parameters listed are those for the top snow layers.
† Indicates that Equation 2.6 was not used to find k_{eff}.
R2 refers to run # 2.
For H5–H8, the soot layer $\kappa = 33800\, m^{-1}$.

Experiment #2

The incident shortwave flux was increased in this experiment to $650\,W/m^2$. The ceiling was kept at the same temperature of $-40\,^{\circ}\mathrm{C}$ as the first experiment, but the incoming longwave radiation increased to $235\,W/m^2$ due to a hotter lamp filament, which increased thermal radiation emission. The relative humidity was reduced by a factor of two to an average value of 10%. The effect of reducing the relative humidity influences the latent heat exchange by increasing the amount of heat loss from the snow surface. The snow had a density of $175\,kg/m^3$ for the entire $40\,cm$ thickness. A salient feature of this experiment over the last was the that the snowpack was allowed to equilibrate to the chamber conditions creating an initial warmer pack.

Figure 41(a) shows the experimentally measured temperature profile for the duration of the 8 hour experiment. Shown in the figure is a data set labeled *no sw*, which is a temperature profile obtained immediately after the 8:00 hour (hr:min) reading with the solar lamp turned off. This reading was taken in order to assess the amount of solar contamination/loading occurring in the thermocouple array. From the figure it is evident that the thermocouples near the surface are cooling by a degree Celsius in this short period of time. Thermocouples at depth are not affected as much because the amount of solar radiation available to absorb in the thermocouple is minimized. It is only near the surface where significant thermocouple absorption is occurring. The surface temperature in all of the experiments was measured with the IR temperature sensor, which provides a more accurate, non-solar contaminated

reading. Notice that the surface temperatures of both the 8:00 and *no sw* readings are identical. As discussed in the prior section the thermocouples and supporting array were painted white to minimize this absorption. While the paint no doubt helped avoid large measurement errors, small ones were still introduced. The *no sw* data set shows a more accurate profile and is used for comparison purposes. Unfortunately a similar data set was not obtained for the first experiment as the contamination was not discovered until this second experiment. The 8:00 hour data set shows the temperature reaching well above 0 °C to a value of +1.5 °C. This is not physically realistic as the temperature of an ice and water mixture does not exceed 0 °C while the two phases are present. Only when the ice phase is completely gone can water increase beyond 0 °C.

The *no sw* profile shows that that at a depth of approximately $-3\,cm$ the snow is starting to melt. This observation is in agreement with the model calculation shown in Figure 41(b) where the knee extends to 0 °C. With the parameters from Table 5 the model matched the experiment well as shown in Figure 41(c) showing the 8:00 and *no sw* temperature profiles for reference. Figure 41(d) shows the temperature gradients for the model and *no sw* data sets. The gradients in the top two layers are well over the threshold for kinetic growth. The calculated model flux values from this experiment are listed in Table 6.

Grain observations are shown in Figures 42 and 43 for times up to the 8:00 hour time step used for model/experiment comparison as well as for times extending to

nearly 20 hours. At the 9:40 observation, Figure 42(f), large facets approaching $1\,mm$ were observed. Figure 43 shows grains after nearly 20 hours of elapsed time. These observations show that under the sustained gradient from Figure 41(d) the facets eventually started to form needles,[1] which agrees with Figure 4 (page 9). This figure shows the preferred growth directions of snow crystals as a function of grain temperature and excess vapor density. The surface temperature during the experiment stayed at about $-8\,°\mathrm{C}$ (Figure 41(a)), which places the preferred growth direction along the c-axis of the crystal in the needle/sheath region of Figure 4 for a high excess vapor density. Thickness of the formed facet layer measured approximately $1-2\,mm$. Figure 43(a) and (b) show the grains at the surface and a few millimeters below the surface. The grains below the surface do not show the same degree of needle formation, in fact there appear to be are a few plate-like crystals. This observation contrasts to the observed grains at the 3:20 elapsed time shown in Figure 42(b)–(d). The surface grains at this observation time are plate-like facets while a few centimeters below the surface the grains appear similar to the initial grains (Figure 42(a)).

[1] This assertion was not verified using a cross polarization universal stage.

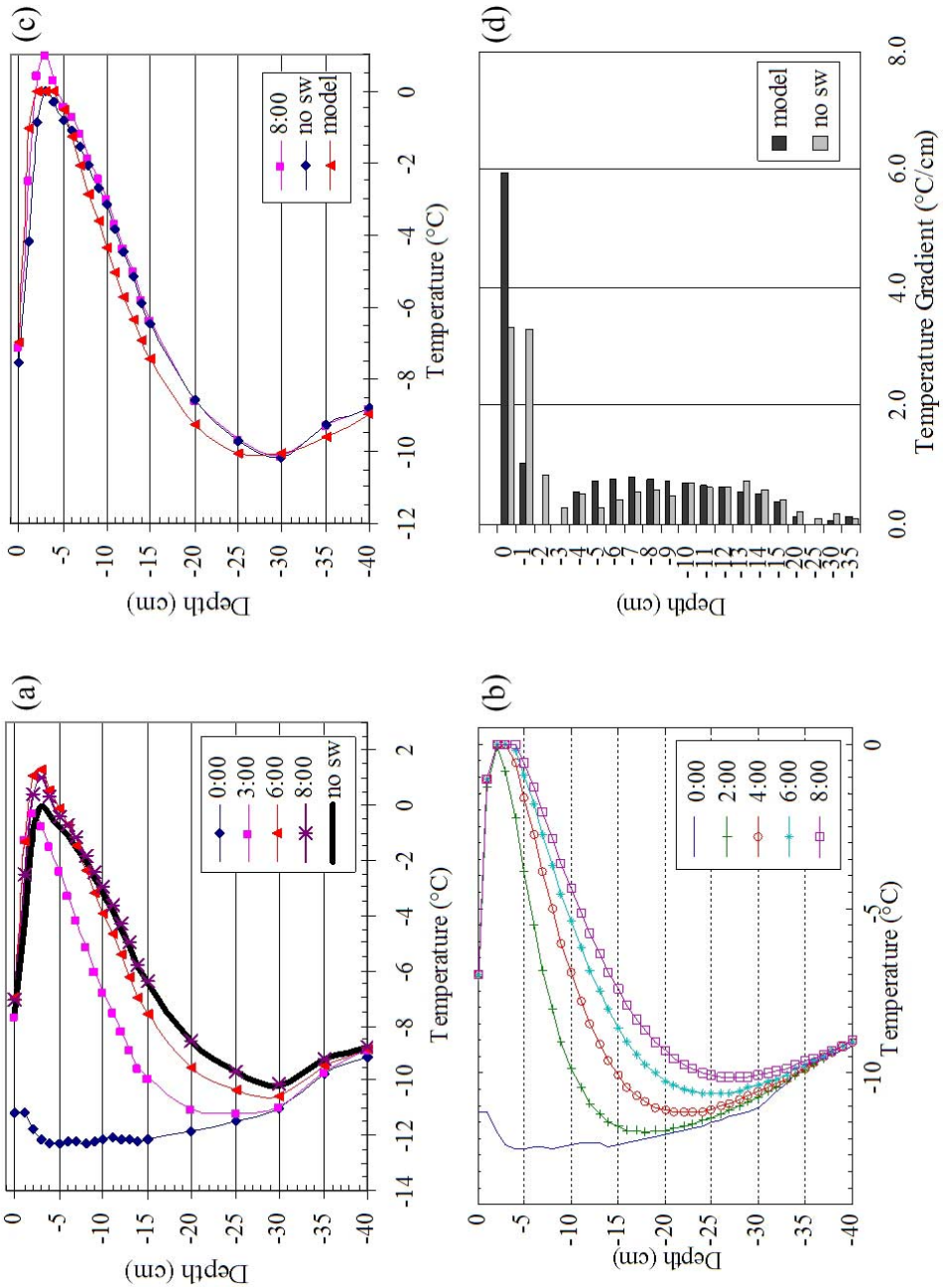

Figure 41. *Experiment #2 temperature profiles for the (a) experiment and (b) thermal model. Comparative model/experiment temperature plots of the (c) profiles and (d) gradients are shown for the last recorded measurement time.*

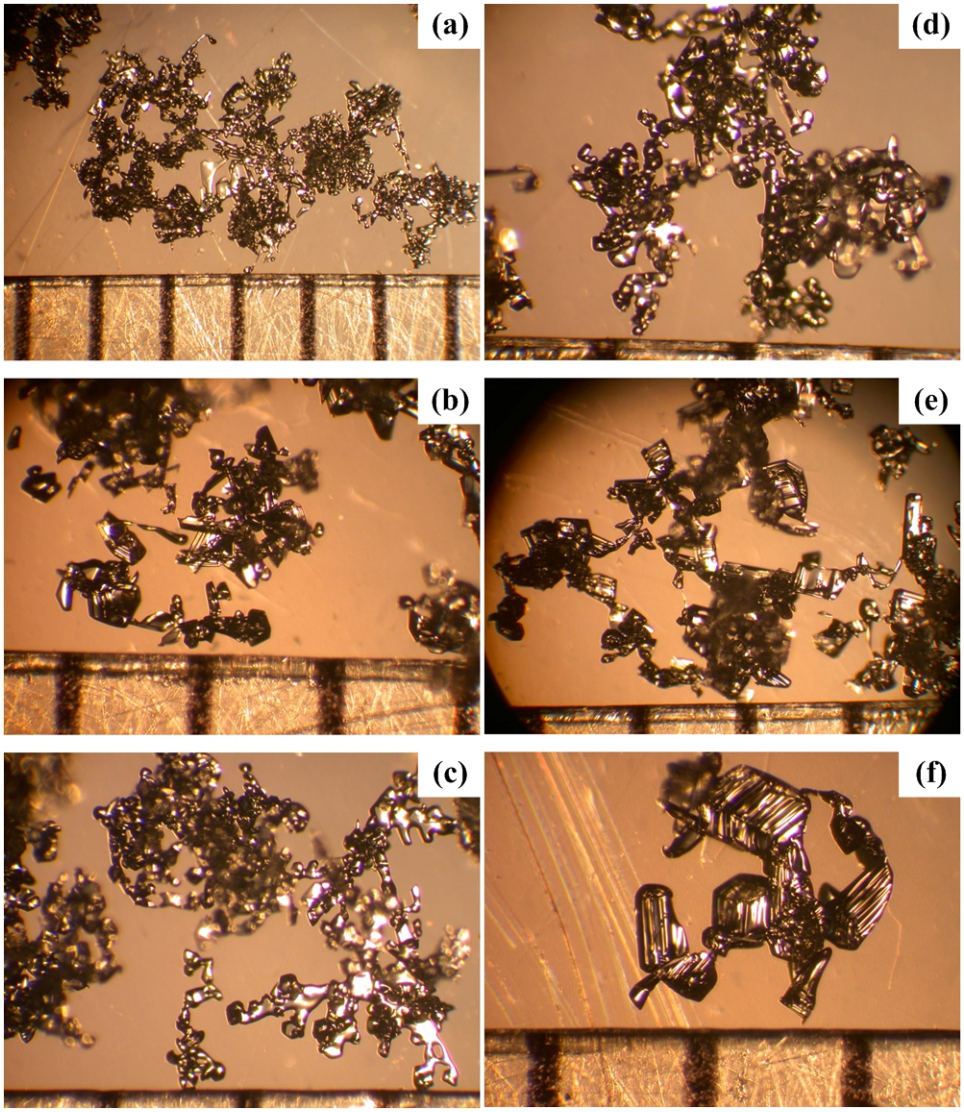

Figure 42. *Experiment #2 observed snow grains for (a) initial, (b) 3:20/surface, (c) 3:20/−1 cm, (d) 3:20/−2 cm, (e) 7:00/surface, and (f) 9:40/surface (time=hr:min, grid scale=mm).*

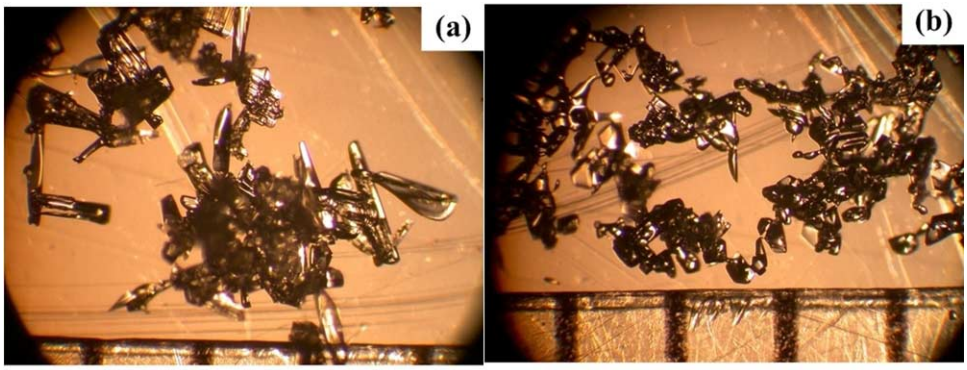

Figure 43. *Experiment #2 observed snow grains for (a) 19:40/surface, and (b) 19:40/below surface (time=hr:min, grid scale=mm).*

Table 6. *Experiment #2 flux values for several near-surface layers at time 8:00. The column q''_g is the sum of the preceding four columns.*

Depth	Q_{SW}	Q_E	Q_H	Q_{LW}	q''_g	q''_{cond}
-9	0.06	–	–	–	0.06	0.30
-8	0.15	–	–	–	0.15	0.17
-7	0.33	–	–	–	0.33	-0.08
-6	0.76	–	–	–	0.76	-0.59
-5	1.73	–	–	–	1.73	-1.71
-4	3.92	–	–	–	3.92	-5.53
-3	8.90	–	–	–	8.90	0.00
-2	20.20	–	–	–	20.20	-10.45
-1	45.86	–	–	–	45.86	-49.01
SFC	41.54	-22.27	-11.97	-45.97	-38.67	41.56

Experiment #3

Only the shortwave radiation flux changed from the last experiment (#2) as shown in Table 3. The value used in this experiment was $725\,W/m^2$, which corresponded to an incoming longwave radiation flux of $240\,W/m^2$. Figure 44 shows the grain observations and Figure 45 shows the experimental and model temperature profiles.

Table 7. *Experiment #3 flux values for several near-surface layers at time 10:20. The column q''_g is the sum of the preceding four columns.*

Depth	Q_{SW}	Q_E	Q_H	Q_{LW}	q''_g	q''_{cond}
-9	0.07	–	–	–	0.07	0.14
-8	0.16	–	–	–	0.16	0.01
-7	0.37	–	–	–	0.37	-0.25
-6	0.85	–	–	–	0.85	-0.77
-5	1.92	–	–	–	1.92	-2.63
-4	4.37	–	–	–	4.37	-2.63
-3	9.92	–	–	–	9.92	0.00
-2	22.53	–	–	–	22.53	-2.27
-1	51.16	–	–	–	51.16	-56.26
SFC	46.33	-24.00	-15.57	-44.83	-38.07	40.93

Again the *no sw* data set in Figure 45 shows a cooler temperature profile compared to the last measured data set, 10:20, over a time difference of less than one minute. The model profile shows good agreement with the experimental profile from the bottom to about $-8\,cm$ where the profiles diverge by 1.5 °C. Temperature gradients show good general agreement except for the top two snow layers. Here the model was unable to capture the small knee occurring at the surface. However the model's gradient for the top layer compares to the experimental gradient at $1\,cm$ below the surface. Table 7 lists the calculated model fluxes. Grain pictures show facets first observed at 3:30 on the surface and growing larger as observed at 6:30, 8:15, and 10:30. At these times, layers a centimeter below the surface exhibited no signs of faceting, but instead resembled the initial snow-type.

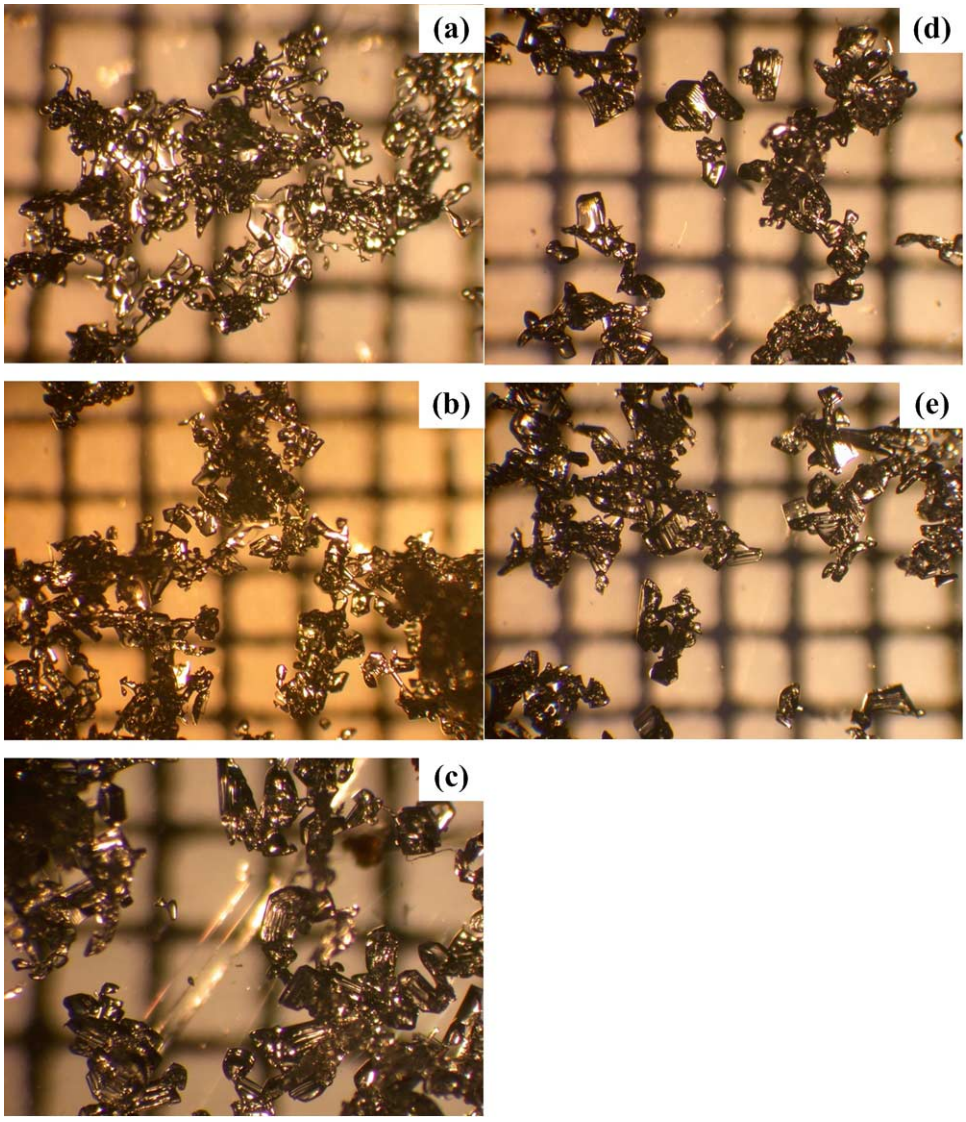

Figure 44. *Experiment #3 observed snow grains for (a) initial, (b) 3:30/surface, (c) 6:30/surface, (d) 8:15/surface, and (e) 10:30/surface (time=hr:min, grid scale=mm).*

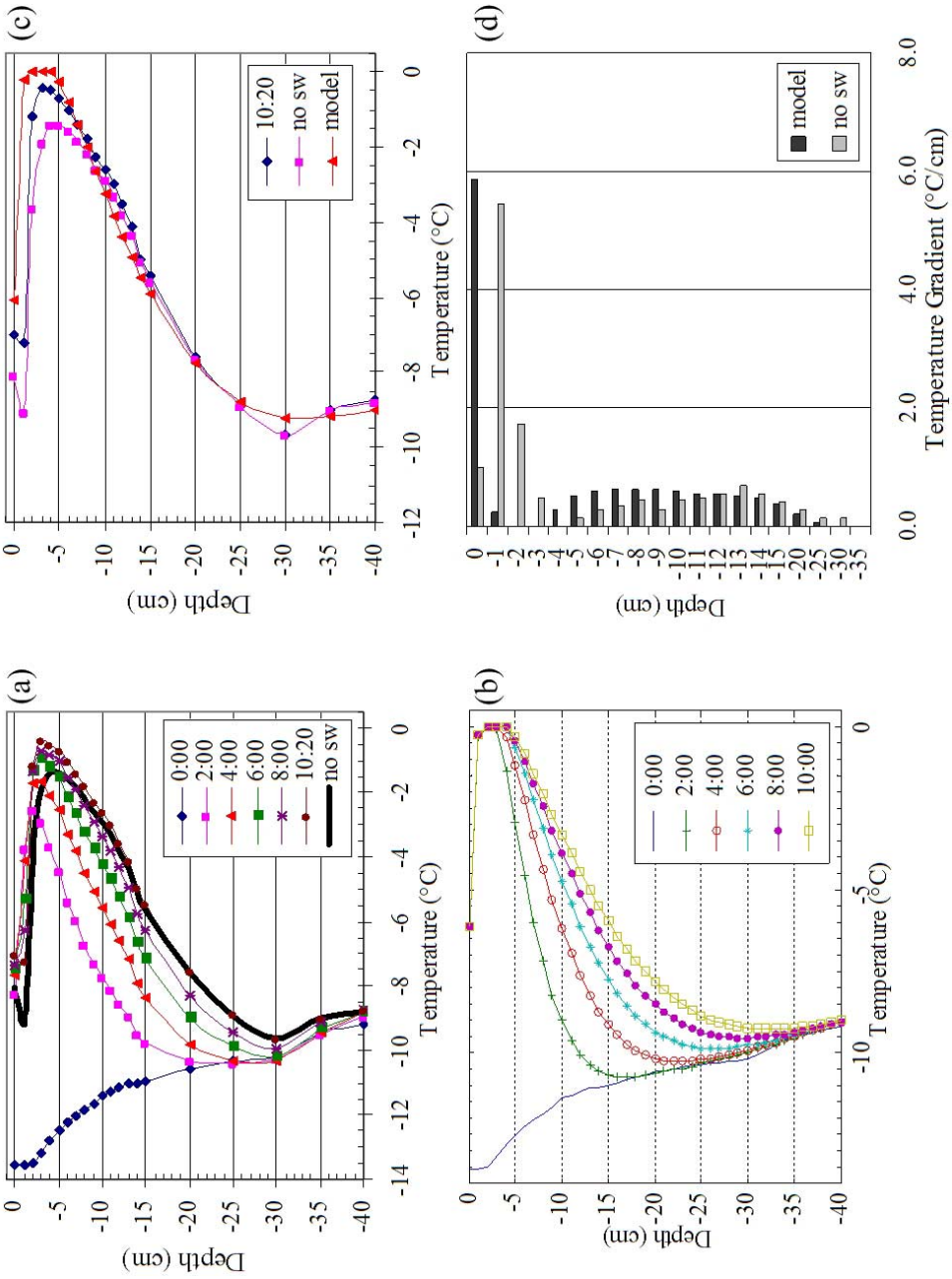

Figure 45. *Experiment #3 temperature profiles for the (a) experiment and (b) thermal model. Comparative model/experiment temperature plots of the (c) profiles and (d) gradients are shown for the last recorded measurement time.*

Experiment #4

When the previous experiment was finished the top $10\,cm$ of snow was removed and replaced with $200\,kg/m^3$ snow. From Table 3 this experiment was similar to experiment #1 with the same density and similar optical properties as shown in Table 5. However, the shortwave intensity was different with a chamber maximum setting of $1140\,W/m^2$ while the longwave intensity for this shortwave setting was $260\,W/m^2$. This value is well above conditions for a bright sunny day, but provides an interesting elevation in shortwave radiation. Figures 46 and 47 show the grain observations and the experiment/model temperature profiles. The experimental temperature profile shows large errors in the thermocouples due to solar contamination, which is emphasized by comparison between the *no sw* and 5:00 data sets in Figure 47(a). The *no sw* profile shows that the layers from -4 to $-7\,cm$ are at or just below $0\,^{\circ}$C. If the shortwave radiation were suddenly turned off or simply phased out as the case of sunset, this melt region would freeze creating an ice crust. This type of scenario has been observed by Birkeland et al. [1998]; Fukuzawa and Akitaya [1993]; Colbeck and Jamieson [2001]. The model predicts this melt behavior from -1 to $-4\,cm$, which is higher up in the snow than the actual experimental melt layer. Facets were observed at 3:00 and 5:00 hours on the snow surface.

Table 8. *Experiment #4 flux values for several near-surface layers at time 5:00. The column q''_g is the sum of the preceding four columns.*

Depth	Q_{SW}	Q_E	Q_H	Q_{LW}	q''_g	q''_{cond}
-9	0.18	–	–	–	0.18	0.42
-8	0.39	–	–	–	0.39	0.12
-7	0.85	–	–	–	0.85	-0.45
-6	1.86	–	–	–	1.86	-1.56
-5	4.06	–	–	–	4.06	-5.84
-4	8.86	–	–	–	8.86	-2.99
-3	19.33	–	–	–	19.33	0.00
-2	42.16	–	–	–	42.16	0.00
-1	91.97	–	–	–	91.97	-25.03
SFC	80.99	-32.96	-31.58	-42.40	-25.95	-1.82

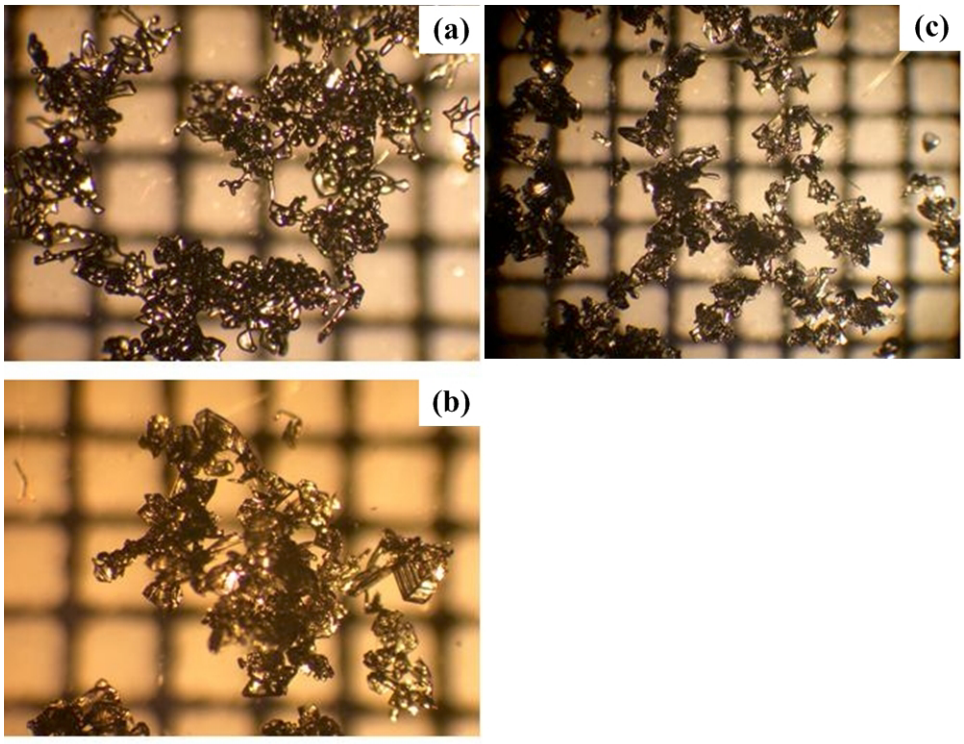

Figure 46. *Experiment #4 observed snow grains for (a) initial, (b) 3:00/surface, and (c) 5:00/surface (time=hr:min, grid scale=mm).*

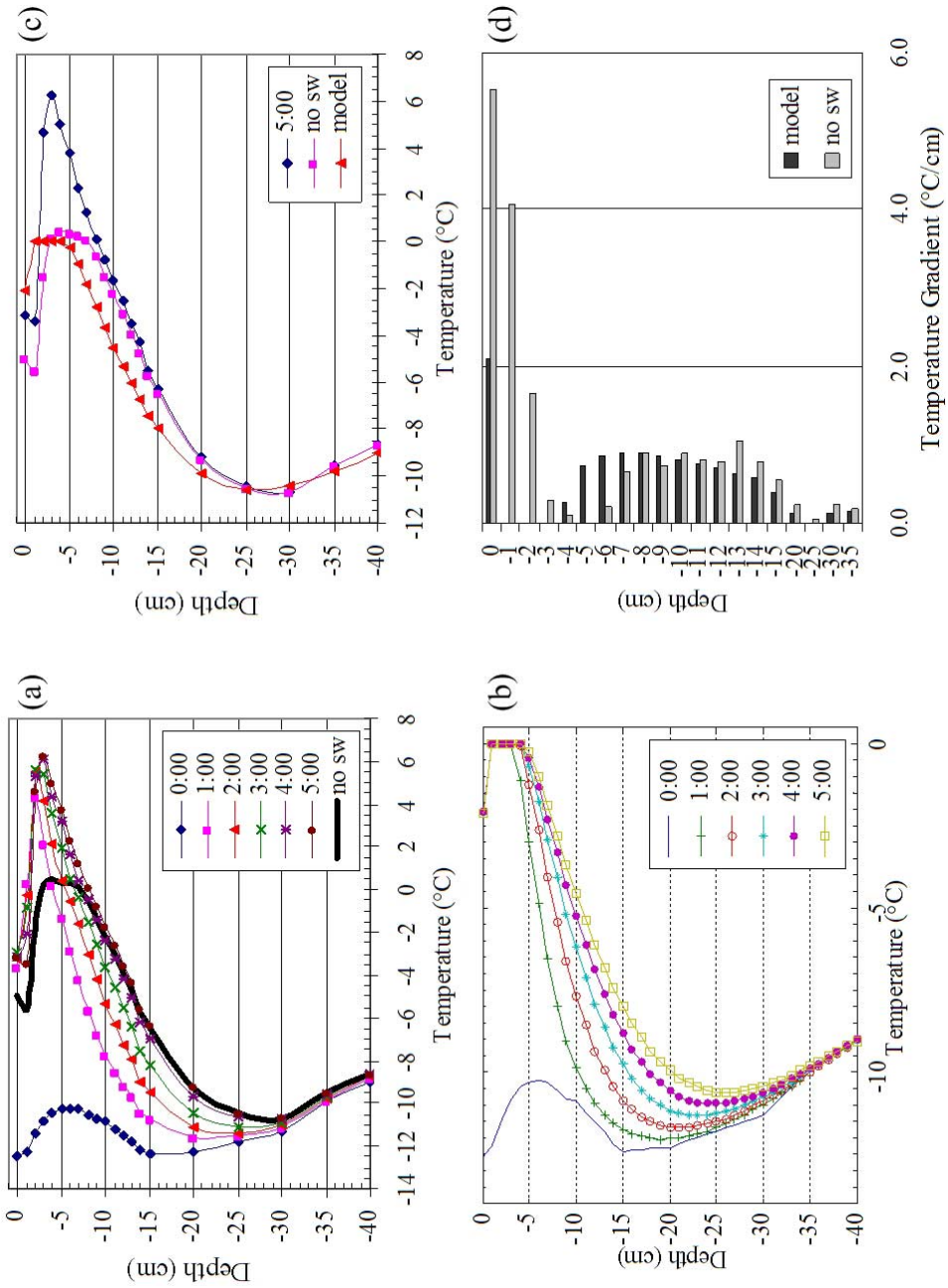

Figure 47. *Experiment #4 temperature profiles for the (a) experiment and (b) thermal model. Comparative model/experiment temperature plots of the (c) profiles and (d) gradients are shown for the last recorded measurement time.*

Table 9. *Experiment #5 flux values for several near-surface layers at time 13:00. The column q''_g is the sum of the preceding four columns.*

Depth	Q_{SW}	Q_E	Q_H	Q_{LW}	q''_g	q''_{cond}
-9	0.06	–	–	–	0.06	0.08
-8	0.14	–	–	–	0.14	-0.02
-7	0.33	–	–	–	0.33	-0.25
-6	0.81	–	–	–	0.81	-0.75
-5	1.94	–	–	–	1.94	-2.89
-4	4.68	–	–	–	4.68	-3.38
-3	11.28	–	–	–	11.28	0.00
-2	27.20	–	–	–	27.20	0.00
-1	65.58	–	–	–	65.58	-67.01
SFC	61.94	-26.70	-24.95	-55.02	-44.73	44.57

Experiment #5

12 cm of the top snow from experiment #4 were removed and replaced with snow of 250 kg/m^3 density. Figures 48 and 49 and Table 9 show the grain observations, the experimental/model temperature profiles, and model fluxes. Grain observations after 6:30 show a significant number of small facets forming, which may be classified as 4sf from the ICSI system [Colbeck et al., 1990]. Model results show melting in the top 5 cm, which differs from the *no sw* data set showing temperatures just below melting. Large temperature gradients are evident from Figure 49(d) exceeding 300 °C/m, which is well over the 10 °C/m threshold. These types of large gradients have been observed in the field by Birkeland et al. [1998] and experimentally by Fukuzawa and Akitaya [1993].

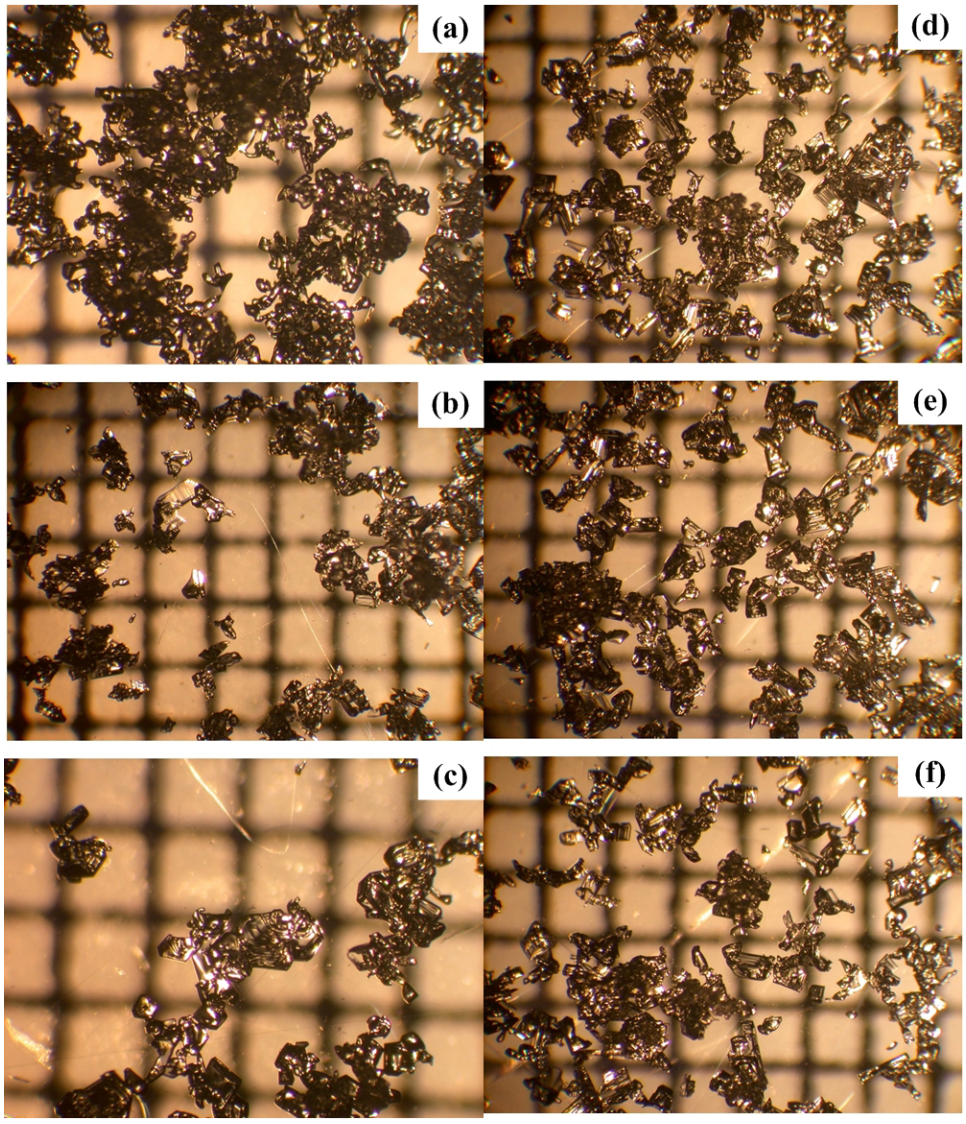

Figure 48. *Experiment #5 observed snow grains for (a) initial, (b) 6:30/surface, (c) 24:00/surface, and (d)–(f) 28:00/surface (time=hr:min, grid scale=mm).*

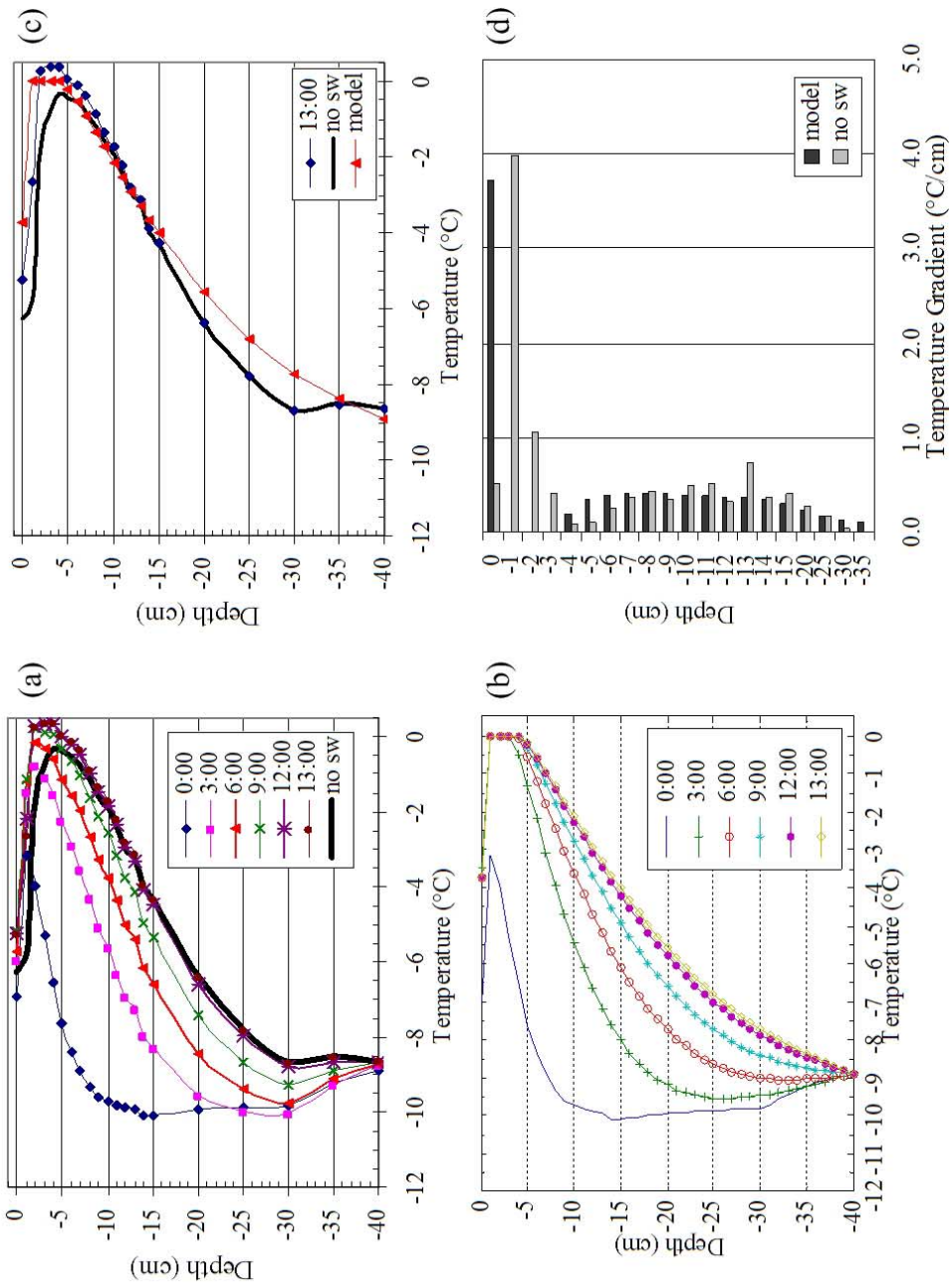

Figure 49. *Experiment #5 temperature profiles for the (a) experiment and (b) thermal model. Comparative model/experiment temperature plots of the (c) profiles and (d) gradients are shown for the last recorded measurement time.*

Experiment #6

Figures 50 and 51 and Table 10 show the grain observations, experimental/model temperature profiles, and model fluxes. This experiment had a slightly lower density value than the previous experiment with a density of $187\,kg/m^3$. The first model temperature calculation for this experiment did not sufficiently match the experimental profile. Figure 51(c) and 52 show this first calculation termed R1 where the parameters used are listed in Table 5. When compared to the experimental temperature measurements, this first calculation was about $1\,^{\circ}$C warmer near the surface and predicted melt at depths from -1 to $-6\,cm$. Only when the parameters α_{top}, κ, and k_{eff} were changed did the model profile resemble the experimental profile (see Table 5 for values) as shown in Figure 51(b) and (c). Model calculations were attempted keeping the CAR calculated albedo and extinction coefficients, but all calculations did not come close to matching the experimental profile. The grain observations show numerous facets occurring at time 5:40 on the surface.

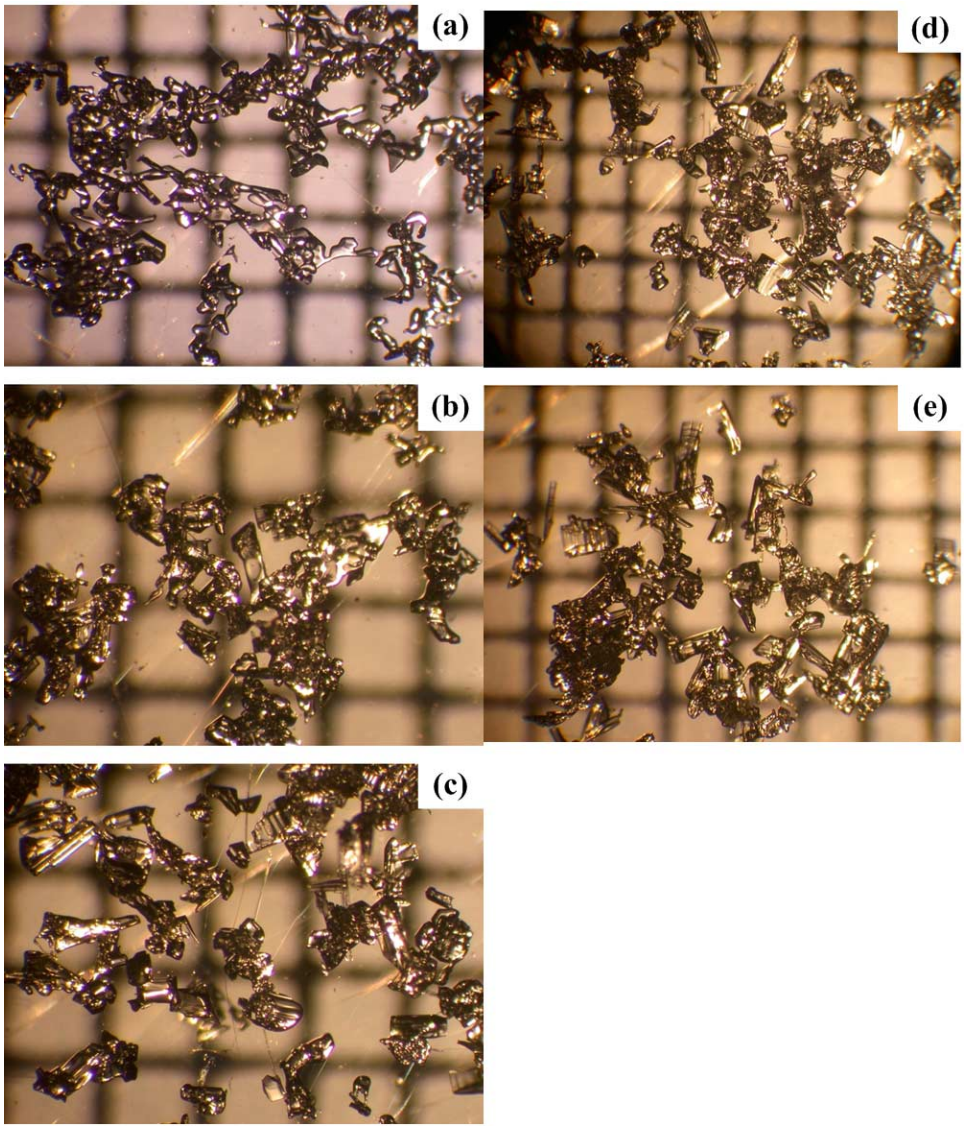

Figure 50. *Experiment #6 observed snow grains for (a) initial, (b) 5:40/surface, (c) 11:00/surface, (d) 22:15/surface, and (e) 22:45/surface (time=hr:min, grid scale=mm).*

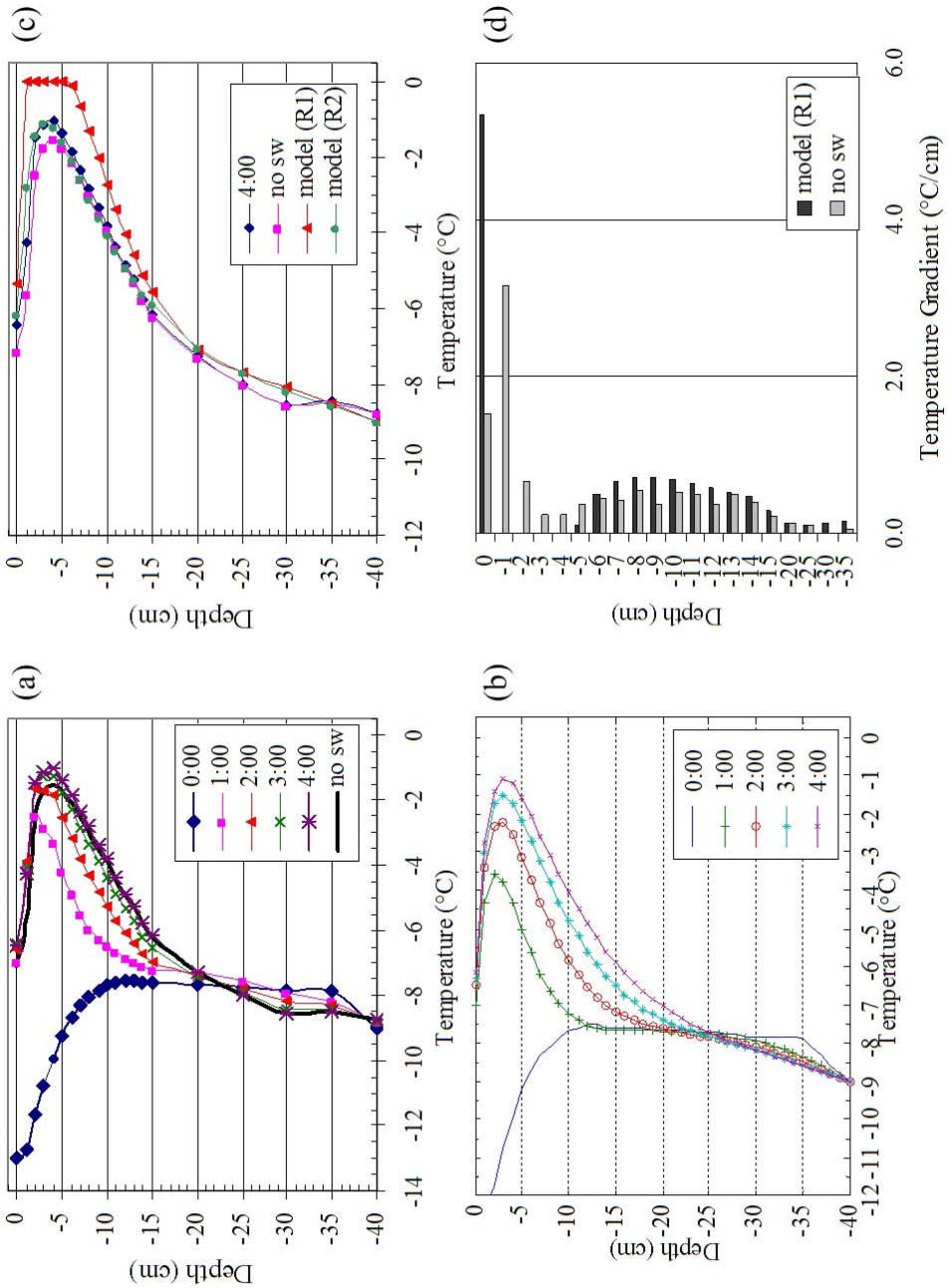

Figure 51. *Experiment #6 temperature profiles for the (a) experiment and (b) thermal model. Comparative model/experiment temperature plots of the (c) profiles and (d) gradients are shown for the last recorded measurement time. Model calculations in (b) and (c) used modified values of* k_{eff}, κ, *and* α.

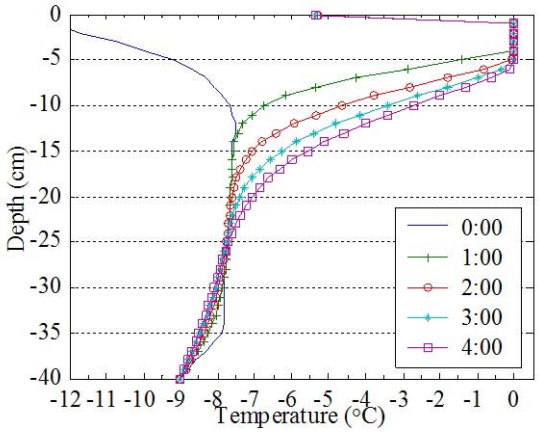

Figure 52. *Experiment #6 thermal model calculation for an increased thermal conductivity value of* $k_{eff} = 0.20\,W/m \cdot K$. *and modified* κ *and* α *values. This model calculation was used for comparison to the experiment in Figure 51(c) and (d).*

Table 10. *Experiment #6 flux values for several near-surface layers at time 4:00 using a conductivity value of* $k_{eff} = 0.20\,W/m \cdot K$ *and modified* κ *and* α *values. The column* q''_g *is the sum of the preceding four columns.*

Depth	Q_{SW}	Q_E	Q_H	Q_{LW}	q''_g	q''_{cond}
-9	0.15	–	–	–	0.15	0.50
-8	0.31	–	–	–	0.31	0.32
-7	0.62	–	–	–	0.62	-0.02
-6	1.24	–	–	–	1.24	-0.69
-5	2.50	–	–	–	2.50	-2.00
-4	5.04	–	–	–	5.04	-4.60
-3	10.15	–	–	–	10.15	-9.78
-2	20.44	–	–	–	20.44	-20.15
-1	41.15	–	–	–	41.15	-40.95
SFC	34.26	-19.85	-15.23	-44.46	-45.28	45.48

Experiment #7

Experiment #7 follows closely from the previous experiment increasing the density to $270\,kg/m^3$, which was used to replace $10\,cm$ of the top snow removed from the last experiment. Figure 53 shows the observed grains, Figures 54 and 55 show the experimental/model temperature profiles, and Table 11 lists the model fluxes. Using the calculated model optical parameters, κ and α, the model failed to accurately predict the temperature profile in the first calculation as shown in Figure 55 and 54(c) named as R1. The model's temperature divergence from the experimental values reached about $2\,^{\circ}$C near the surface. When the model parameters were changed as tabulated in Table 5, the profile began to match the experiment profile as shown in Figure 54(b) and plotted in (c) named as R2. Grain pictures show facet formation at the 3:00 time mark and beyond (Figure 53). The 7:00 observations show grain pictures immediately below the surface as well as at -1 and $-2\,cm$ depths. Just below the surface some facets were observed while below this level no facets were observed.

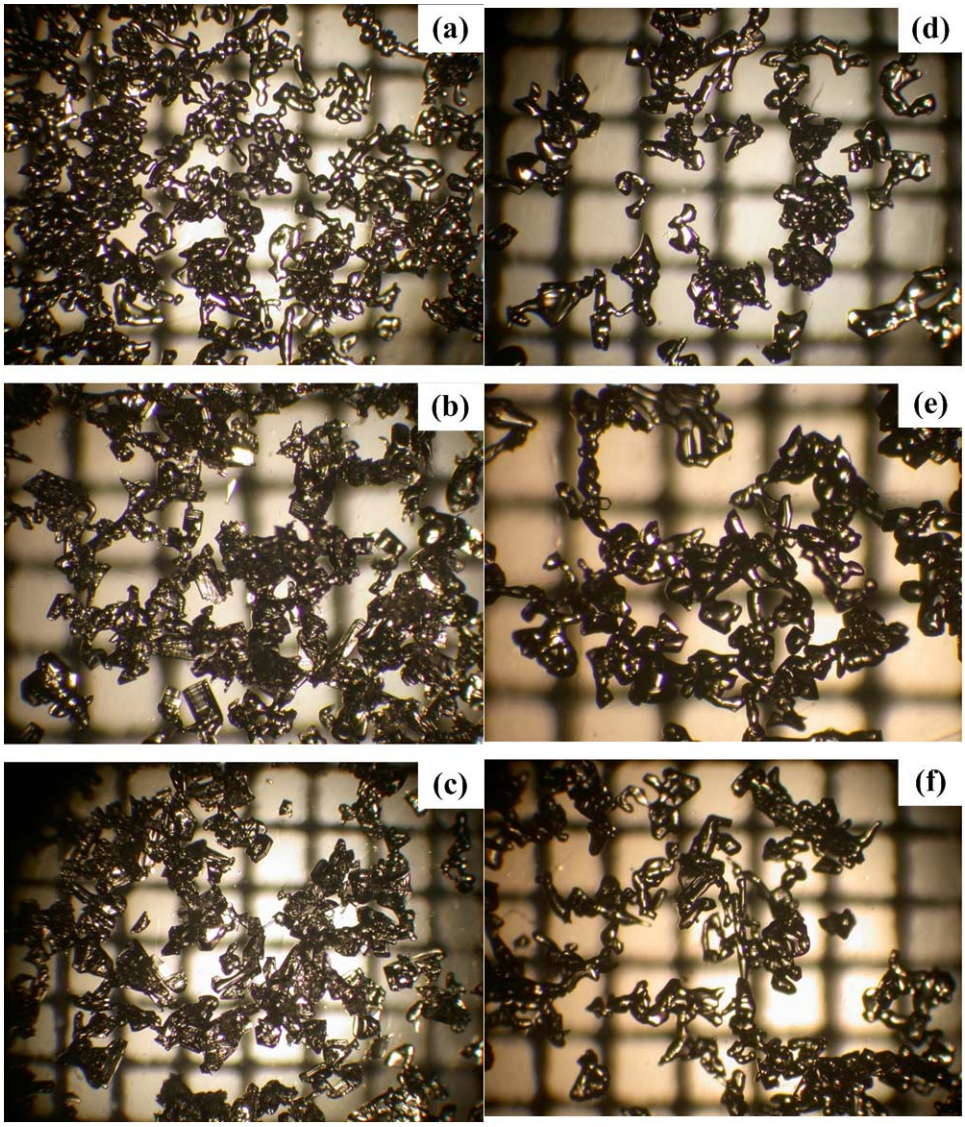

Figure 53. *Experiment #7 observed snow grains for (a) initial, (b) 3:00/surface, (c) 7:00/surface, (d) 7:00/below surface, (e) 7:00/−1 cm, and (f) 7:00/−2 cm (time=hr:min, grid scale=mm).*

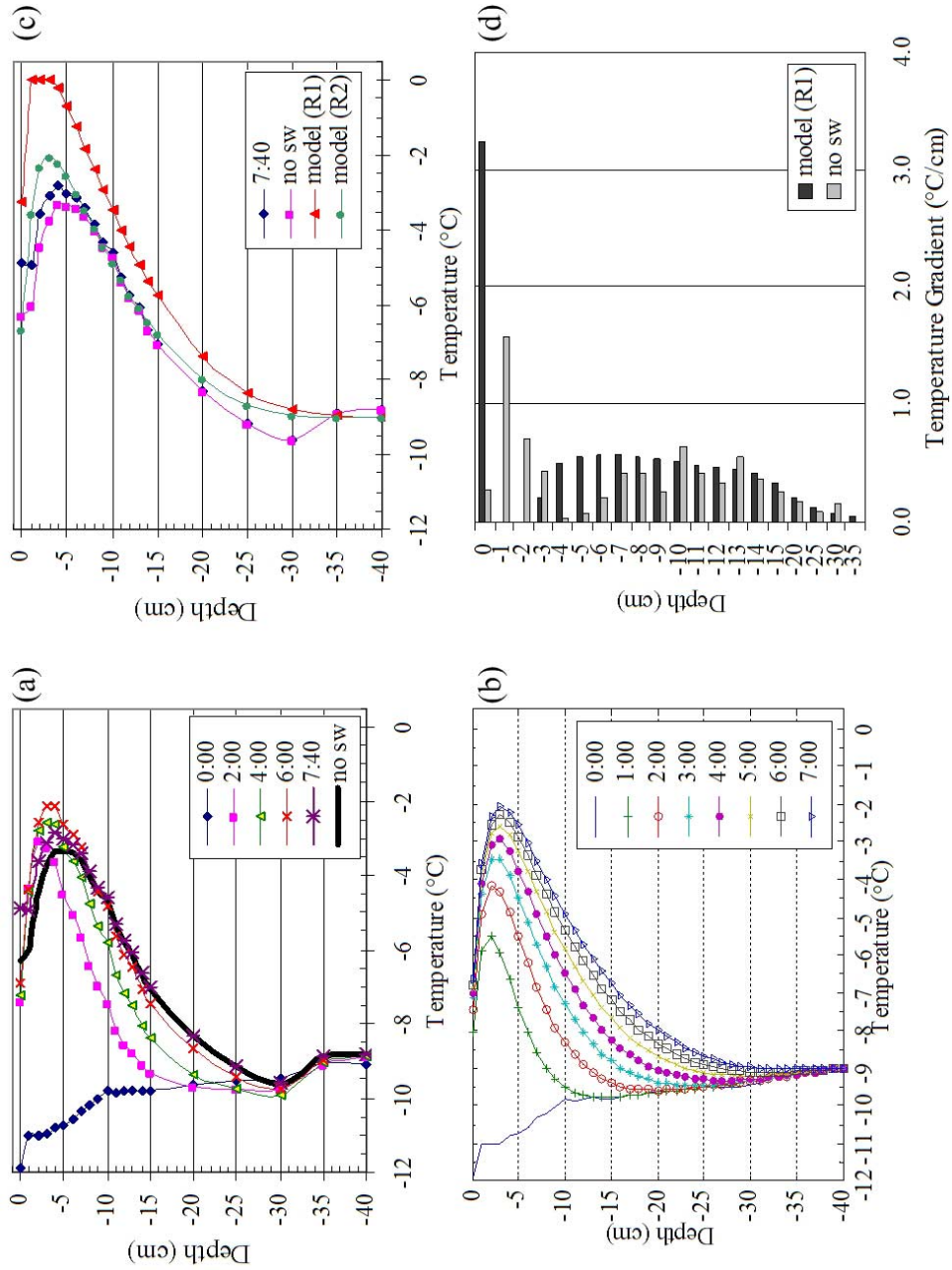

Figure 54. *Experiment #7 temperature profiles for the (a) experiment and (b) thermal model. Comparative model/experiment temperature plots of the (c) profiles and (d) gradients are shown for the last recorded measurement time. Model calculations for (b) and (c) used modified κ and α values.*

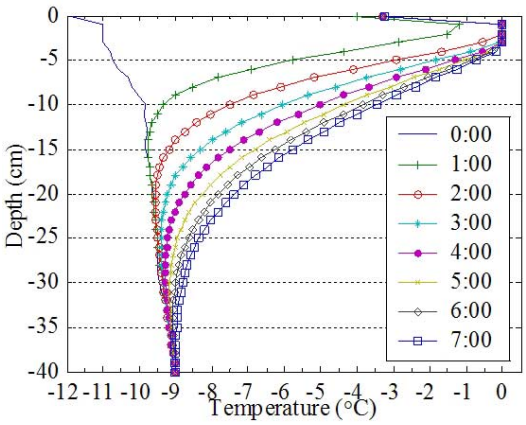

Figure 55. *Experiment #7 thermal model calculation for an increased albedo value of 0.85 and decreased extinction coefficient of* $70\,m^{-1}$*. This model calculation was used for comparison to the experiment in Figure 54(c),(d).*

Table 11. *Experiment #7 flux values for several near-surface layers at time 7:00 with modified values for* κ *and* α*. The column* q_g'' *is the sum of the preceding four columns.*

Depth	Q_{SW}	Q_E	Q_H	Q_{LW}	q_g''	q_{cond}''
-9	0.14	–	–	–	0.14	0.55
-8	0.29	–	–	–	0.29	0.34
-7	0.58	–	–	–	0.58	-0.05
-6	1.17	–	–	–	1.17	-0.81
-5	2.35	–	–	–	2.35	-2.28
-4	4.72	–	–	–	4.72	-5.22
-3	9.51	–	–	–	9.51	-11.13
-2	19.16	–	–	–	19.16	-23.05
-1	38.58	–	–	–	38.58	-47.00
SFC	32.12	-18.37	-13.25	-42.35	-41.85	71.13

Experiment #8

This experiment had the lowest solar lamp setting of $173\,W/m^3$. Density was measured at $170\,kg/m^3$, which was used to replace $16\,cm$ of top snow from the previous experiment. Figures 56 and 57 show the observed grains, Figures 58 and 59 show the experimental/model temperature profiles, and Table 12 lists the model fluxes. The first model calculation, using a calculated effective thermal conductivity value $k_{eff} = 0.09\,W/m{\cdot}K$, failed to closely predict the temperature profile as shown in Figure 59. When conductivity was increased to $k_{eff} = 0.15\,W/m^2$, the model temperature profile matched the experimental profile closer as shown in Figures 58(b) and (c). Grain pictures show mostly rounded crystals and no facets on the surface or below. While the temperature gradients have a numerical value expected to be in the kinetic growth region, the temperature of the snow at the location of these large gradients is around -11 to $-12\,^{\circ}$C, which may have been too cool to sustain rapid metamorphism.

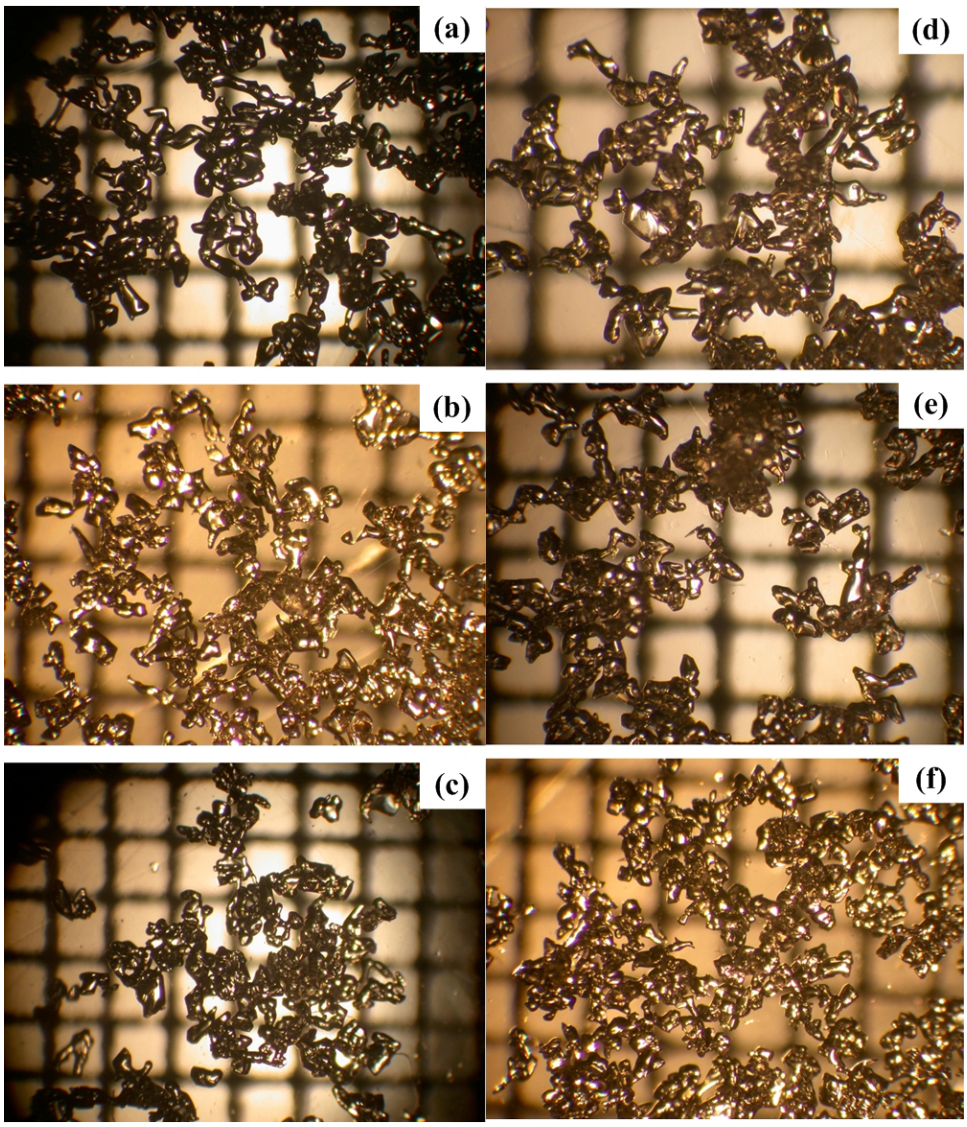

Figure 56. *Experiment #8 observed snow grains for (a) initial, (b) 3:30/surface, (c) 3:30/below surface, (d) 3:30/−1 cm, (e) 3:30/−2 cm, and (f) 6:15/surface (time=hr:min, grid scale=mm).*

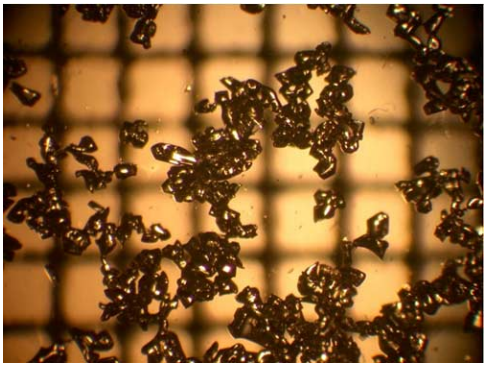

Figure 57. *Experiment #8 observed snow grains for 9:00/surface (time=hr:min, grid scale=mm).*

Table 12. *Experiment #8 flux values for several near-surface layers at time 8:00 using a conductivity value of* $k_{eff} = 0.15\,W/m \cdot K$. *The column* q''_g *is the sum of the preceding four columns.*

Depth	Q_{SW}	Q_E	Q_H	Q_{LW}	q''_g	q''_{cond}
-9	0.21	–	–	–	0.21	-0.17
-8	0.36	–	–	–	0.36	-0.33
-7	0.61	–	–	–	0.61	-0.58
-6	1.04	–	–	–	1.04	-1.01
-5	1.77	–	–	–	1.77	-1.74
-4	3.01	–	–	–	3.01	-2.97
-3	5.11	–	–	–	5.11	-5.06
-2	8.68	–	–	–	8.68	-8.64
-1	14.74	–	–	–	14.74	-14.64
SFC	10.87	-8.06	13.89	-39.49	-22.79	22.86

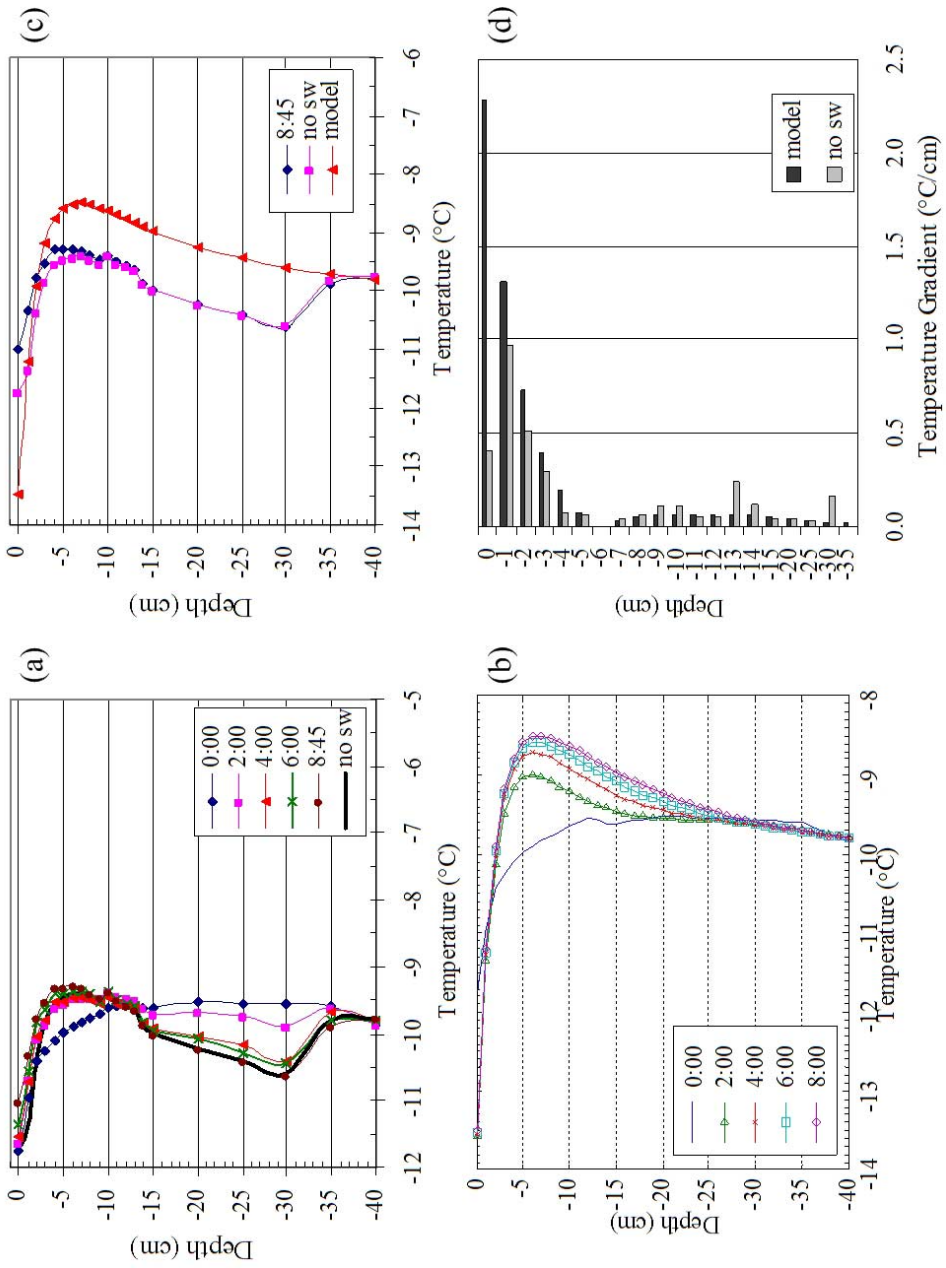

Figure 58. *Experiment #8 temperature profiles for the (a) experiment and (b) thermal model. Comparative model/experiment temperature plots of the (c) profiles and (d) gradients are shown for the last recorded measurement time. Model calculations in (b-d) used* $k_{eff} = 0.15\,W/m \cdot K$.

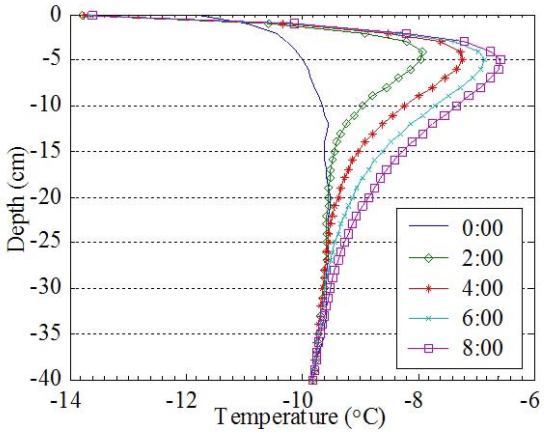

Figure 59. *Experiment #8 first thermal model calculation for thermal conductivity value of* $k_{eff} = 0.09\,W/m \cdot K$*. This value failed to accurately predict the experimental temperature profile in Figure 58(a).*

Experiment #9

15 cm of snow from the last experiment was removed and replaced by new snow with density 257 kg/m^3. Figure 60 shows the observed grains, Figures 61 and 62 show the experimental/model temperature profiles, and Table 13 lists the model fluxes. The first model calculation, shown in Figure 62, used an effective thermal conductivity calculated as $k_{eff} = 0.19\,W/m \cdot K$, which did not closely match the experiment temperature profile. When conductivity was increased to $0.40\,W/m \cdot K$, the profile yielded a closer match to the experimental profile as shown in Figure 61(b-d). Grain pictures show facets starting to form at time 3:15.

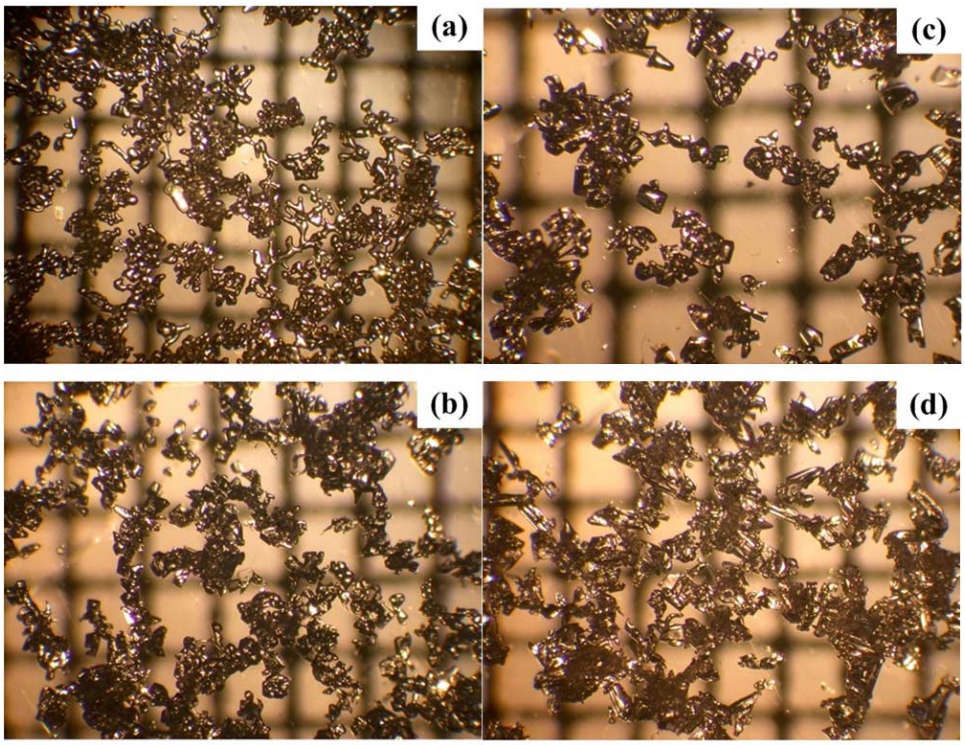

Figure 60. *Experiment #9 observed snow grains for (a) initial, (b) 3:15/surface, (c) 6:15/surface, and (d) 16:00/surface (time=hr:min, grid scale=mm).*

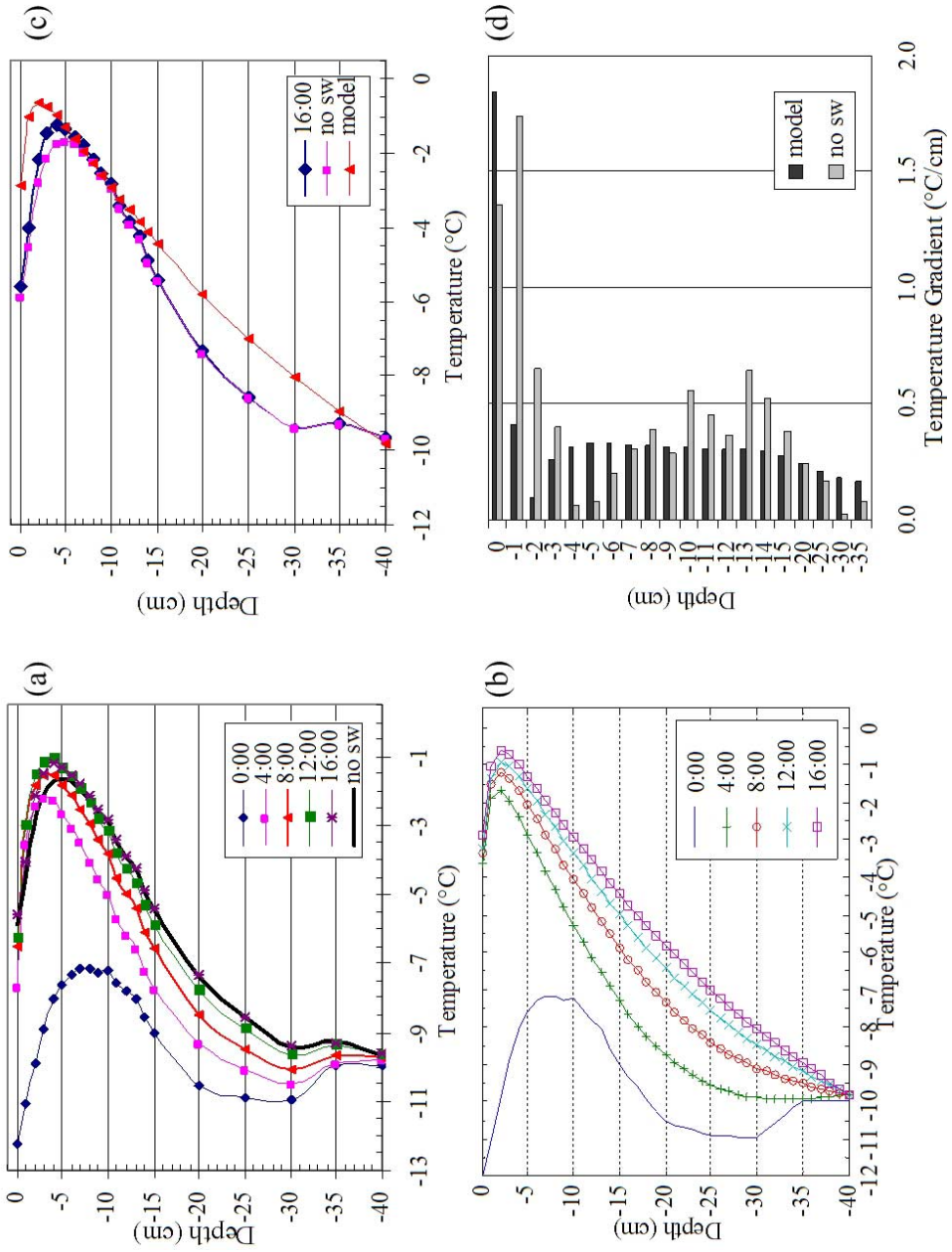

Figure 61. *Experiment #9 temperature profiles for the (a) experiment and (b) thermal model. Comparative model/experiment temperature plots of the (c) profiles and (d) gradients are shown for the last recorded measurement time. Model calculations for (b-d) used* $k_{eff} = 0.40\,W/m \cdot K$.

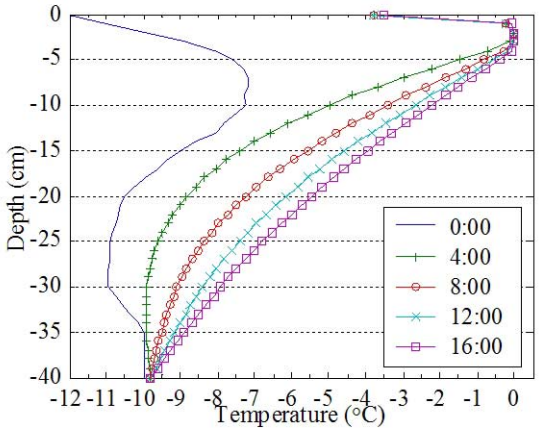

Figure 62. *Experiment #9 first thermal model calculation for a thermal conductivity value of* $k_{eff} = 0.19\,W/m \cdot K$. *This conductivity value did not accurately predict the experimental temperature profile in Figure 61(a).*

Table 13. *Experiment #9 flux values for several near-surface layers at time 16:00 using a conductivity value of* $k_{eff} = 0.40\,W/m \cdot K$. *The column* q''_g *is the sum of the preceding four columns.*

Depth	Q_{SW}	Q_E	Q_H	Q_{LW}	q''_g	q''_{cond}
-9	0.01	–	–	–	0.01	0.16
-8	0.04	–	–	–	0.04	0.16
-7	0.11	–	–	–	0.11	0.13
-6	0.31	–	–	–	0.31	0.00
-5	0.88	–	–	–	0.88	-0.51
-4	2.51	–	–	–	2.51	-2.07
-3	7.17	–	–	–	7.17	-6.68
-2	20.49	–	–	–	20.49	-20.13
-1	58.55	–	–	–	58.55	-57.44
SFC	62.19	-24.71	-28.12	-58.54	-49.19	49.13

Experiment #10

This experiment attempted to analyze the effect of increasing the amount of incoming longwave radiation by setting the ceiling to $-10\,^{\circ}\mathrm{C}$, which produced an incoming flux of $320\,W/m^2$. The net longwave flux, Q_{LW}, which includes incoming minus emitted radiation from the snow surface, was warming the snow surface at $8\,W/m^2$ as shown in Table 14. The shortwave was set at $755\,W/m^2$. Relative humidity in the chamber was high at 57% because of the relatively warm ceiling temperature, which was unable to condense out air moisture, which was possible when the ceiling was set at $-40\,^{\circ}\mathrm{C}$. Snow with density of $240\,kg/m^3$ replaced $15\,cm$ of snow from the previous experiment. The model correctly predicted a $0\,^{\circ}\mathrm{C}$ layer below the surface, but failed to accurately predict the surface temperature to within a few degrees. As shown in Figure 65(a) the experimental temperature measurements at time 7:30 shows significant solar contamination of the thermocouples reading a maximum of $+4\,^{\circ}\mathrm{C}$. The *no sw* profile corrects these readings to $0\,^{\circ}\mathrm{C}$ at this maximum. Grain pictures in Figures 63 and 64 show some faceting activity starting at about 7:20. The time when facets first appeared in this experiment was a few hours longer than other experiments. This may have been due to the temperature gradient at the surface shown in Figure 65(d), which was generally lower than those experiments producing facets in a couple hour time frame. The net longwave flux was not cooling as usual and thus lowered the imposed temperature gradient.

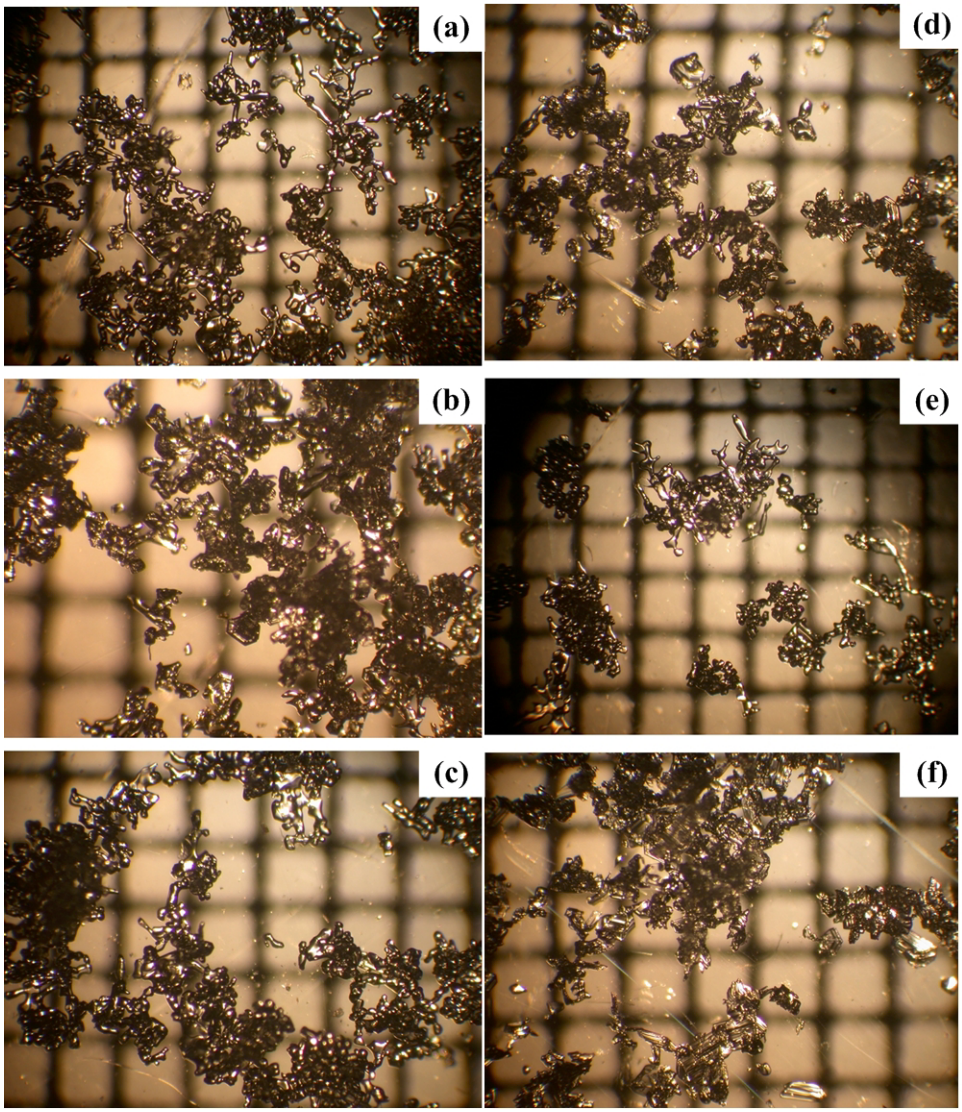

Figure 63. *Experiment #10 observed snow grains for (a) initial, (b) 1:00/surface, (c) 1:00/below surface, (d) 2:20/surface, (e) 2:20/below surface, and (f) 4:20/surface (time=hr:min, grid scale=mm).*

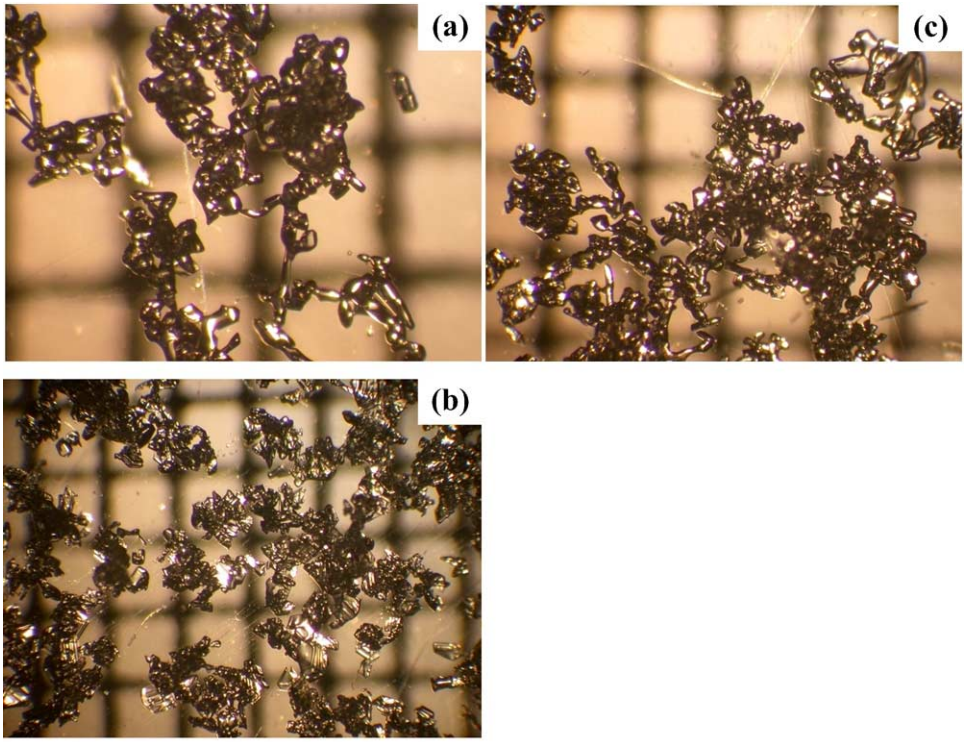

Figure 64. *Experiment #10 observed snow grains for (a) 4:20/below surface, (b) 7:20/surface, and (c) 7:20/below surface (time=hr:min, grid scale=mm).*

Table 14. *Experiment #10 flux values for several near-surface layers at time 7:00. The column q''_g is the sum of the preceding four columns.*

Depth	Q_{SW}	Q_E	Q_H	Q_{LW}	q''_g	q''_{cond}
-9	0.03	–	–	–	0.03	0.25
-8	0.08	–	–	–	0.08	0.15
-7	0.22	–	–	–	0.22	-0.03
-6	0.55	–	–	–	0.55	-0.43
-5	1.41	–	–	–	1.41	-1.47
-4	3.62	–	–	–	3.62	-6.53
-3	9.27	–	–	–	9.27	0.00
-2	23.73	–	–	–	23.73	0.00
-1	60.75	–	–	–	60.75	0.00
SFC	59.81	-31.94	-39.74	8.33	-3.54	7.08

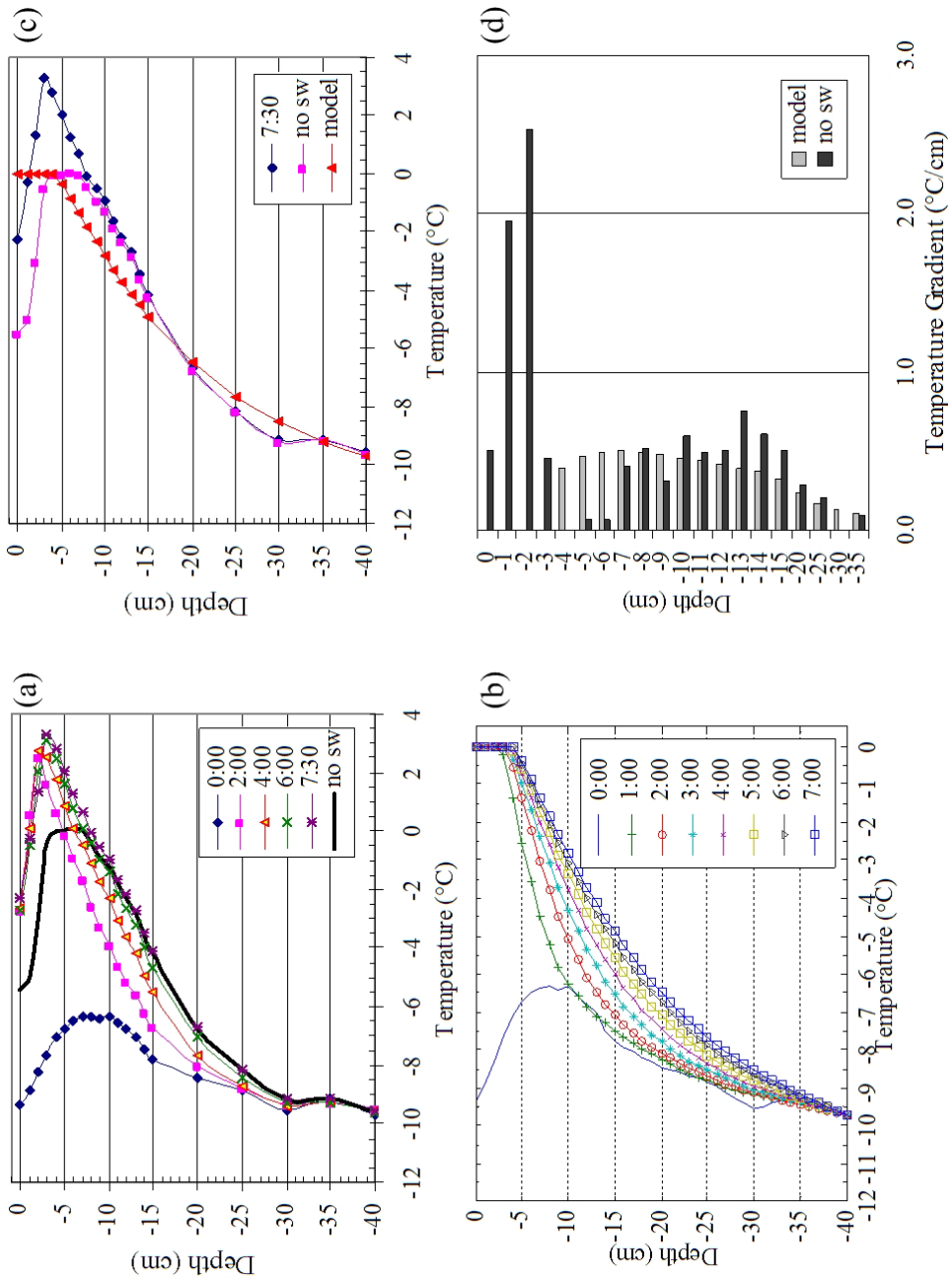

Figure 65. *Experiment #10 temperature profiles for the (a) experiment and (b) thermal model. Comparative model/experiment temperature plots of the (c) profiles and (d) gradients are shown for the last recorded measurement time.*

Experiment #11

The effect of increasing the snow density was investigated in this experiment with new snow at $410\,kg/m^3$ used to replace $18\,cm$ snow from the previous experiment. To achieve this relatively high density value, snow was sieved through a #4 mesh US Standard Soils Sieve and then artificially compacted to the stated density. Figure 66 shows observed snow grains, Figure 67 shows the experimental/model temperature profiles, and Table 15 lists the model fluxes. The calculated effective thermal conductivity was first set at $0.44\,W/m \cdot K$ and the model profile using this value is shown in Figure 67(c) labeled as R1. This value seemed to predict the conductivity too low and when with an increased value of $0.75\,W/m \cdot K$ the model calculated a more accurate profile as shown in the same figure labeled as R2. When snow is sieved, grains are broken apart resulting in a conglomeration of more uniform and rounded snow grains. Due to the rounded nature sintering occurs in this sieved snow increasing the grain connectedness, which increases the thermal conductivity as discussed on page 24. For this reason increasing the conductivity seemed reasonable. Grain pictures reveal some small ($< 1/8\,mm$) facets forming at the surface at 3:00 and 6:00 times, but their size is small compared to other experiments.

Table 15. *Experiment #11 flux values for several near-surface layers at time 9:00 using a conductivity value of* $k_{eff} = 0.75\,W/m \cdot K$. *The column* q''_g *is the sum of the preceding four columns.*

Depth	Q_{SW}	Q_E	Q_H	Q_{LW}	q''_g	q''_{cond}
-9	0.10	–	–	–	0.10	0.25
-8	0.22	–	–	–	0.22	0.10
-7	0.50	–	–	–	0.50	-0.18
-6	1.10	–	–	–	1.10	-0.81
-5	2.45	–	–	–	2.45	-2.18
-4	5.46	–	–	–	5.46	-5.22
-3	12.16	–	–	–	12.16	-11.93
-2	27.06	–	–	–	27.06	-26.86
-1	60.21	–	–	–	60.21	-60.04
SFC	53.78	-26.80	-25.97	-56.15	-55.14	55.32

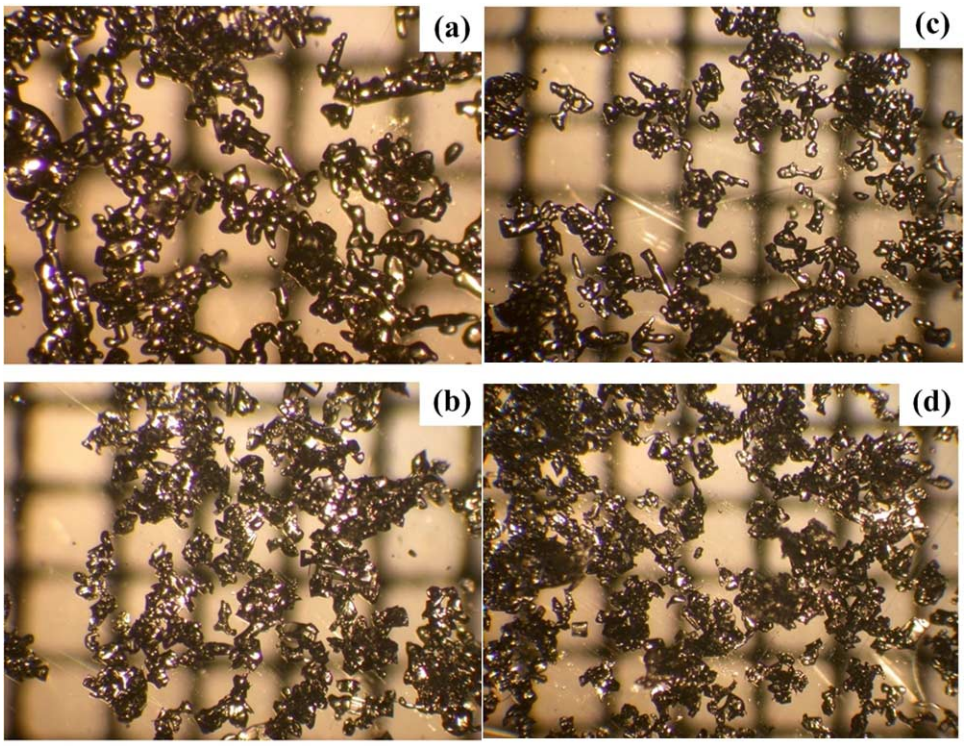

Figure 66. *Experiment #11 observed snow grains for (a) initial, (b) 3:00/surface, (c) 3:20/−0.5 cm, and (d) 6:00/surface (time=hr:min, grid scale=mm).*

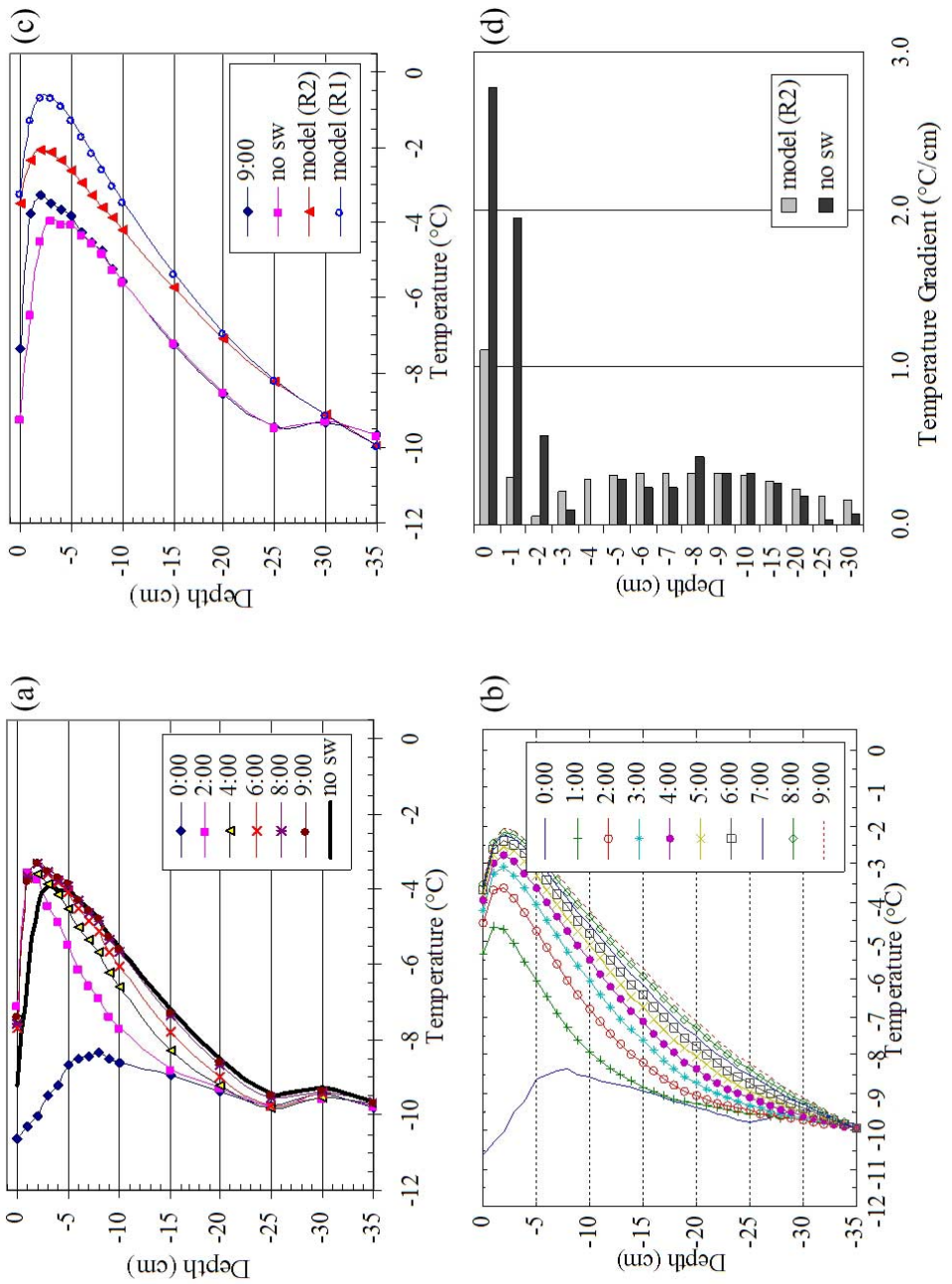

Figure 67. *Experiment #11 temperature profiles for the (a) experiment and (b) thermal model. Comparative model/experiment temperature plots of the (c) profiles and (d) gradients are shown for the last recorded measurement time. Model calculations in (b-d) used* $k_{eff} = 0.75\,W/m{\cdot}K$*. A model calculation in (c) is shown labeled as R1 and used* $k_{eff} = 0.44\,W/m{\cdot}K$*.*

Table 16. *Experiment #12 flux values for several near-surface layers at time 6:00. The column q''_g is the sum of the preceding four columns.*

Depth	Q_{SW}	Q_E	Q_H	Q_{LW}	q''_g	q''_{cond}
-9	0	–	–	–	0	-0.82
-8	0	–	–	–	0	-0.80
-7	0	–	–	–	0	-0.72
-6	0	–	–	–	0	-0.72
-5	0	–	–	–	0	-0.63
-4	0	–	–	–	0	-0.60
-3	0	–	–	–	0	-0.53
-2	0	–	–	–	0	-0.45
-1	0	–	–	–	0	-0.35
SFC	0	-3.33	27.22	-34.60	-10.72	10.91

Experiment #12

This experiment had the solar lamp turned off for the duration of the experiment in an attempt to prove the necessity of a solar input. $303\,kg/m^3$ density snow replaced $25\,cm$ from the previous experiment. Figures 68 shows observed grains, Figure 69 shows the experimental/model temperature profiles, and Table 16 lists the model fluxes. The model followed reasonably well compared to the experiment temperature profile as shown in Figure 69(a), but did predict a cooler surface than what occurred. While temperature gradients were above $10\,°C/m$ in the top layers (Figure 69(c)), the relatively cool temperature here hindered kinetic growth. As a result no facets were observed as shown in the grain pictures (Figure 68).

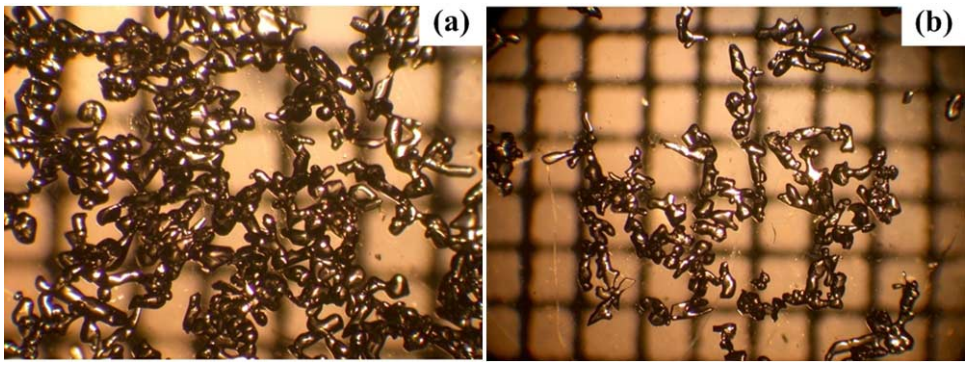

Figure 68. *Experiment #12 observed snow grains for (a) initial and (b) 6:00/surface (time=hr:min, grid scale=mm).*

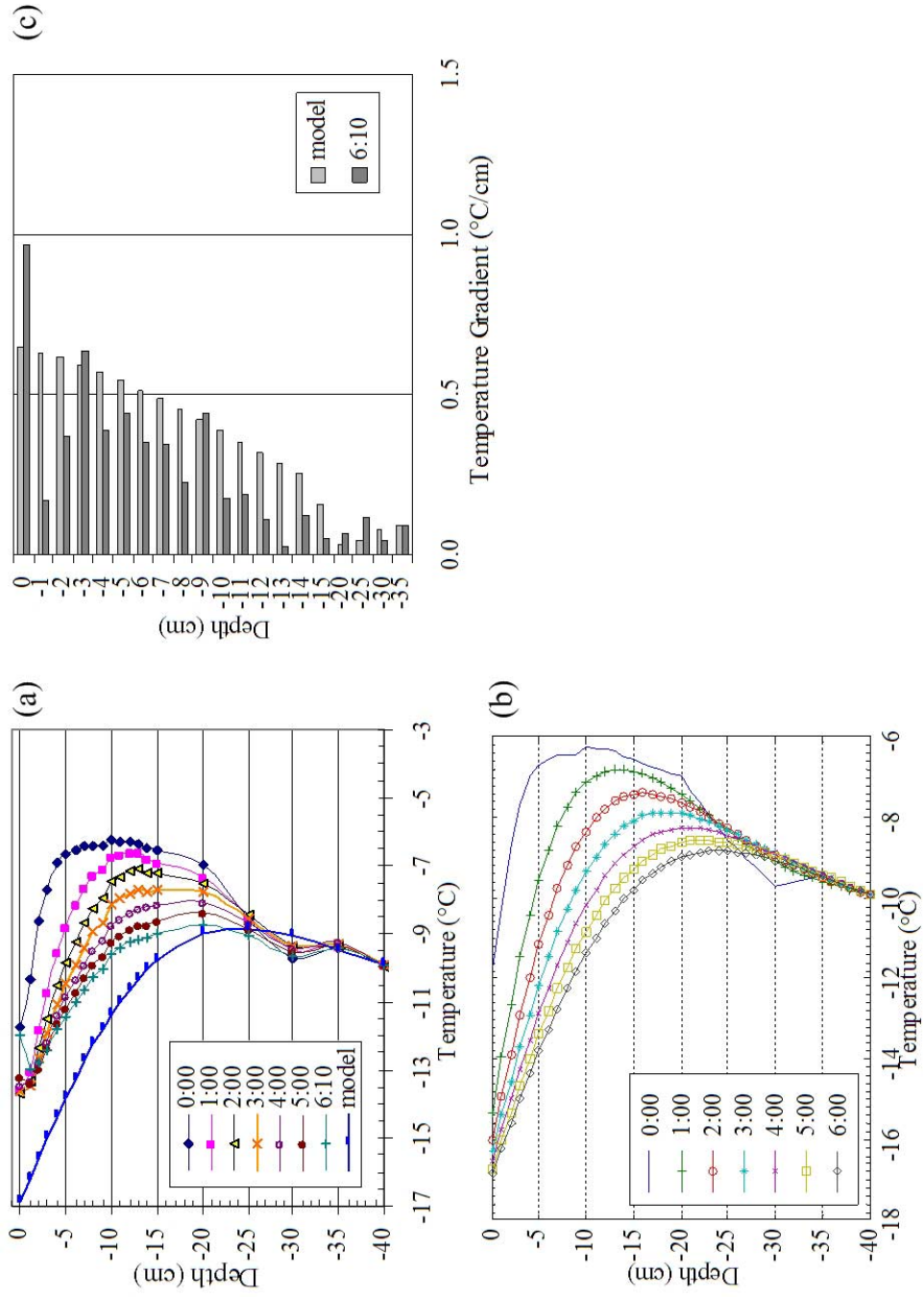

Figure 69. *Experiment #12 temperature profiles for the (a) experiment and (b) thermal model. Comparative model/experiment temperature plots of the (c) profiles and (d) gradients are shown for the last recorded measurement time.*

Table 17. *Experiment #13 flux values for several near-surface layers at time 6:00. The column q''_g is the sum of the preceding four columns.*

Depth	Q_{SW}	Q_E	Q_H	Q_{LW}	q''_g	q''_{cond}
-9	0.02	–	–	–	0.02	0.58
-8	0.06	–	–	–	0.06	0.47
-7	0.17	–	–	–	0.17	0.28
-6	0.47	–	–	–	0.47	-0.12
-5	1.27	–	–	–	1.27	-1.04
-4	3.45	–	–	–	3.45	-4.69
-3	9.37	–	–	–	9.37	-9.26
-2	25.46	–	–	–	25.46	0.00
-1	69.21	–	–	–	69.21	-68.29
SFC	71.03	-28.67	-28.89	-59.39	-45.91	44.74

Experiment #13

Experiment #13 was a continuation of experiment #12 where the solar lamp was simply turned on after #12 finished. The experimental settings produced facets at the 2:00 observation time that were approaching $1/2\,mm$ in grain size as shown in Figure 70. The density, measured at $300\,kg/m^3$, was relatively high yet still produced facets. Figure 71 shows the experimental/model temperature profiles. Model calculations showed good agreement as shown in (b-d).

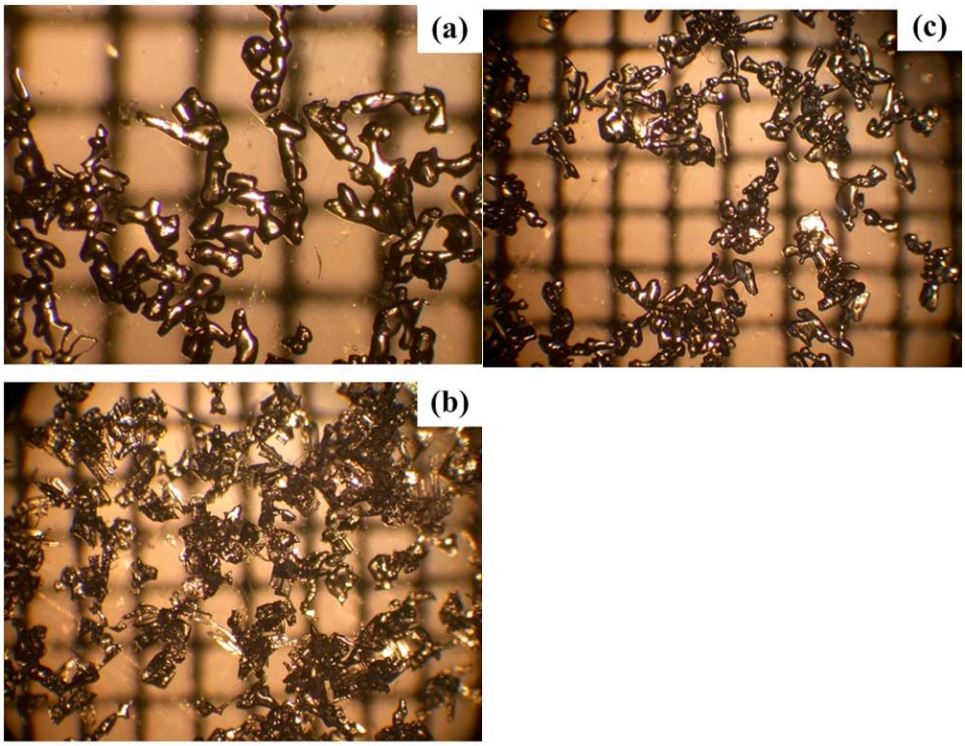

Figure 70. *Experiment #13 observed snow grains for (a) initial, (b) 2:00/surface, and (c) 2:00/below surface (time=hr:min, grid scale=mm).*

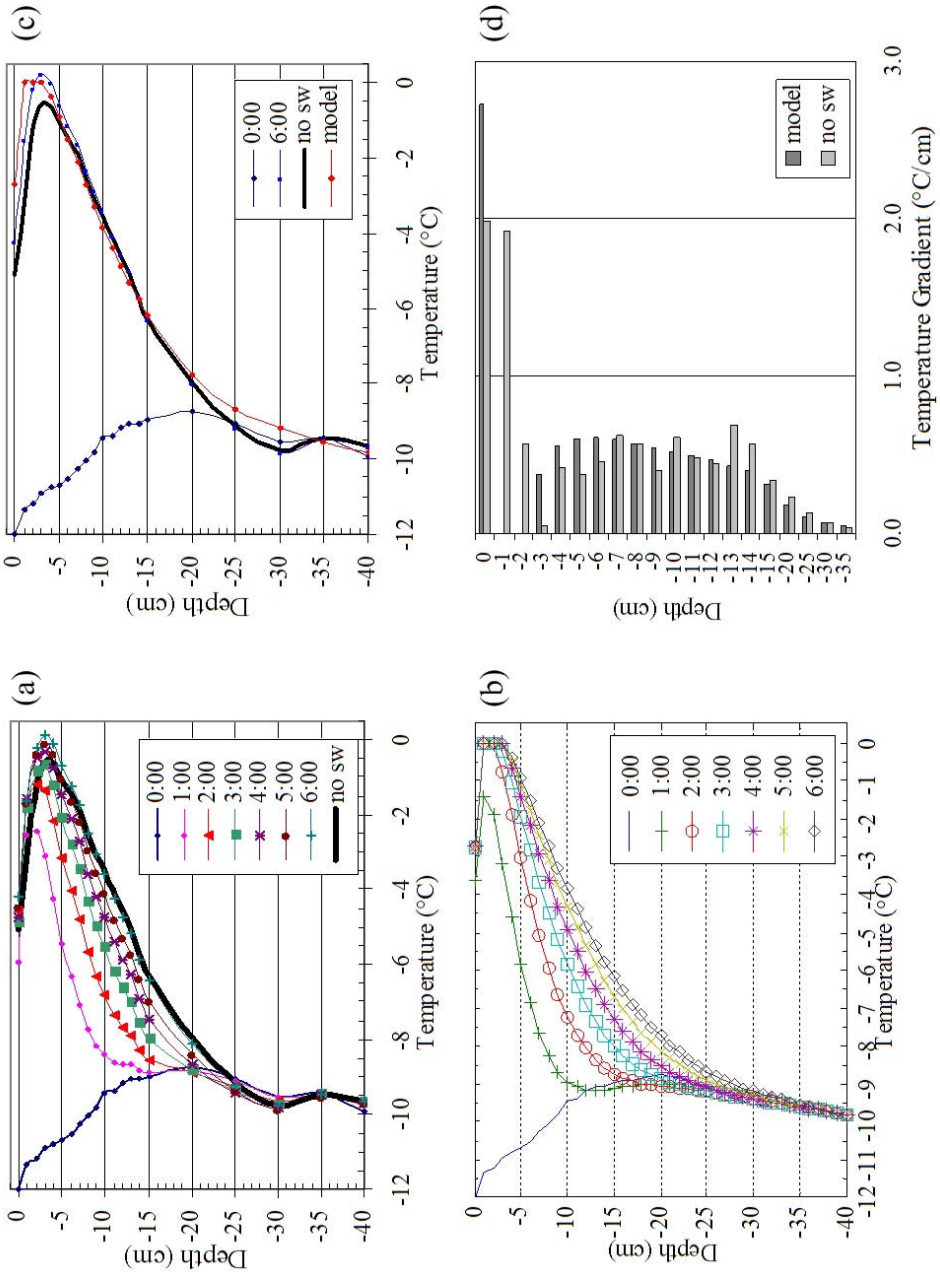

Figure 71. *Experiment #13 temperature profiles for the (a) experiment and (b) thermal model. Comparative model/experiment temperature plots of the (c) profiles and (d) gradients are shown for the last recorded measurement time.*

Experimental Summary

Upon performing the thirteen experiments some interesting observations were found regarding formation of near-surface facets. For example in experiment #1 no facets were found on the surface, which as discussed was most likely due to the fact that the snow used came from a $-24\,^{\circ}\mathrm{C}$ environment. This likely created vapor pressure gradients too low to drive kinetic metamorphism even though the temperature gradients at the surface were high. In experiment #2 the mean snowpack temperature was close to the chamber temperature and along with an increased shortwave setting and decreased density, these conditions created approximately $1\,mm$ facets near the surface. Experiment #12 showed that shortwave radiation is indeed necessary to form radiation-recrystallized facets. However, the amount of shortwave radiation appeared to have a lower limit indicated by experiment #8, which failed to produce facets for an incoming shortwave flux of $173\,W/m^2$.

The upper shortwave limit was investigated when the chamber shortwave setting was set to the maximum value as in experiment #4 for a value of $1140\,W/m^2$, which exceeds normal atmospheric radiation intensity. At this setting the snow a few centimeters below the surface started to form a melt-layer when as it was heated to $0\,^{\circ}\mathrm{C}$. The temperature gradient between this melt-layer and surface was high enough to produce some facets $0.5\,mm$ in size. This gradient magnitude was limited to the amount that the surface could be cooled primarily by longwave radiation exchange. With this high shortwave setting the actual incoming longwave radiation increased

due to emission from the lamp thus decreasing the amount of cooling possible due to the net longwave radiation exchange. If the snow surface was exposed to incoming longwave radiation present for a cold, clear sky the temperature gradient would have been larger. This would create optimal conditions for facet formation with a strong vapor pressure gradient established from the warm melt-layer to the cool surface.

Experiment #11 showed the effect of increasing the density to a relatively high value of $410\,kg/m^3$. With this increased density an increased effective thermal conductivity resulted, which hindered the ability of the snowpack to build-up heat. This experiment may be compared to #9 which had similar conditions and a density value of $257\,kg/m^3$. In #9 the subsurface temperature maximum reached $-1\,^{\circ}\mathrm{C}$ while the maximum for #11 reached three degrees cooler at a value of $-4\,^{\circ}\mathrm{C}$. Both experiments had similar temperature gradients near the surface, but in #9 the overall warmer temperatures created larger sized facets than #11. In this comparison the effect of increasing density shows the resulting effect in facet formation for some of the other major conditions held equal, including the shortwave and longwave radiation amounts.

Experiment #10 showed the effect of decreasing the incoming longwave radiation by setting the ceiling temperature to equal the chamber temperature. This effect actually caused heating of the snowpack due to the net longwave exchange being positive. This effect led to the formation of a melt-layer below the surface. When

compared to #9 where the net longwave radiation was cooling the surface, #10 was 1 °C warmer.

These experiments show agreement with previous research regarding radiation-recrystallized (RXT) near-surface facets. LaChapelle [1970] who coined this type of faceting, published a paper in 1970 where he discussed facet formation near the surface caused by a radiation balance between shortwave and longwave components. Birkeland et al. [1998] measured temperature gradients in the field where he observed high values in the near-surface layer occurring from shortwave heating. In Birkeland's paper, temperatures were measured with thermocouples, which experienced some level of solar-contamination although the amount was not known [Birkeland, 2004]. In Birkeland et al. [1998], the author was challenged as to whether the temperature increase was mainly due to solar-contamination of the thermocouples or if actual increases in snow temperature were occurring. From the preceding experiments it was shown that there is in fact an amount of solar-contamination present, which does give artificially high temperature measurement. However, the *no sw* data sets show that there was in fact significant temperature increases attributed to the snow actually warming. This dispels the notion that increased snow temperature was not only due to measurement error, but actually due solar absorption in the snow. Another occurrence that was discussed in prior papers was the presence of a melt-layer at depth caused by solar heating [Birkeland, 1998a; LaChapelle, 1970], which

was observed in several of the experiments. When the solar lamp was turned off these melt-layers froze into a melt-freeze crust.

The previous thirteen experiments showed many combinations of radiation balance, density, relative humidity, and snow type. Each experiment provided a discrete set of conditions in which the thermal model was used to perform temperature profile calculations. To attempt to isolate the causes leading to the formation of radiation-recrystallized near-surface facets, only one variable can be changed from one experiment to the next. If two or more variables are changing between experiments it is difficult to know what effect each has separately on facet formation. This was the case for the experiments in this thesis where it was difficult to selectively alter one variable. It may be possible to do so if all laboratory conditions can be precisely tuned, but then one still has to deal with the ever-changing nature of snow, which creates additional changes beyond the one intended. In the experiments when the intention was to only increase the snow density from a previous experiment, other variables such as a changing snow albedo and extinction coefficient would accompany the desired density increase. As a result, the number of unknowns could not be sufficiently scaled back as to find the effect of only variable influencing facet formation at a time.

This experimental short-coming alone emphasizes the need for a thermal model, which can reduce complexity by paring down the number of unknown variables to one. This one variable can then be altered over a wide range to determine how it

affects the formation of near-surface facets. In this way, the thermal model acts as an extrapolation tool investigating conditions not performed in the lab. However, before this extrapolation can be performed the model must show reasonable agreement with experimental results. The thirteen experiments provided the means to validate the thermal model for the thirteen combinations of chamber and snow conditions. After performing model calculations under these conditions it was shown that the model did provide good agreement to the measured temperature profiles. It is therefore reasonable to use the thermal model to analyze several "hypothetical" cases.

Hypothetical Model Calculations

Several hypothetical cases were tested using the thermal model as described in the following sections for calculations H1–H8. Tables 3 and 5 show the hypothetical conditions used in all of the cases.

H1

The intention in H1 was to observe the temperature profile occurring in new, low density snow ($130\,kg/m^3$) with a moderate amount of solar radiation ($500\,W/m^2$) and an incoming longwave radiation representative of a partly cloudy day ($240\,W/m^2$). Figure 72(a) shows the model's temperature profile for these conditions. The initial condition started out as an isothermal snowpack at $-10\,°\mathrm{C}$. Melt occurred for a $3\,cm$ thick layer below the surface. A sharp knee was observed, which creates a large

temperature gradient. Under these conditions faceting is expected to occur at the surface.

H2

This calculation assumed the same conditions as H1, but with a the solar zenith angle changed to 60°. Throughout all of the experiments the solar zenith angle was identical to 0° corresponding to the sun being directly overhead, which was the case of the solar lamp in relation to the snow surface. The effect of increasing the zenith angle was to increase the snow albedo, which in turn decreases the amount of solar radiation available to absorb in the snowpack. The increase in albedo in this calculation, H2, over H1 was only about 5%. However this increase contributed to about a 1 °C cooler temperature profile as shown in Figure 72(b).

H3

This hypothetical calculation was similar to H2 except that the incoming longwave radiation was reduced to $185\,W/m^2$, which corresponds to a day with a cold, clear sky [Plüss, 1997]. The result of this change is shown in Figure 72(c) where the temperature profile is about 3 °C cooler than calculation H2. An extremely large temperature gradient can be seen in the figure from a depth of $-2\,cm$ at −5 °C to the surface at −15 °C. H3 is cooler as a result of an increased net longwave radiation exchange due to a decreased incoming longwave radiation.

H4

H3 was repeated in this calculation with a higher shortwave radiation amount of $725\,W/m^2$. The result is shown in Figure 72(d) where the surface is still as cool as H3, but the subsurface is warmed to melt. The additional warmth creates an even larger temperature gradient than H3. Faceting would be expected to occur for this situation.

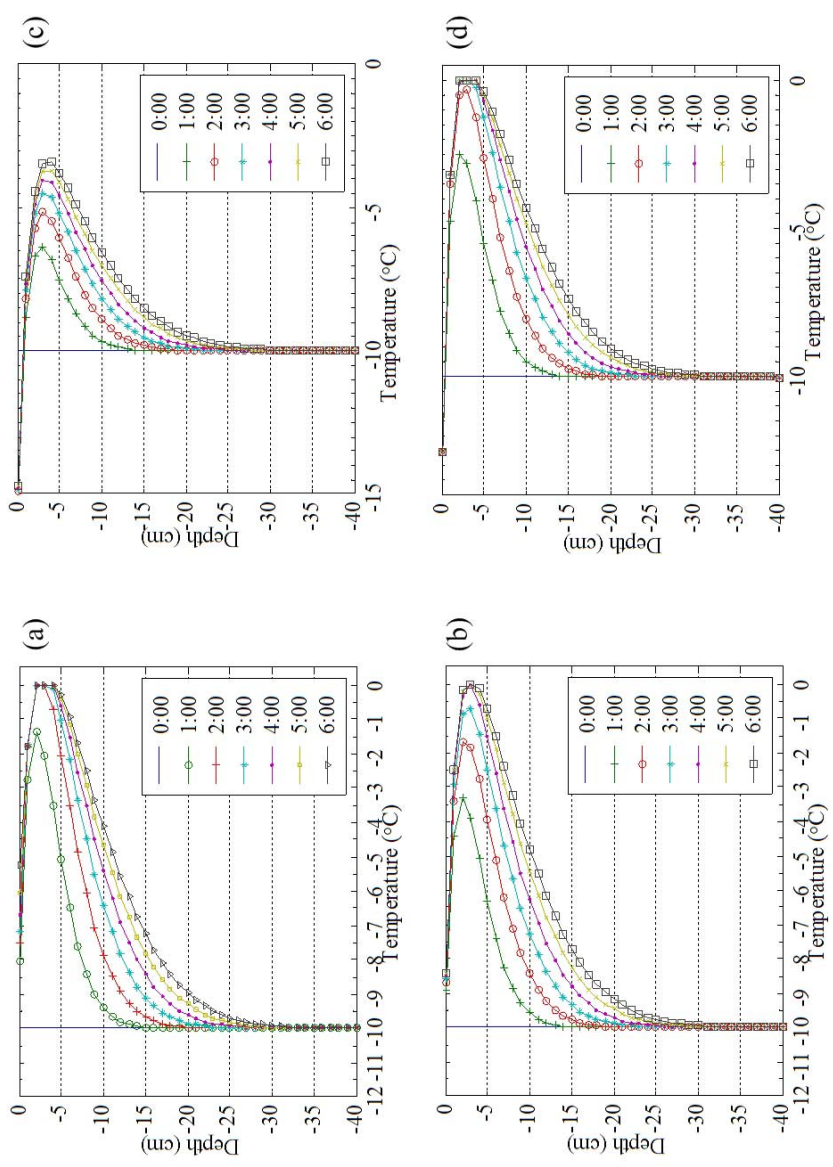

Figure 72. *Hypothetical model calculations for (a) H1, (b) H2, (c) H3, and (d) H4. H1, H2, and H3 have solar irradiance set at* $500\,W/m^2$*. H2-H4 have the same albedo value of 0.86, which is greater than H1 at 0.82. H1 and H2 have incoming longwave radiation values of* $240\,W/m^2$ *while H3 and H4 have* $185\,W/m^2$*. All calculations used a density value of* $130\,kg/m^3$*.*

H5–H8

The hypothetical calculations of H5, H6, H7, and H8 all included a one centimeter soot layer with the same concentration of $0.001\,ppmw$ as the samples used for the Hyperspectral albedo validation experiments (page 98). Calculations H5–H8 used the same atmospheric conditions as H4 as shown in Table 3 and similar snow properties as shown in Table 5. The placement of the soot layer from the snow surface was the only parameter changed from H5 through H8. The distances were 1, 2, 3, and $4\,cm$ below the surface for hypothetical runs H5, H6, H7, and H8, respectively. Geometrically speaking, H5 and H8 match experimental samples D1 and D3 from the albedo validation (see Figure 36). Changing the placement of this soot layer resulted in changes of the overall snowpack albedo. As the soot layer was placed deeper within the snowpack, the influence of this layer was minimized. When placed near the surface, the soot layer lowered the snowpack albedo when compared to an entirely clean sample without the soot layer. Figure 73 shows the four soot calculations. In part (a) (H5) of the figure, the snowpack is showing melt at a depth of $1\,cm$. Below this depth the snow is relatively cooler when compared to part (d) (H8). This is a result of the high extinction coefficient of the soot layer, which acts to absorb all shortwave radiation at this layer. No amount of shortwave absorption was detected below this layer indicating that no amount of heating due to shortwave radiation was occurring. Moving to part (b) (H6) where the soot layer was moved to a depth of $2\,cm$ below the surface the melting is occurring at the $2\,cm$ depth. Part (c) (H7) shows the soot

layer at $3\,cm$ and shows melting occurring both at the soot layer as well as in the overlying snow. Part (d) (H8) has the soot layer $4\,cm$ below the surface where its influence is starting to be undiscernible where H8 now closely resembles H4.

These hypothetical runs show that large temperature gradients can be established with the presence of dirty snow, which can act to greatly increase the gradient value. This has implications for facet formation whereby an increased gradient will likely result in an increased level of faceting. The preceding four hypothetical runs might simulate actual conditions where new low density snow could fall onto a dirty snow surface. The soot layer acts to absorb nearly all of the shortwave radiation reaching the soot layer depth, which concentrates the solar absorption to this layer. This concentration creates an effective heat source balanced by cooling effects at the snow surface thereby creating a temperature gradient.

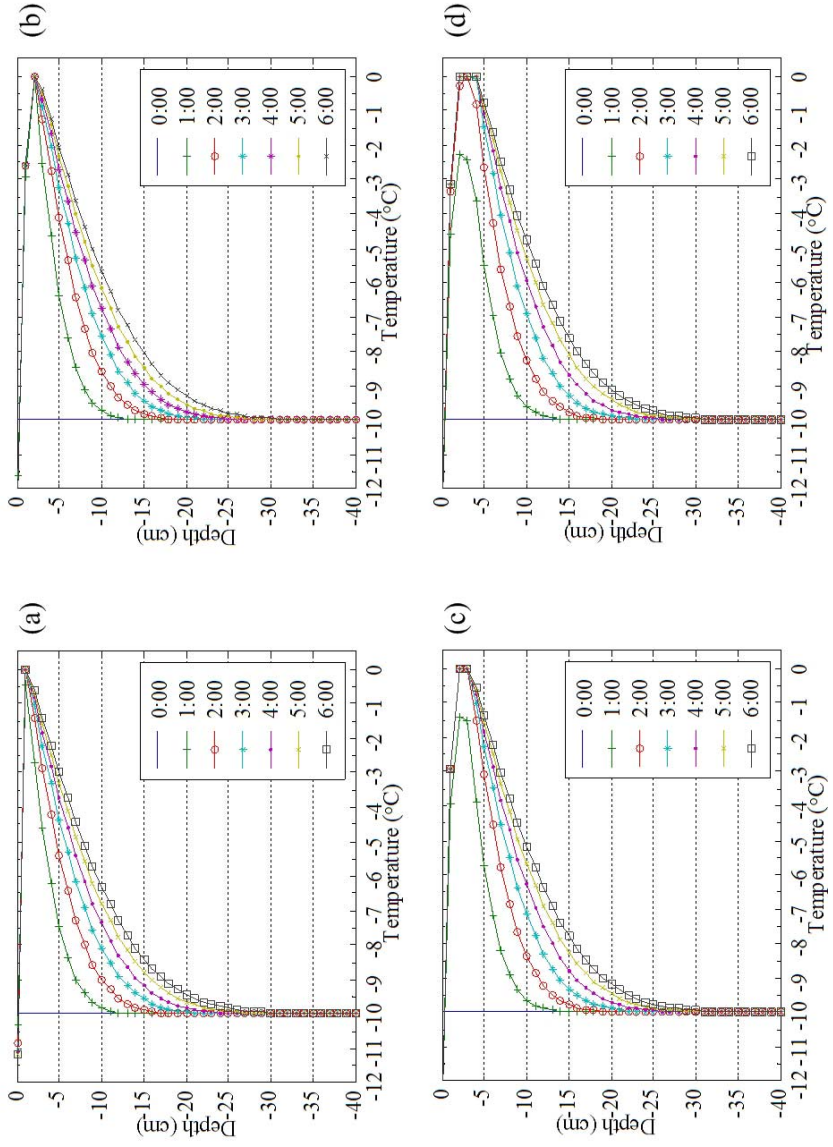

Figure 73. *Hypothetical model calculations for (a) H5, (b) H6, (c) H7, and (d) H8, which include soot layers placed at 1, 2, 3, and 4 cm below the surface, respectively.*

CHAPTER 5

CONCLUSIONS AND RECOMMENDATIONS

This study investigated the formation of near-surface facets in snow created by the radiation-recrystallization process. While these types of near-surface facets have been observed in the field setting, no prior work to the author's knowledge has been attempted to form these facets in a laboratory setting. The laboratory results are encouraging as several experiments performed in the environmental chamber developed a layer of facets near the surface. These successes back up prior papers discussing near-surface faceting including those of [Birkeland, 1998b] and [LaChapelle, 1970], which described the conditions necessary for facet formation.

From the experiments, the necessary conditions to form radiation-recrystallized facets can be summarized as following. The presence of shortwave radiation absorption in the top $10\,cm$ of the snowpack is required. Experiments with no shortwave absorption created no facets as expected. To create a temperature gradient the snow surface must be cooled by longwave radiation and/or turbulent energy exchange. If these cooling mechanisms were removed from the snow surface and the snow was exposed only to solar radiation, the surface would be the warmest part of the snowpack with diminishing warmth with depth. When the cooling mechanisms are present they act to *directly* counter the heating from the solar absorption at the surface. However, since longwave and turbulent exchange act at the surface they cannot directly affect

the snow at depth. Only an *indirect* interaction occurs via conduction, which does not cool as effectively as the *direct* interaction at the surface. As a result the surface of the pack is at a cooler temperature than the temperature at a few centimeters below the surface. This temperature difference was shown in most of the experiments and resembles a knee as discussed. These differences created high temperature gradients in the near-surface snow layers resulting in kinetic growth metamorphism leading to facet formation. It was observed that when density was over $300\,kg/m^3$ facet formation was nearly non-existent. For lower density snow, facets formed more readily showing agreement with field observations. The lower density snow was observed to be generally warmer at depth, which was due to the decreased thermal conductivity. Higher conductivity snow was relatively more efficient at conducting any absorbed heat away from a given point thus tending to lower temperature gradients. Experiments showed that the the radiation exchange and the snow density were significant factors to radiation-recrystallization facet formation.

The experimental study was supplemented with a developed thermal model that was used for each experiment. The experiments served to validate the model and create a tool that could be used to confidently extrapolate imposed snowpack conditions and snow-types. The model was compared to the thirteen experiments performed and proved to provide a good prediction of the snowpack temperature profile. The model solved a problem existing with any experimental study which is the problem of separating causes and effects. In this thesis, any attempt to change just one variable

from one experiment to the next was usually accompanied by an unintended change in another variable. Hypothetically applying the model allowed the influence of one variable on facet formation to be determined. The thermal model was adapted from previous research [Beddoe, 2001; Bristow, 2002] and modified and improved to work within this study. For example, the ability to extract extinction coefficients from the CAR albedo model was added, which gave good results. Another addition was the method of distributing the total absorbed shortwave radiation flux throughout the layers, which was not adequately done in the previous iterations of the thermal model [Bristow, 2002].

While some parts of the model were improved there exists some future refinements that may increase model accuracy. This includes studying the method used to determine shortwave radiation distribution and improving it by using extinction coefficients defined over a narrower spectral region. This thesis used an all-wave type approach for these coefficients, which fails to predict solar absorption well for some wavelengths. The trade-off in increasing spectral resolution is that the model would increase in complexity and computation time.

Future experimental refinements include studying the other two processes forming near-surface facets, that is the melt-layer recrystallization and diurnal recrystallization processes. These two processes could be easily implemented in the environmental chamber. Further experiments into different combinations of snow-type and imposed

conditions within the radiation-recrystallization process would also add to the understanding of this process. Also, obtaining snow-types not tested here would be beneficial to understanding the bounds of this process. This would include testing low density snow below $100\,kg/m^3$ and more cases with snow density above $300\,kg/m^3$.

The environmental chamber itself could be improved if resources were available to do so. One chamber function improvement would be upgrading the cooled ceiling with the capability to achieve even colder temperatures. This would decrease the amount of incoming longwave radiation to the snow surface and could increase the amount cooling at the snow surface. Currently, the ceiling is not able to reach incoming radiation values found on cold, clear days. A means to control chamber humidity would also be beneficial as tighter control over experimental conditions would be achieved. Currently, the chamber can only directly increase the humidity and cannot directly decrease humidity. Humidity is lowered in the room only when condensation occurs on the cooled ceiling panel.

REFERENCES CITED

REFERENCES CITED

Adams, E. and S. McDowell (1991). Thermal model for snow on three dimensional terrain. In *Japan-U.S. Workshop on Snow Avalanche, Landslide, Debris Flow Prediction and Control*.

Adams, E. E. and A. Sato (1993). Model for effective thermal conductivity of a dry snow cover composed of uniform ice spheres. *Annals of Glaciology 18*, 300–304.

Akitaya, E. (1974). Studies on depth hoar. *Contributions from the Institute of Low Temperature Sciences, Series A: Physical Sciences 26*, 1–67.

AMS (2004). Glossary of Meteorology. American Meteorological Society *http://amsglossary.allenpress.com*.

Anderson, E. (1976). A point energy and mass balance model of a snow cover. Technical Report NOAA/NWS 19, Office of Hydrology, National Weather Service, Silver Springs, MD.

Armstrong, R. (1985). *Metamorphism in a subfreezing, seasonal snowcover: The role of thermal and vapor pressure conditions*. Ph. D. thesis, University of Colorado.

Beckwith, T., R. Marangoni, and J. Lienhard (1993). *Mechanical Measurements* (5^{th} ed.). Addison-Wesley, Inc.

Beddoe, A. (2001). A spectrually integrated temporal albedo model. Master's thesis, Montana State University, Bozeman, MT.

Berger, R. H. (1979). Snowpack optical properties in the infrared. Technical Report 79-11, USA Cold Regions Research and Engineering Laboratory.

Birkeland, K. (1998a). Recycled powder and other types of near-surface faceting. *The Avalanche Review 17*(1).

Birkeland, K. (1998b). Terminology and predominant processes associated with the formation of weak layers of near-surface faceted crystals in the mountain snowpack. *Arctic and Alpine Research 30*(2), 193–199.

Birkeland, K. (2004). Personal communication, June 23, 2004.

Birkeland, K., R. Johnson, and D. Schmidt (1998). Near-surface faceted crystals formed by diurnal recrystallization: A case study of weak layer formation in the mountain snowpack and its contribution to snow avalanches. *Arctic and Alpine Research 30*(2), 200–204.

Bohren, C. and B. Barkstrom (1974). Theory of the optical properties of snow. *Journal of Geophysical Research 79*(30), 4527–4535.

Brandt, R. and S. Warren (1993). Solar-heating rates and temperature profiles in Antarctic snow and ice. *Journal of Glaciology 39*(131), 99–110.

Bristow, J. (2002). The development and validation of a snow/icepack pavement temperature thermodynamic model. Master's thesis, Montana State University, Bozeman, MT.

Brun, E., E. Martin, V. Simon, C. Gendre, and C. Coleou (1989). An energy and mass model of snow cover suitable for operational avalanche forecasting. *Journal of Glaciology 35*(121).

Chapra, S. and R. Canale (1998). *Numerical Methods for Engineers* (3^{rd} ed.). McGraw-Hill.

CIE (1989). Solar spectral irradiance. Technical Report 85, International Commission of Illumination, *http://www.cie.co.at/publ/abst/85-89.html*.

Colbeck, S. (1980). Thermodynamics of snow metamorphism due to variations in curvature. *Journal of Glaciology 26*.

Colbeck, S. (1982). Growth of faceted crystals in a snow cover. Technical Report CRREL 82-29, USA Cold Regions Research and Engineering Laboratory.

Colbeck, S. (1983). Theory of metamorphism of dry snow. *Journal of Geophysical Research 88*(C9), 5475–5482.

Colbeck, S. (1997). A review of sintering in seasonal snow. Technical Report CRREL 97-10, USA Cold Regions Research and Engineering Laboratory.

Colbeck, S., E. Akitaya, R. Armstrong, H. Gubler, J.Lafeuille, K.Lied, D. McClung, and E. Morris (1990). The international classification for seasonal snow on the ground. *The International Commission on Snow and Ice of the International Association of Scientific Hydrology*.

Colbeck, S. and J. Jamieson (2001). The formation of faceted layers above crusts. *Cold Regions Science and Technology 33*, 247–252.

Dozier, J. and S. Warren (1982). Effect of viewing angle on the infrared brightness temperature of snow. *Water Resources Research 18*, 1424–1434.

Eppley Laboratories, Inc. (2001). Instructions for the Precision Infrared Radiometer (Model PIR). *http://www.eppleylab.com*.

Fierz, C. (1998). Field observations and modelling of weak-layer evolution. *Annals of Glaciology 26*, 7–13.

Fukuzawa, T. and E. Akitaya (1993). Depth-hoar crystal growth in the surface layer under high temperature gradient. *Annals of Glaciology 18*, 39–45.

Gray, D. and D. Male (1981). *Handbook of Snow*. Pergamon Press Canada.

Grenfell, T. and G. Maykut (1977). The optical properties of ice and snow in the Arctic Basin. *Journal of Glaciology 18*(80), 445–463.

Incropera, F. and D. Dewitt (1996). *Introduction to Heat Transfer* (3^{rd} ed.). John Wiley & Sons.

Iqbal, M. (1983). *An Introduction to Solar Radiation*. Academic Press.

Ishikawa, N., N. Hideki, and Y. Kajiya (1999). Contributions of heat from traffic vehicles to snow melting on roads. *Transportation Research Record* (1672). National Research Council, Washington, D.C.

Jamieson, J. (2000). Snow avalanche hazards and management in Canada: Progress and challenges. In *53rd Canadian Geotechnical Conference, Workshop on Geotechnique and Natural Hazards*.

Jamieson, J. and C. Johnston (1992). Snowpack characteristics associated with avalanche accidents. *Canadian Geotechnical Journal 29*, 862–866.

Jamieson, J. and A. van Herwijnen (2002). Preliminary results from controlled experiments on the growth of faceted crystals above a wet snow layer. In *Proceedings of the 2002 International Snow Science Workshop*.

Jordan, R. (1991). A one-dimensional temperature model for a snow cover. Technical Report Special Report 91-16, USA Cold Regions Research and Engineering Laboratory.

Kakaç, S. and Y. Yener (1993). *Heat Conduction* (3^{rd} ed.). Taylor & Francis.

Kerlin, T. W. (1999). *Practical Thermocouple Thermometry*. Research Triangle Park, NC: Instrument Society of America.

KHS (2001). *Technical Lighting Systems*. K.H. Steuemagel.

Kirchner, H., G. Michot, and J.Schweizer (2002). Fracture toughness of snow in shear and tension. *Scripta Materialia 46*, 425–429.

Kopka, H. and P. Daly (2004). *Guide to LaTeX* (4^{th} ed.). Addison-Wesley Professional.

LaChapelle, E. (1970). Principles of avalanche forecasting. In *Ice Engineering and Avalanche Forecasting and Control*, Number 98 (Technical Memorandum) in Technical Memorandum, National Research Council, Canada, pp. 106–113.

Male, D. and R. Granger (1981). Snow surface energy exchange. *Water Resources Research 17*(3), 609–627.

Marbouty, D. (1980). An experimental study of temperature-gradient metamorphism. *Journal of Glaciology 26*(94), 303–312.

Marks, D. (1988). *Climate, energy exchange, and snowmelt in Emerald Lake watershed, Sierra Nevada*. Ph. D. thesis, University of California Santa Barbara.

Marshall, S. (1989). *A physical parameterization of snow albedo for use in climate models*. Ph. D. thesis, University of Colorado.

Martin, E. and Y. Lejeune (1998). Turbulent fluxes above the snow surface. *Annals of Glaciology 26*, 179–183.

McClung, D. and P. Schaerer (1993). *The Avalanche Handbook* (6^{th} ed.). Seattle. The Mountaineers Books.

Moran, M. and H. Shapiro (2004). *Fundamentals of Engineering Thermodynamics* (5^{th} ed.). John Wiley & Sons, Inc.

Omega Engineering Inc. (2003). *The Temperature Handbook* (5^{th} ed.), Volume MMV. *http://www.omega.com*.

Özisik, M. (1994). *Finite Difference Methods in Heat Transfer* (2^{nd} ed.). CRC Press.

Patankar, S. (1980). *Numerical Heat Transfer and Fluid Flow*. New York: Hemisphere Publishing.

Plüss, C. (1997). The energy balance over an alpine snowcover. *Zürcher Geographische Schriften Heft 65*.

Resonon, Inc. (2004). *http://www.resonon.com*. Bozeman, MT.

Stull, R. (1988). *An Introduction to Boundary Layer Meteorology*. Kluwer Academic Publishers.

Sturm, M., J. Holmgren, M. Knig, and K. Morris (1997). The thermal conductivity of seasonal snow. *Journal of Glaciology 43*(143), 26–41.

Tremper, B. (2001). *Staying Alive in Avalanche Terrain*. Seattle: The Mountaineers Books.

Warren, S. (1982). Optical properties of snow. *Reviews of Geophysics and Space Physics 20*(1), 67–89.

Warren, S. (1984). Impurities in snow: Effects on albedo and snowmelt (review). *Annals of Glaciology 5*, 177–179.

Warren, S. and W. Wiscombe (1980a). A model for the spectral albedo of snow. I: Pure snow. *Journal of the Atmospheric Sciences 37*, 2712–2733.

Warren, S. and W. Wiscombe (1980b). A model for the spectral albedo of snow. II: Snow containing atmospheric aerosols. *Journal of the Atmospheric Sciences 37*, 2734–2745.

Yosida, Z. (1960). Internal melting of snow due to the penetrating sunlight. *Contributions from the Institute of Low Temperature Sciences, Series A: Physical Sciences*, 97–111.

APPENDICES

APPENDIX A

THERMAL MODEL MATLAB CODE

```
function [Temp_holdall, TG, flux_hold, Q_hold, k_eff, k_all] = MAIN;

%-----MAIN - Temperature Profile Program
%   Blake Morstad / 2003-2004
%
%   The MAIN program initializes and controls
%   the solution procedure involving
%   the energy balance routine.
%
%*********Functions called in MAIN*************************************************
%
% FILE_READ_MET_DATA - Reads a weather input text file
% TEMP_CONTROL - Controls layer temperatures for melting (holds at 0*C)
% HEAT_TRANSFER - Calculates energy fluxes for the layers
% TEMP_PROFILE - Crank-Nicolson solution method for temperature profile
% NOTES:  - add paths in Matlab to include CAR and NSF folders (setpath)
%
%*****************************************************************************
% INPUTS: Meteorological data, user defined data
% OUTPUTS: Results of energy balance analysis
%*****************************************************************************
clear; clc;
%-----Start of User-Defined Input-----------------------------------------------
    %-----Define Variables

    dtmin = 15;                 % time step (minutes) based on INPUT
    dtint = 4;                  % time interval (used to add stepped data to INPUT)
    dt = (dtmin*60)/(dtint+1);   % time step (units needed in sec.)used in:TEMP_PROFILE
    dy = 0.01;         % snow layer thickness (m)
    n_l = 40;          % number of snow layers
    albc = 0.8;        % albedo of underlying surface (SHORT_RAD fxn)
%--->
%%EXP#1 inputs

    Tavg = -9.8;       % (C) Used to calculate specific heat
    Tbottom = -9;   % (C) Bottom boundary condition
    albtop = .75;     % albedo of the snow surface computed from CAR (allwave value)
    N = 20;            % specify that every Nth iteration plotted (hourly=20)
    met_file = 'metdata_exp1.txt';     % specify meteorological input file string
    IC_file = 'tempdata_exp1.txt';     % specify initial temperature inpute file string
    graph_title = 'Experiment #1 Model Temperature Profile';     % plot title

    %-----Define Snow Layer Properties
        for i = 1:40
            layers(i,1) = 195;      %density
            layers(i,2) = 65; end   %kappa
        for i = 1:n_l
            layers(i,3) = (2.115 + 0.00779*Tavg)*1000;      % specific heat (J/kg*K)
            layers(i,4) = .021 + 2.5*(layers(i,1)*.001)^2;  % thermal conductivity (W/m*K)
            %layers(i,4) = 0.2;
        end
%--->
        k_eff = layers(30:40,4);    % thermal cond.
        k_all = layers(:,4);
        % NOTES:
        % i=1 => bottom layer (node 1) /// i=n_l => top layer (node n_l+1)
        % Snow layers array: [Density (kg/m^3), Extinction Coeff. (1/m),...
        %                     Specific Heat (J/kg*K), Thermal Conductivity (W/m*K)]
%-----End of User Defined Input-------------------------------------------------
%-------------------------------------------------------------------------------------
%-----Read the Meteorological Inputs
    % INPUT = [Wind Speed(m/s), Air Temperature(C), Barometric Pressure(mbar),...
    %          Relative Humidity(%), Solar Radiation(W/m^2), Incoming Longwave (W/m^2)]
    [INPUT] = met_data(met_file, dtint);    % input from a text file
    [metrows, metcolumns] = size(INPUT);    % used to determine number of iterations
%-----Steady State Temperature Profile
```

```
        %-----Constant Initial Temperature Profile:
            %for i = 1:n_l+1         % i = node index
            %  Temp(i,1) = Tbottom;    % assume I.C. at plate temperature
            %end
            %Temp_initial(:,1) = initial_temp(IC_file);
        %-----User-defined Temeperature Profile:
            myfile = fopen(IC_file, 'r'); T = fscanf(myfile, '%g', [1 inf]);
            fclose(myfile); Temp(:,1) = T';
            Temp_initial(:,1) = Temp(:,1);

%-----End of Model Input--------------------------------------------------------------------
%------------------------------------------------------------------------------------------
%-----Begin Iterative Calculations----------------------------------------------------------
    z = 1;  % column indicator for storing data
    Qsw = 0;
    %-----Loop through data
    for i = 1:metrows   % i=loop index / # INPUT rows determines # loops

        %-----Call HEAT_TRANSFER Energy Function
        [flux, Q, Qsw] = heat_transfer(INPUT, Temp, albtop, albc, i, n_l, dy, layers, Qsw);
                         % i in the above call is the row of INPUT considered

        %-----Call TEMP_PROFILE to Calculate New Temperature Profile
        Temp = temp_profile(Temp, n_l, dy, dt, layers, flux, Tbottom);
        Temp = temp_control(Temp, n_l)

    %-----Save every Nth array to plot
        for k = N:N:metrows
            if i == k
                Temp_hold(:,z) = Temp;
                flux_hold(:,z) = flux;
                Q_hold(:,:,z) = Q;
                z = z + 1;
            end
        end
    end
%-----END of Iterative Calculations---------------------------------------------------------
%------------------------------------------------------------------------------------------
% Combine the initial and temporal temperature arrays:
Temp_holdall = [Temp_initial Temp_hold];    % Horizontally Concatenate Matrices

% Calculate temperature gradients between each node for every Nth time step:
TG = diff(Temp_holdall,1,1)./dy;        %(*C/m)

%------Plot Results
Y = [0:dy:n_l*dy];          % Vector of nodes
        plot(Temp_holdall(:,:),Y)
        %title(graph_title,'FontName','Times New Roman','FontSize',14)
        xlabel('Temperature (\circC)','FontName','Times New Roman','FontSize',14)
        ylabel('Depth (cm)','FontName','Times New Roman','FontSize',14)
        set(gca,'YGrid','on')
        xlim([-12 0.5])
        set(gca,'xtick',[-12 -11 -10 -9 -8 -7 -6 -5 -4 -3 -2 -1 0 1])
        set(gca,'xminortick','on')
        set(gca,'YTickLabel',{'-40';'-35';'-30';'-25';'-20';'-15';'-10';'-5';'0'})
        set(gca,'FontName','Times New Roman','FontSize',14)
        legend('0:00','1:00','2:00','3:00','4:00',4)
%-----END of MAIN---------------------------------------------------------------------
%-------------------------------------------------------------------------------------

function [M] = met_data(file, dtint)
%
%   This function reads a text file deliminated
%   by tabs and writes it to a matrix.  It also
%   adds input lines between time steps to allow for
%   a smaller dt.
```

```
%
%**********INPUT VARIABLES*********************************************
%   file = file name writen as 'file name.txt'
%   >>dtmin = time step in minutes >>(only use to interpolate)
%   dtint = time step intervals between input points
%
%**********OUTPUT VARIABLE*********************************************
%   M = m x n matix of input data
%**************************************************************************

%  >>Read file
myfile = fopen(file, 'r');
M = fscanf(myfile, '%g  %g  %g  %g  %g  %g', [6 inf]);
fclose(myfile); M = M';

%  >>Add constant steps to input
[m,n] = size(M); Mdata(1,:) = M(1,:);
for i = 1:dtint             %1st loop to create one copy of data
    Mdata(i+1,:) = M(1,:);
end
for j = 2:m                 %2nd loop creates copies of remaining data
    for k = 1:dtint
        Mdata2(k,:) = M(j,:);
    end
    Mdata = [Mdata; Mdata2; M(j,:)];    %concatenate created steps
end
%Mdata = [Mdata; M(m,:)];    %adds one last line to end on even time
M = Mdata;

% >>NOTES:  Consider the example: if dtint=4 and dtmin=15
% (MET data measured every 15 minutes from cold room or field data)
% then 4 (dtint) additional lines will be added to each line from the original
% metdata.txt data.  This combination will provide for a time step of 3
% minutes (dt).

function [flux, Q, Qsw] = heat_transfer(INPUT, Temp, albtop, albc, j, n_l,
dy, layers, Qsw)

%   This function calculates the fluxes due to
%   convection, longwave radiation, evaporation,
%   and calls the function which distributes the
%   shortwave radiation into fluxes for each layer.
%***********************Functions called in HEAT_TRANSFER************************
%
% VAPOR_PRESSURE - Calculates saturation vapor pressure
% SHORT_RAD - Determines the amount of radiation generation in each layer
%
%*******************************************************************************
%**********OUTPUT VARIABLES*****************************************************
%   flux = Heat flux that is absorbed at each layer (W/m^2)
%
%   Where flux is the sum of 4 components
%       Qe = Latent heat flux (evaporation)
%       Qh = Sensible heat flux (convection)
%       Qlw = Long-wave radiation heat flux
%       Qsw = Short-wave radiation heat flux
%
%**********INPUT VARIABLES******************************************************
%   INPUT column 1 = wind speed (m/s)
%   INPUT column 2 = air temperature (C)
%   INPUT column 3 = barometric pressure (mbar)
%   INPUT column 4 = relative humdity (%)
%   INPUT column 5 = solar radiation (W/m^2)
%   INPUT column 6 = incoming longwave radiation (W/m^2)
%   layers column 1 = density (kg/m^3)
%   layers column 2 = extinction coefficient (kappa) (1/m)
```

```
%   albtop = top surface albedo (%)
%   albc = albedo of the underlying surface (%)
%   Temp = temperature profile (C)...stores all layer temperatures
%   dt = time step (seconds)
%   j = row indicator variable to determine which line of INPUT to use
%   n_l = number of snow layers
%   dy = layer thickness
%*****************************************************************************

%%%%%%%%%%%%%%%%%%%%%%%%
%%  Define Variables   %%
%%%%%%%%%%%%%%%%%%%%%%%%

%   Initialize Local Variables

    Vw = INPUT(j,1);                % Wind Speed
    Tair = INPUT(j,2);              % Air Temperature
    Pa = INPUT(j,3);                % Barometric Pressure
    R_H = INPUT(j,4);               % Relative Humidity
    Qsw_in = INPUT(j,5);            % Incoming Solar Radition
    Qlw_in = INPUT(j,6);            % Incoming Longwave Radiation
    dens = layers(:,1);             % Snow Layer Density (kg/m^2)
    kappa = layers(:,2);            % Extinction Coefficient
    e_snow = 0.9875;                % Average Snow Emissivity [Dozier and Warren]
    s_b = 5.6696*10^(-8);           % Stefan-Boltzmann constant (W/m^2*K^4)
    R = .287;                       % Gas constant for air  (kJ/kg*K)

    % For Turbulent Heat Transfer
    Kh = .0023;   % Dimensionless transfer coeff. for heat
    Ke = .0023;   % Dimensionless transfer coeff. for water vapor
    Lsub = 2833;  % Latent heat of sublimation (kJ/kg)

    % Piecewise Cubic Hermite Interpolation for Heat Capacity
    Cpd = [1003, 1003, 1005, 1008];  % Heat Capacity of Air(J/kg*K)
    Tr = [200, 250, 300, 350];       % Reference Temp for curve fit (K)
    Cp = interp1(Tr,Cpd,Tair+273.15,'pchip');

    % Barometric Pressure (kPa) this is divided by 10 because it is changing
    % from mbars to kPa
    Pa = Pa/10;

    % Air Density (kg/m^3) (Ideal Gas Law):
    air_p = Pa/( R*(Tair+273) );

    % e_a = water vapor pressure of air:
        e_a = vapor_pressure(Lsub, Tair, -5, .402);
        % Account for the relative humidity of the air [Martin, 1998]
            e_a = e_a*R_H/100;              % (divide by 100 for fraction)
    % e_s = water vapor pressure of snow surface:
        e_s = vapor_pressure(Lsub, Temp(n_l+1,1), -5, .402); % solid - vapor (kPa)

%%%%%%%%%%%%%%%%%%%%%%%%%%%%%%%%%%%%%%%%%%%%%%%%%%%%%%%%%%%%%%%%%%%%%%%%%%%%
%%   Net Longwave Radiation (LW_in - LW_out)   %%
%%%%%%%%%%%%%%%%%%%%%%%%%%%%%%%%%%%%%%%%%%%%%%%%%%%%%%%%%%%%%%%%%%%%%%%%%%%%

    Qlw(n_l,1) = Qlw_in - e_snow*s_b*(Temp(n_l+1,1) + 273.15)^4 ;

%%%%%%%%%%%%%%%%%%%%%%%%%%%%%%%%%%%%%%%%%%%%%%%%%%%%%%%%%%%%%%%%%%%%%%%%%%%%
%% Sensible (Convective) Heat Flux %%
%%%%%%%%%%%%%%%%%%%%%%%%%%%%%%%%%%%%%%%%%%%%%%%%%%%%%%%%%%%%%%%%%%%%%%%%%%%%

    Qh(n_l,1) = air_p*Cp*Kh*Vw*(Tair - Temp(n_l+1,1));

%%%%%%%%%%%%%%%%%%%%%%%%%%%%%%%%%%%%%%%%%%%%%%%%%%%%%%%%%%%%%%%%%%%%%%%%%%%%
%% Latent Heat (Evaporation - Sublimation) Flux %%
%%%%%%%%%%%%%%%%%%%%%%%%%%%%%%%%%%%%%%%%%%%%%%%%%%%%%%%%%%%%%%%%%%%%%%%%%%%%
```

```
    Qe(n_l,1) = 0.622*air_p*Lsub*Ke*Vw*(e_a - e_s)*1000/Pa;

%%%%%%%%%%%%%%%%%%%%%%%%%%%%%%%%%%%%%%%%%%%%%%%%%%%%%%%%%%%%
%% Call the Shortwave Radiation Distribution Function %%
%%%%%%%%%%%%%%%%%%%%%%%%%%%%%%%%%%%%%%%%%%%%%%%%%%%%%%%%%%%%

    if j == 1, Qsw = short_rad(kappa, albtop, albc, Qsw_in, n_l, dy, dens); end

%%%%%%%%%%%%%%%%%%%%%%%%%%%%%%%%
%% Constructing the Flux Matrix %%
%%%%%%%%%%%%%%%%%%%%%%%%%%%%%%%%

    Q = [Qsw Qe Qh Qlw];

%%%%%%%%%%%%%%%%%%%%%%%%%%%%%%%
%% Sum fluxes for each layer %%
%%%%%%%%%%%%%%%%%%%%%%%%%%%%%%%

flux = sum(Q')';  %column array [bottom snow; ... ; top snow]

% NOTES:
% -n_l = top snow layer / n_l+1 = top snow node
% -Qh, Qe, Qlw only apply to top (surface) layer of snow

function [Pv] = vapor_pressure(L, T, To, Po)
%
%   This function calculates the water vapor pressure
%   (kPa) from the Clausius-Clapeyron Eqn.
%   Assumptions:    - Air is an Ideal Gas
%                   - Small temperature changes Le is ~ constant
%
%**********OUTPUT VARIABLES***************************************************
%       Pv = Saturation vapor pressure  (kPa)
%
%**********INPUT VARIABLES****************************************************
%       L  = Latent heat of transformation  (kJ/kg)
%       T  = Temperature of interest  (C)
%       To = Reference temperature  (C)
%       Po = Reference pressure  (kPa)
%*********************************************************************

R = .462;    % Gas constant for water vapor (kJ/kg*K)

%   Convert Temperatures to Kelvin
To = To + 273.15; T = T + 273.15;

%   Calculate saturated vapor pressure
Pv = Po*exp((L/R)*(1/To - 1/T));

%   Water: Solid-vapor Saturation near -5 C
%Le = 2836.2 kJ/kg;
%To = -5; % degree C
%Po = 0.402 kPa;

function [Qsw] = short_rad(kappa, albtop, albsub, Qsw_in, n_l, z, dens)
%
%   This function calculates the absorbed shortwave
%   radiation distribution throughout the snow pack.
%
%**********INPUTS*************************************************************
%   kappa  = extinction coefficient of each layer (1/m)
%   albtop = albedo of top layer computed from CAR
%   albsub = albedo of substrate surface
%   Qsw_in = incoming shortwave radiation at the surface (W/m^2)
%   n_l    = number of snow layers
```

```
%   z      = snow layer thickness used in Bouger's equation
%
%**********OUTPUTS*********************************************************
%   Qsw = Absorbed shortwave radiation (W/m^2) in each layer
%*****************************************************************************

%****NOTES:
%   It = Amount of radiation that is transmitted into a layer
%   Ia = Amount of radiation absorbed in the layer (Ia = It - It exp(-k*z))

% COMPUTE DISTRIBUTION OF ABSORBED RADIATION WITHIN THE SNOWPACK:
    % TOP LAYER:

It(n_l,1) = Qsw_in*(1-albtop);     % Total amount available for absorption
%Ia(n_l,1) = It(n_l,1)*(1 - exp(-kappa(n_l)*(z/2)*(dens(n_l)/1000)));
Ia(n_l,1) = It(n_l,1)*(1 - exp(-kappa(n_l)*(z/2)));
Qsum = sum(Ia(:,1));                  % Running sum variable

% INTERMEDIATE LAYERS:
for i = 1:n_l-1
    It(n_l-i,1) = It(n_l,1) - Qsum;
    %Ia(n_l-i,1) = It(n_l-i,1) - It(n_l-i,1)*exp( -kappa(n_l-i)*z*(dens(n_l-i)/1000) );
    Ia(n_l-i,1) = It(n_l-i,1) - It(n_l-i,1)*exp( -kappa(n_l-i)*z );
    Qsum = sum(Ia(:,1));
end

Qsw = Ia;

% NOTES:
% -returns a column array:
%   Qsw = [   Q(bottom snow)
%             ...
%             Q(top snow)    ]

function [Temp] = temp_profile(Temp, n_l, dy, dt, layers, flux, Tbottom)
%
%   This function calculates the new temperature
%   profile from the bottom to the top layer.
%   Solving the heat tranfer differential equation
%   taking into acount for conduction, and other
%   heat fluxes.  The Crank-Nicolson method
%   is used to solve the differential equation:
%   (p*Cp*dT/dt = k*d^2T/dy^2 + qin/dy)
%
%**********OUTPUT VARIABLES***********************************************
%       Temp = The new or updated temperature profile (C)
%
%**********INPUT VARIABLES************************************************
%       Temp = previous temperature profile
%       n_l = number of snow layers
%       dy = layer thickness (m)
%       dt = timestep (s)
%       layers column 1 = density (kg/m^3)
%       layers column 3 = specific heat (J/kg K)
%       layers column 4 = thermal conductivity (W/m K)
%       flux = amount of energy flux terms being absorded in each layer (W/m^2)
%       Tbottom = specified boundary condition for the bottom node
%
%*****************************************************************************

% Changing the variable names
    rho = layers(:,1);
    Cp  = layers(:,3);
    k   = layers(:,4);

%****Equation Constants
```

```
for i = 2:n_l+1     % i = node index
    a(i)  = k(i-1)/(2*dy^2);
    b1(i) = rho(i-1)*Cp(i-1)/dt + k(i-1)/dy^2;
    b2(i) = rho(i-1)*Cp(i-1)/dt - k(i-1)/dy^2;
    c(i)  = flux(i-1)/dy;
end

% Note: The "i-1" terms are needed to combine the layer and node concepts.  Also
% included the specified temperature B.C. in the solution matrix (adds a row).

%****Setup Crank-Nicolson equations for each node in matrices.  Then will solve
%    the following: [A]*[Temp]=[B] for [Temp], which are the new time step temps.

%****Left Side Matrix
A = zeros(n_l+1);

for i = 2:(n_l)
    A(i,i-1) = -a(i);
    A(i,i) = b1(i);
    A(i,i+1) = -a(i);
end

A(1,1) = 1;                       % Specified Lower Temperature B.C.
A(n_l+1,n_l)   = -2*a(n_l+1);     % Upper Gradient B.C.
A(n_l+1,n_l+1) = b1(n_l+1);       % Upper Gradient B.C.

%****Right Side Matrix
B = zeros(n_l+1,1);

for i = 2:(n_l)
    B(i,1) = a(i)*Temp(i-1,1) + b2(i)*Temp(i,1) + a(i)*Temp(i+1,1) + c(i);
end

B(1,1) = Tbottom;                 % Specified temperature of B.C. plate
B(n_l+1,1) = 2*a(n_l+1)*Temp(n_l,1) + b2(n_l+1)*Temp(n_l+1,1) +
3*c(n_l+1);
                                  % RHS of the gradient boundary condition

Temp = A\B;  % returns a column array of updated temperatures
             % Temp(:,1) = [T(bottom); T(2); ...; T(n_t); T(n_l+1)]

function [Tadj] = temp_control(Temp, n_l)

%   This function controls snow temperatures.
%   If an snow layer gets warmer than zero the
%   temp control function will fix it to a zero.

%********** INPUTS ***************************************************************
%   Temp = the calculated temperature profile that needs to be adjusted
%   n_l = number of snow layers
%
%********** OUTPUTS **************************************************************
%   Tadj = is the new adjusted temperature profile (C)
%*************************************************************************************

for i = 1:n_l+1
   if Temp(i,1) >= 0, Temp(i,1) = 0; end
end

Tadj = Temp;
```

APPENDIX B

CAR C++ CODE

```
/************************************************************
main.c
**** SNOW ALBEDO PROGRAM: This program scans input data from a file
(albedodata.txt), calls the albedo function (Albedo.c), which calculates
snow albedo, and creates an output file (albedoresults.txt).
************************************************************/

#include <stdio.h> #include <stdlib.h>

// PROTOTYPE FUNCTION //
int Albedo(int iwvl,int lab,double cosz,double ps, double rad,
       double snowmass,long double soot,double srfalb[2],
       double dfrac[2],double sflx[2],double trans[3],
       double alb[3],double albm[3],double cmxs[2],
       double dens,double kap[2]);

// PROCEDURE //
void main(void) {
// DECLARE VARIABLES //
double cosz,ps,rad,snowmass,cmxs[2],dens,kap[2]; long double soot; double
srfalb[2],dfrac[2],sflx[2],trans[3],alb[3],albm[3]; int iwvl,lab; int n_l
= 1; FILE *file, *file_out;

// OPEN THE FILE FOR INPUT //
if((file = fopen("albedodata.txt","r"))==NULL)
    {
    printf("Cannot open the file albedodata.txt.\n");
    exit(1);
    }

// OPEN THE FILE FOR OUTPUT //
if((file_out = fopen("albedoresults.txt","a+"))==NULL)
    {
    printf("Cannot open the file albedoresults.txt. \n");
    exit(1);
    }

//*****************************************************************
//  SNOW ALBEDO CALCULATION
//*****************************************************************

// PRINT DESCRIPTIVE COLUMN LABELS
printf("   ALBEDO RESULTS:\n"); printf("#
rad/mass/dens/VIS/NIR/SOLAR/cmxs(VIS)/cmxs(NIR)/kap(VIS)/kap(NIR)\n");


// LOOP OVER THE INPUT FILE //
while(!feof(file))      //loops through each input line until eof
    {
    // READ THE VALUES IN FROM THE FILE //
    fscanf(file,"%lf%lf%lf%lf%i%i%lf%lf%lf%lf%lf%lf%lf%lf%lf\n",
    &rad,&soot,&snowmass,&dens,&iwvl,&lab,&cosz,&ps,&srfalb[0],
    &srfalb[1],&dfrac[0], &dfrac[1],&sflx[0],
    &sflx[1],&trans[0],&trans[1],&trans[2]);

    if (n_l != 1)   // Comment out this block for independent CAR runs (no layering)
        // Assign computed alb as new underlying alb (srfalb)
        // Not applicable for the first iteration (n_l !=1)
    {
        srfalb[0] = alb[0];
        srfalb[1] = alb[1];
        printf("%f %f\n",srfalb[0],srfalb[1]);
    }
    //  printf("%f %f\n",srfalb[0],srfalb[1]); /* test */

    // RUN ALBEDO ROUTINE //
```

```
    if(Albedo(iwvl,lab,cosz,ps,rad,snowmass,soot,srfalb,
    dfrac,sflx,trans,alb,albm,cmxs,dens,kap)!=0)
        {
        printf("Trouble calculating albedo!\n");
        exit(1);
        }

    // PRINT THE VALUES TO THE FILE //
    fprintf(file_out,"%i %f %f %f %f %f %f %f %f %f %f\n",n_l,rad,
            snowmass,dens,alb[0],alb[1],alb[2],cmxs[0],cmxs[1],kap[0],kap[1]);

    // PRINT TO SCREEN
    printf("%i %f %f %f %f %f %f %f %f %f %f\n",n_l,rad,snowmass,dens,
        alb[0],alb[1],alb[2],cmxs[0],cmxs[1],kap[0],kap[1]);

    n_l++;  //Increment layer counter
    }

// CLOSE THE FILES //
fclose(file); fclose(file_out); }


/*****************************************************************
 END of main.c
*****************************************************************/

/*****************************************************************
                        ALBEDO ROUTINE

This program calculates the albedo of snow. It defines it in terms of
impurities, grain size, snow mass, and the albedo of the underlying
surface. Factors that are also included are atmospheric mass (which is
determined by altitude and angle of incident light) and percentage of
diffuse light. This work is basically the result of earlier work by Susan
Marshall. Her Ph.D. thesis, "A Physical Parameterization of Snow Albedo
for Use in Climate

  Models", University of Colorado, 1989, utilizes the work of Steve
Warren, University of Washington. She developed a model that simplifies
Warren's work so that it can be used in large computational models for
climate analysis. She wrote a Fortran program, and from it this C program
was developed.

************************** DEFINE VARIABLES ***********************
*****INPUTS:

iwvl            defines wavelength separation of visible
                and NIR
                = 0 split at 0.7 micrometers
                = 1 split at 0.9 micrometers

lab             flag used to differentiate between laboratory
                and outside conditions
                = 0 outside conditions
                = 1 inside/laboratory conditions

cosz            solar zenith angle cosine

ps              surface air pressure (millibars)

rad             snow grain radius (micrometers)

snowmass        optical snow depth [density*layer depth] (kg/m^2)

dens            snow density (used to calculate extinction
                coefficients with 1% method)
```

```
soot            soot content of snow (mass fraction) (normalize
                impurities other than soot in input file before
                running CAR)

surfalb(i)      albedo of underlying surface
                i = 0   visible
                i = 1   NIR

dfrac(i)        diffuse fraction of surface downflux
                i = 0 visible
                i = 1   NIR

sflx(i)         fraction of surface downflux in each spectral ban
                (needed only to return value of broadband
                solar snow albedo)
                i = 0   visible
                i = 1   NIR

trans(i)        atmospheric transmittance (fraction)
                If value < 0, solar transmittance defaults to
                value of 0.55 and the others will be estimated
                in the program.
                i = 0   visible
                i = 1   NIR
                i = 2   solar (default = 0.55)

*****OUTPUTS: alb(i)          snow albedo
                i = 0   visible
                i = 1   NIR
                i = 2   solar

albm(i)         max snow albedo
                i = 0   visible
                i = 1   NIR
                i = 2   solar

cmxs(i)         critical mass cross section (kg/m^2) for determining
                semi-infinite depth as well as the extinction coeff.
                i = 0   visible
                i = 1   NIR

kap(i)          extinction coefficient calculated from dens and cmxs(i)
                using 1% as extinction rule
                i = 0   visible
                i = 1   NIR

n_l             layer counter: counts number of input lines from
                albedodata.txt


*****LABORATORY SETTING:
    -> when this albedo model is applied in a lab setting only
    the following functions are needed from CAR:
        - efrad
        - albclr
        - efsoot
        - alb5
        - cmassxs
        - aintrp (only when underlying sfc albedo is high)
    -> Functions NOT called:
        - albcld        - dfrac         - transmt

************************* REFERENCES ******************************

Marshall, S. 1989. A new snow albedo parameteriztion for use in climate
```

models. Ph. D. thesis. University of Colorado

Marshall, S.E. and S.G. Warren 1987. Parameterization of Snow Albedo for Climate Models in Large Scale Effects of Seasonal Snow Cover (Proceedings of the IUGG/IAHS Symposium. August, 1987). IAHS Publ. no. 166 pp43-50

Wiscombe, W.J. and S.G. Warren 1980. A model for the spectral albedo of snow. I.Pure snow. J. Atmos. Sci. 37. 2712-2733

Rozenberg, G.V. 1966. Twilight: A Study in Atmospheric Optics. Plenum Press. (translated from the Russian). 358pp.

Wallace, J.M. and P.V. Hobbs 1977. Atmospheric Science: An Introductory Survey. Academic Press.

```
*****************************************************************/

#include <math.h> #include <stdlib.h> #include <stdio.h>

// PROTOTYPE FUNCTIONS //
double alb5(int i,double as,double it); double transmt(double solat, int
i,int j); double albclr(int i,int j,double rad,long double soot); double
cmassxs(int i,int j,double rad,long double soot); double aintrp(int i,int
j,double amax,double rad, long double soot,
              double snowd,double srfalb);
double efsoot(int i,int j, long double soot, double snowd,
              double srflab);
double efrad(int i, int j, double rad, double czen); double albcld(int
i,double aclr,double at,long double soot); double difrac(int j,int
i,double sigma,double ram,
              double atrns,double czen);

// PROCEDURE //
int Albedo( int iwvl,int lab,double cosz,double ps,double rad,
            double snowmass,long double soot,double srfalb[2],
            double dfrac[2],double sflx[2],double trans[3],
            double alb[3],double albm[3],double cmxs[2],
            double dens,double kap[2] )

{ /************************** DECLARATIONS ************************/


// DEFINE FLOATING POINT VARIABLES //
double  relairmass,sigma,solat,difmu,dfrc,
        mu,erad,ua,esoot,clear,alb3,albmax;
double po = 1013.0;     // Reference sea-level pressure (mbar) double
solcon = 1372.0; // solar constant (W/m^2)

// DEFINE INTEGER VARIABLES //
int i;

// DEFINE ARRAYS //
double fluxes[2][2] = {{0.46,0.54},{0.63,0.37}};


/*********************** START CALCULATIONS **********************/

// Relative air mass (relairmass) - ref (Rozenberg, 1966)
    // Relative air mass is also called the "optical path length" or
    // the "optical path". Used in difrac function
    // **Not needed for lab**

    relairmass = 1.0/(cosz + 0.025*exp(-11.0*cosz));

    // 1/cosz is sometimes used for the relative air mass.
```

```
    // Max allowable value = 10.0.
    if(relairmass >= 10.0) relairmass = 10.0;

// Solar atmospheric transmittance (SOLAT)(Wallace and Hobbs, 1977)

    // Default, trans[2] = 0.55     **Not needed for lab**
    if (trans[2] <= 0.0) trans[2] = 0.55;
    solat = trans[2];

// Surface to sea level pressure ratio  **Not needed for lab**
    // sigma is the ratio of surface air pressure to the
    // pressure at sea level.
    sigma = ps/po;
    if(sigma >= 1.0) sigma = 1.0;  // Must be above sea level.


// Loop for visible (i = 0) & NIR (i = 1) spectra
    // If value of trans, sflx, or dfrac are set <= 0, they will be
    // estimated via the functions transmt and difrac or defaulted
    // to fluxes.
    // sflx is used to calculate a value for the solar snow albedo.
    // difrac is used to obtain a value of effective zenith cosine.

    for(i=0;i<=1;i++) {         // (NOTE: i=0=VIS; i=1=NIR)

        // Estimate transmittance for visible (i=0) and NIR (i=1).
        // If it is not initally known and supplied as input, use
        // the function trnsmt(solat,i,iwvl). **For laboratory
        // lighting use transmittance equal to one (use input file)
        // **Not needed for lab**.

        if(trans[i] <= 0.0) trans[i] = transmt(solat,i,iwvl);

        // Estimate surface downflux for visible (i=0) and
        // NIR (i=1). If it is not initally known and supplied as
        // input, use the matrix fluxes[i][j].

        if(sflx[i] <= 0.0) sflx[i] = fluxes[iwvl][i];

        // Estimate diffuse fraction. This is the fraction of the
        // incoming radiation at the snow surface that is diffuse
        // rather than direct from solar radiation. **For lab
        // lighting assume diffuse fraction = 0

        if ((dfrac[i] <= 0.0) && lab==0)    // not known, estimate
            dfrc = difrac(iwvl,i,sigma,relairmass,trans[i],cosz);
        else
            dfrc = dfrac[i];

        // The zenith cosine is weighted for diffuse and direct
        // fraction, mu. The effective zenith cosine for diffuse
        // radiation is cosz = 0.65.  **For lab get back mu = dfrac

        difmu = 0.65;
        mu = dfrc*difmu + (1.0-dfrc)*cosz;

        if(mu >= 1.0) mu = 1.0; // mu must lie between 0.0 and 1.0
        if(mu <= 0.0) mu = 0.0;

        // Estimate effective snow grain radius.
        erad = efrad(iwvl,i,rad,mu);

        // Estimate deep snowcover albedo (albmax).
        ua = srfalb[i];   // user defined underlying surface albedo
        albmax = albclr(iwvl,i,erad,soot);  //semi-infinite albedo
```

```
    // **Semi-infinite albedo only needs two
    //   parameters: erad and soot. Doesn't
    //   include mxs or underlying albedo.**

albm[i] = albmax;       // assign to albm[i]
// printf("\n albmax = %f\n", albmax);  /* test */

// Compute critical mass cross-section (semi-infinite depths)
cmxs[i] = cmassxs(iwvl,i,erad,soot);

// Compute extinction coefficients based on cmxs[i] and dens
kap[i] = -log(0.01)/(cmxs[i]/dens);

// Check for special case where srfalb > albmax.
    if(albmax <= ua)
        {
        //printf("surface albedo > albmax\n");  /* test */

        // surface albedo is greater than snow albmax
        alb[i] = aintrp(iwvl,i,albmax,erad,soot,snowmass,ua);
        }
            // **Not usually physically the case (might use
            //   in lab)**
    else
        {
        //printf("surface albedo < albmax\n");  /* test */

        // snow albmax is greater than surface albedo.
        esoot = efsoot(iwvl,i,soot,snowmass,ua);

        // Calculate albedo for effective soot and effective
        // radius.
            // **If snow is semi-infinite, then this below
            //   calculation will remain equaling albmax**
        alb[i] = albclr(iwvl,i,erad,esoot);
        }

    // Correct for NIR snow albedo for:
    //  (a) cloudy sky
    //  (b) extend albedo to full range => 5 micrometers.
    //  **Note: The following "if" statements adjust outside
    //          (lab=0) NIR (i=1) albedo for the above corrections.
    if((i==1) && (lab==0))
        {
        // cloudy day
        clear = alb[i];
        //printf("clear = %f\n", clear); /* test */

        alb[i] = albcld(iwvl,clear,trans[i],esoot);
        //printf("alb[1] = %f\n", alb[i]); /* test */

        // extend to 5 micrometers
        alb3 = alb[i];
        alb[i] = alb5(iwvl,alb3,trans[i]);
        }
    else if(i==1)   // correct lab albedo to full range
        {
        // extend to 5 micrometers
        alb3 = alb[i];
        alb[i] = alb5(iwvl,alb3,trans[i]);
        //printf("inside = %f\n", alb[1]); /* test */
        }

// PRINT TO SCREEN  /* test */
//printf("%i %f %f %f\n\n",i,erad,alb[i],trans[i]);
}
```

```
    // Calculate snow solar albedo
    alb[2] = (sflx[0]*alb[0] + sflx[1]*alb[1]);

    // Calculate maximum snow solar albedo (albm)
    albm[2] = (sflx[0]*albm[0] + sflx[1]*albm[1]);

    return 0;
    }   // End albedo program

/********************** CALLED FUNCTIONS: ************************/

/*****************************************************************/

double transmt(double solat,int i,int j)

/*****************************************************************/

// This function estimates the visible or NIR atmospheric
// transmittance given a value of of the solar atmospheric
// transmittance.
// **Not called for lab application**

// INPUT VARIABLES
//  solat = solar atmospheric transmittance
//  i = 0 for visible, =1 for NIR.
//  j = iwvl = separation factor between visible and NIR.

    {

    double transmttnce;

    double  a[2][2] = {{1.5710,0.4246},
                               {1.5064,0.0579}};
    double  b[2][2] = {{-0.5715,0.5751},
                               {-0.5060,0.9412}};

    // a[i][j] and b[i][j] are both empirical matrices for calculating
    // transmittance of the atmosphere if it is not initially known.

    transmttnce = a[j][i]*solat + b[j][i]*solat*solat;
    return transmttnce;
    }

/*****************************************************************/

double difrac(int j,int i,double sigma,double ram,double atrns,
              double czen)

/*****************************************************************/

// This function estimates the fraction of diffuse radiation,
// given values sigma. Correction factors for relative airmass,
// atmospheric transmittance and zenith cosine are inlcuded.
// **Not called for lab application**

// INPUT VARIABLES
//  j = iwvl, wavelength separation parameter.
//  i = visible/NIR identification parameter.
//  sigma = The ratio of surface air pressure to the pressure
//          at sea level.
//  ram = Relative air mass is also called the "optical path
//        length" or the "optical path".
//  atrns = atmospheric transmittance, "trans[i]"
//  czen = Zenith cosine
```

```
    {
    double dclr, slope, tclr,diffrac;       /** 0.0486 **/
    double at[2][2] = {{0.0540,-0.2567},{0.0400,-0.3957}};
    double bt[2][2] = {{-0.4000,0.3061},{-0.8000,0.2383}};
    double c[2][2] = {{0.4460,0.0630},{0.3450,0.2500}};
    double k[2][2] = {{-0.3888,-0.1686},{-0.4135,-0.0042}};
    double asl[2][2] = {{-0.3389,-0.2971},{-0.3417,-0.2479}};
    double bsl[2][2] = {{0.4689,0.2943},{0.4588,0.1895}};

    // tclr is the clear sky transmission. Calculate this.
    if(i==0)        // visible spectrum
        tclr = 1.0 - (at[j][i]*ram)*exp(bt[j][i]*(1.0-sigma));
    else            // NIR spectrum
        tclr = exp((at[j][i]*pow(ram,bt[j][i]))*sigma);

    // tclr must lie between atrans and 1.0.
    if(tclr >=1.0) tclr = 1.0;
    if(tclr <= atrns) tclr = atrns;

    // Calculate clear sky diffuse fraction dclr.
    dclr = c[j][i]*(1.0 - exp(k[j][i]*ram*sigma));
    // dclr must lie between 0.0 and 1.0.
    if(dclr >= 1.0) dclr = 1.0;
    if(dclr <= 0.0) dclr = 0.0;

    // Zenith cosine (czen).
    slope = asl[j][i] + bsl[j][i]*czen;

    // Calculate diffuse fraction (difrac).
    diffrac = (atrns - tclr)*slope + dclr;
    // difrac must lie between dclr and 1.0.
    if(diffrac >= 1.0)  diffrac = 1.0;
    if(diffrac <= dclr) diffrac = dclr;

    return diffrac;
    }

/*****************************************************************/

double efrad(int i,int j,double rad,double czen)

/*****************************************************************/

// This function estimates the effective radius, "efrad" of the snow
// given a value of the actual mean grain radius, "rad" and the
// zenith cosine angle, "czen". This procedure simplifies the
// problem by combining the effects of radius and zenith
// cosine. Both effects are similar therefore they are combined.

// INPUT VARIABLES
//  i = iwvl, wavelength separation parameter
//  j = visible/NIR identification parameter
//  rad = mean grain radius
//  czen = zenith cosine

    {
    double slope, delmu, sqrad, ratio,efradius;
    double  b[2][2] =   {{1.2812,1.2642}, {1.3072,1.2039}};

    slope = b[i][j];
    delmu = czen - 0.65;
    sqrad = sqrt(rad);
    ratio = sqrad/slope;
    efradius = pow((sqrad + delmu*ratio), 2);

    return efradius;
```

```
    }

/*****************************************************************/

double albclr(int i,int j,double rad,long double soot)

/*****************************************************************/

// This function calculates clear sky surface albedo.

// INPUT VARIABLES
//  i = iwvl, wavelength separation parameter
//  j = visible/NIR identification parameter
//  rad = effective grain radius
//  soot = effective soot content

    {
    double  al,ah,a2,s2,s2l,ratio,k,sqrl,sqrad,albedoclr;
    double  l[2][2] = {{0.0700,0.0590}, {0.0710,0.0490}};
    double  c[2][2] = {{0.9988,1.0667}, {0.9952,0.9832}};
    double  d[2][2] = {{-0.0020,-0.1811}, {-0.0034,-0.2161}};
    double  a[2][2] = {{-6.3550,-5.9328}, {-6.3914,-6.0302}};
    double  b[2][2] = {{-1.9752,-1.8102}, {-1.9194,-1.5541}};
    double  kl[2][2] = {{0.4540,0.5670}, {0.4690,0.6320}};
    double  kh1[2][2] = {{0.4500,0.5800}, {0.4500,0.8000}};
    double  kh2[2][2] = {{-0.0400,-0.0400}, {-0.0400,-0.1200}};

    sqrad = sqrt(rad);
    sqrl = log(sqrad);
    al = l[i][j];

    // Visible spectrum for ah (j = 0).

    if(j == 0)
    ah = c[i][j] + d[i][j]*sqrad;

    // NIR spectrum for ah (j = 1).

    if(j == 1) ah = c[i][j] + d[i][j]*sqrl;

    s2l = a[i][j] + b[i][j]*sqrl;
    s2 = exp(s2l);
    a2 = (al + ah)/2.0;
    if(soot >= s2)
        {
        k = kl[i][j];
        ratio = log(soot) - s2l;
        albedoclr = al + (a2 - al)*exp(-k*ratio);
        if (albedoclr <= al) albedoclr = al;
        }
    else
        {
        if(soot <= 1.0e-9) soot = 1.0e-9;
        ratio = s2l-log(soot);
        albedoclr = ah - (ah - a2)*exp(-kh1[i][j]*ratio
                    + kh2[i][j]*ratio*ratio);
        if(albedoclr >= ah) albedoclr = ah;
        }
    return albedoclr;
    }

/*****************************************************************/

double cmassxs(int i,int j,double rad,long double soot)

/*****************************************************************/
```

```
// This function uses the same equations as aintrp, but only
// returns a value for the maximum critical depth (semi-infinite).

// INPUT VARIABLES
//  i = iwvl, wavelength separation parameter
//  j = visible/NIR identification parameter
//  rad = effective grain radius
//  soot = soot concentration (mass fraction)

    {
    long double  ar,rtox,brs,negp,t[2],crtmass;
    double  a[2][2][2] = {{{0.1983, 2.640},{5.0e-5, 3.2e-5}},
                          {{1.5e-2, 1.300},{4.0e-5, 5.0e-4}}};
    double  b[2][2][2] = {{{2.67e9,8.67e8},{0.0,0.0}},
                          {{2.60e7,2.00e8},{0.0,0.0}}};
    double  x[2][2][2] = {{{1.50,1.40},{0.640,-1.00}},
                          {{1.20,1.40},{0.640,0.0}}};
    double p = 0.50;
    int k;
    negp = -p;

    for(k = 0;k<=1;k++)
        {
        ar = a[i][j][k]*rad; //printf("a=%f ",a[i][j][k]);
        brs = b[i][j][k]*rad*soot; //printf("brs=%f ",b[i][j][k]);
        rtox = pow(rad,x[i][j][k]); //printf("x=%f \n",x[i][j][k]);
        t[k] = ar*pow((brs + rtox),negp);
        }
    crtmass = t[1]; //maximum critical mass cross-section

    return crtmass;
    }

/*****************************************************************************/

double aintrp(int i,int j,double amax,double rad,
              long double soot,double snwmass,double srfalb)

/*****************************************************************************/

// This function interpolates the snow albedo as a function of soot
// content when the underlying surface albedo is higher than the snow
// surface albedo. Also included is the case where dirty snow overlies
// clean snow.

// INPUT VARIABLES
//  i = iwvl, wavelength separation parameter
//  j = visible/NIR identification parameter
//  amax = deep snow cover albedo
//  rad = effective grain radius
//  soot = soot concentration (mass fraction)
//  snwmass = snowmass per unit area
//  srfalb = road surface albedo

    {
    long double  ar,rtox,brs,negp,tmin,tmax, slope,diff,tmin10,
            tmax10,aintrpp,t[2];
    double  a[2][2][2] = {{{0.1983, 2.640},{5.0e-5, 3.2e-5}},
                          {{1.5e-2, 1.300},{4.0e-5, 5.0e-4}}};
    double  b[2][2][2] = {{{2.67e9,8.67e8},{0.0,0.0}},
                          {{2.60e7,2.00e8},{0.0,0.0}}};
    double  x[2][2][2] = {{{1.50,1.40},{0.640,-1.00}},
                          {{1.20,1.40},{0.640,0.0}}};
    double p = 0.50;
```

```
    int k;
    negp = -p;

    for(k = 0;k<=1;k++)
        {
        ar = a[i][j][k]*rad; //printf("a=%f ",a[i][j][k]);
        brs = b[i][j][k]*rad*soot; //printf("brs=%f ",b[i][j][k]);
        rtox = pow(rad,x[i][j][k]); //printf("x=%f \n",x[i][j][k]);

        //printf("ar=%f; brs=%f; rtox=%f\n",ar,brs,rtox); /* test */
        t[k] = ar*pow((brs + rtox),negp);
        }
    tmin = t[0];
    tmax = t[1];
    printf("");  // needed to make model run for thin snow layers
    //printf("tmin = %f; tmax = %f; VIS(0)/NIR(1) = %i\n",tmin,tmax,j);  /* test */ //

    if(snwmass <= tmin)
        {
        //printf("snwmass <= tmin\n");  /* test */
        aintrpp = srfalb;
        }
    else if(snwmass >= tmax)
        {
        //printf("snwmass >= tmax\n");  /* test */
        aintrpp = amax;
        }
    else
        {
        // Now interpolate
        //printf("snwmass <= tmax\n");  /* test */
        tmin10 = log10(tmin);
        tmax10 = log10(tmax);
        //printf("tmin10=%f; tmax10=%f \n",tmin10, tmax10);  /* test */
        //printf("amax=%f; srfalb=%f \n", amax, srfalb);
        slope = (amax - srfalb)/(tmax10 - tmin10);
        diff = log10(snwmass) - tmin10; //log10(tmin);
        //printf("slope=%f; diff=%f \n",slope, diff);  /* test */

        aintrpp = slope*diff + srfalb;
        }

    //printf("aintrpp=%f\n", aintrpp);  /* test */
    return aintrpp;
    }

/*************************************************************/

double efsoot(int i,int j, long double soot, double snwmass,
              double srfalb)

/*************************************************************/

// This function estimates the effective soot given values of
// soot concentration "soot", snowmass "snwmass", and underlying
// surface albedo "srfalb".

// INPUT VARIABLES
//  i = iwvl, wavelength separation parameter
//  j = visible/NIR identification parameter
//  soot = soot concentration (mass fraction)
//  snwmass = snow mass per unit area
//  srfalb = underlying surface albedo

    {
    double a,b,seffo, effecsoot;
```

```
    double  ao[2][2] = {{-13.6421,-13.7878}, {-13.7781,-13.6237}};
    double  a1[2][2] = {{-2.3306,-2.7360}, {-1.8936,-1.8347}};
    double  bo[2][2] = {{-1.2430,-1.3433}, {-1.2855,-1.3044}};
    double  b1[2][2] = {{0.5714,0.9005}, {0.6730,1.3470}};
    double  b2[2][2] = {{-0.4319,-1.5425}, {-0.5038,-2.1925}};

    // Calculate the effective soot as a function of soot content
    // and snow depth.

    a = ao[i][j] + a1[i][j]*srfalb;
    b = bo[i][j] + (b1[i][j]*srfalb) + (b2[i][j]*srfalb*srfalb);
    seffo = exp(a)*pow(snwmass,b);
    if(seffo >= 1.0) seffo = 1.0;
    effecsoot = soot + seffo;
    if(effecsoot <= 1.0e-9) effecsoot = 0.0;

    return effecsoot;
    }

/*****************************************************************/

double albcld(int i,double aclr,double at,long double soot)

/*****************************************************************/

// This function estimates the change in NIR snow albedo
// under overcast skies. This usually results with an increase in
// albedo due to shifts in the specturm of the incoming radiation.
// - ref (Marshall and Warren, 1987)
// **Not called for lab application**

// INPUT VARIABLES
//  at = atmospheric transmittance.
//  soot = effective soot content.
//  aclr = albedo under clear skies.

    {
    double a[2] = {0.3865,0.1952};
    double b[2] = {0.0640,0.0384};
    double c[2] = {0.0017,0.0011};
    double to[2] = {0.740,0.640};

    double sl,beta,albedocld;

    if(soot <= 1.0e-9) soot = 1.0e-9;
    sl = log(soot);
    beta = a[i] + b[i]*sl + c[i]*(sl*sl);
    albedocld = (at-to[i])*beta + aclr;

    // The albedo on a cloudy day must lie between 1.0
    // and the value on a clear day.

    if(albedocld >= 1.0) albedocld = 1.0;
    if(albedocld <= aclr) albedocld = aclr;

    return albedocld;
    }

/*****************************************************************/

double alb5(int i,double as,double at)

/*****************************************************************/

// This function corrects albedo to full solar range (>= 5 micrometers).
```

```
// INPUT VARIABLES
//  i = wavelength separation parameter
//  as = albedo (either visible or NIR)
//  at = atmopspheric transmittance (either visible or NIR)

    {
    double frac5, albedo5;

    double  a[2] = {0.0016,-0.0020};
    double  b[2] = {-0.0158,0.0141};
    double  c[2] = {0.0462,0.0372};

    double  albo = 0.015;

    frac5 = a[i] + b[i]*at + c[i]*at*at;
    if((i == 0) && (frac5 <= 0.17)) frac5 = 0.0;
    if(frac5 <= 0.0) frac5 = 0.0;
    albedo5 = (1.0 - frac5)*as + frac5*albo;
    return albedo5;
    }

/*****************************************************************
END of Albedo.c
*****************************************************************/
```